

Nitrogen-doped carbonaceous materials for energy and catalysis

Dissertation

zur Erlangung des akademischen Grades
Doktor der Naturwissenschaften (“Doctor rerum naturalium”, Dr. rer. nat.)
in der Wissenschaftsdisziplin “Materialwissenschaft”

eingereicht an der Mathematisch-Naturwissenschaftlichen Fakultät
der Universität Potsdam
von

Enrico Lepre

Geboren am 02.12.1995 in Monfalcone

Potsdam 2022

Unless otherwise indicated, this work is licensed under a Creative Commons License Attribution 4.0 International.

This does not apply to quoted content and works based on other permissions.

To view a copy of this licence visit:

<https://creativecommons.org/licenses/by/4.0>

Hauptbetreuer: Prof. Dr. Dr. h.c. Markus Antonietti

Zweitbetreuer: Prof. Dr. Adreas Taubert

Metorin: Dr. Maria de las Nieves López Salas

Gutachter/innen Prof. Dr. Dr. h.c. Markus Antonietti

Prof. Dr. Adreas Taubert

Dr. Ana Primo

Published online on the

Publication Server of the University of Potsdam:

<https://doi.org/10.25932/publishup-57739>

<https://nbn-resolving.org/urn:nbn:de:kobv:517-opus4-577390>

If you don't make mistakes, you're not working on hard enough problems, and that's a mistake.

Frank Wilczek

Acknowledgment

Despite the Ph.D. being a personal journey, I found help and support in many people, without whom this thesis would not have been possible and need to be mentioned. First, I want to express my gratitude to my supervisor, Prof. Dr. Dr. h.c. Markus Antonietti, who accepted me into his department and has been a central source of inspiration throughout these years. I want to acknowledge Prof. Andreas Taubert for being my second supervisor and letting me teach in his course at the University of Potsdam.

Among all the people, Prof. Nieves López Salas has been the most central and crucial for this work. She has been my mentor, group leader, and friend, and her humanity will always remain a moral compass for me. I want to thank her for all the teaching, scientific discussions, and personal support which helped me grow as an aspiring scientist and, more importantly, as a person. Thank you, Nieves.

I want to thank Josep Albero, Ivan K. Ilic, Julian Heske, Michal Nowakowski, Ernesto Scoppola, Ivo Zizak, Tobias Heil, Thomas D Kühne, Cristian Cavedon, and Bartholomäus Pieber for participating to part of the experimental results which will be described in this work. Moreover, I would like to acknowledge Jessica Brandt, Antje Voelkel, Bolortuya Badamdorj, and Heike Runge for helping me with part of the material characterization.

Personal support was as much crucial as work support. For this reason, I want to thank Stefano Mazzanti and Janina Kossmann for being the first friends I found here in Germany. They made life as an expat much more pleasant and, despite my stubbornness, taught me different ways of seeing life. Together with them, I want to thank the Colloid Chemistry Department, which allowed building a vivid and never-boring social network. Among them, I want to thank the OCHEAMA group, which I saw growing with exciting new science every year, and Erich C and BEEM, which taught me that science and music are excellent partners.

Despite being in Germany, I also had a lot of support from my native country. In particular, I want to thank Francesco and David for always being there when I needed them. I want to thank the department of Chemistry of the University of Trieste and, in particular, Prof. Paolo Fornasiero for giving me the chance to move to Germany to pursue my ambitions. Finally, I want to thank my family, Mauro, Paola, and Diana, who helped me stand for my values every day.

Outline

The increasing consciousness of humankind for the surrounding environment is the core of society development. This process improved human life conditions but also increased the anthropogenic impact on the surrounding world. Aiming to decrease such impact while preserving the progress made, the role of materials science is to provide new and more accurate descriptions of materials and their properties. Within this frame, this thesis will focus on the synthesis, characterization, and application of carbonaceous materials in electrical energy storage and heterogeneous catalysis (**Chapter 1**).

Carbon-based materials are extensively used for their relatively low cost and wide mechanical, thermal, electrical, and chemical properties. This thesis will describe the synthesis of different carbon materials obtained from nucleobases utilizing the salt melt templating method. By using different precursors, salt mixtures, and synthetic temperatures, it aims to provide further insights into the relationship between synthetic conditions and final material properties (**Chapter 2**).

Electrical energy storage is a crucial technology to increase society's sustainability. Carbon-based materials are widely used in energy storage devices due to their low cost, good conductivity, and high specific surface area. Even though the preparation of such devices plays a fundamental role in the final performance, its effect on the materials is often overlooked. Here, a focus on ball milling for electrode preparation from carbonaceous materials will be reported, aiming to test the oxidation resistance of the materials and their performance as Li-ion capacitors cathodes (**Chapter 3**).

Heterogeneous catalysis is a fundamental tool in the production of chemicals. Nowadays, it is characterized by the wide use of heavy and noble metals, which are expensive, and their production impacts the environment. To reduce their usage, carbocatalysis and single-atom catalysis are promising strategies that attracted attention over the last decade. This thesis will focus on identifying the structure-performance relationship of nitrogen-doped carbon materials in thermal catalysis (**Chapter 4**). Moreover, it will investigate nickel single-atom materials' synthesis, characterization, and catalytic properties in electrocatalysis (**Chapter 5**).

Nitrogen-doped carbonaceous materials for energy and catalysis

Contents

1	Introduction to carbonaceous materials and their applications	25
1.1	The role of materials science	27
1.2	Carbon-based materials	28
1.2.1	General introduction to carbon-based materials	28
1.2.2	Control of the porous structure	31
1.2.3	Control of the composition	33
1.3	Electrochemical energy storage	35
1.3.1	Devices for electrochemical energy storage	35
1.3.2	Carbon materials for electrochemical energy storage	36
1.4	Heterogeneous catalysis	37
1.4.1	Carbocatalysis	39
1.4.2	Single-atom catalysis	41
2	Salt melt templated synthesis	61
2.1	Synthetic procedure	63
2.2	Precursor dependence	64
2.3	Salt melt dependence	69
2.4	Temperature dependence	74
3	Oxidation resistance for Li-ion capacitor cathodes	81
3.1	The role of electrode preparation	83
3.2	Caffeine derived materials	84
3.3	Ball milled derived cathode materials	88
3.4	Performance of a caffeine derived cathode	90
4	Catalytic properties of carbonaceous materials	95
4.1	Nitrogen role in carbocatalysis	97
4.2	Carbonaceous materials for redox catalysis	98
4.3	Carbonaceous materials for acid-base catalysis	101
4.4	Catalytic influence of nitrogen speciation	103

5	Unconventional selectivity of Ni-decorated carbonaceous materials	111
5.1	Nickel for single-atom materials	113
5.2	Nickel decorated materials	114
5.3	Local structure of nickel atoms	120
5.4	Electrocatalytic activity for CO ₂ reduction reaction	123
6	Conclusion	131
7	Appendix	135
7.1	Methods applied	136
7.2	List of used chemicals	144
7.3	Material synthesis	145
7.4	Catalytic experiments	146
7.5	Electrochemical methods	147
7.6	List of publications	151
7.7	Declaration	153

List of Figures

1.1	(On the left) Graphical representation of crystalline, amorphous, and nano carbons structures, and (on the right) number of publication per year from Web of Science in 2022.	29
1.2	Graphical representation of the variables controllable and parameter measurable during the carbonization process.	30
1.3	Schematic visualization of different strategies towards porous carbons.	32
1.4	Schematic visualization of different carbon-based materials with increasing nitrogen content.	34
1.5	Graphical representation of an ideal ion capacitor.	36
1.6	Schematic visualization of different categories of catalysis.	38
1.7	Schematic visualization of different functionalities and their activity in carbocatalysis.	40
1.8	Schematic visualization of bulk to single-atom distribution supported on an ideal surface.	42
2.1	Graphical representation of the salt melt templated synthesis.	63
2.2	(From left to right) Molecular structure of cytosine, adenine and caffeine.	64
2.3	Thermogravimetric analysis at 10 K min ⁻¹ of (from left to right) precursor in nitrogen, materials in nitrogen, materials in synthetic air.	65
2.4	(from left to right) X-ray diffraction patterns, FT-IR transmittance spectra, and elemental composition from SEM-EDX of C8LZ (green), A8LZ (blue) and CF8LZ (red).	66
2.5	Scanning electron microscopy (first row) and Scanning transmission electron microscopy (second row) of (from left to right) C8LZ, A8LZ, and CF8LZ.	67
2.6	Graphical representation of the sol-gel-like mechanism proposed.	68
2.7	(From left to right) N ₂ isotherms at 77K, DFT calculated pore size distribution, and CO ₂ adsorption isotherm at 273K for C8LZ (green), A8LZ (blue), and CF8LZ (red).	69
2.8	Thermogravimetric analysis at 10 K min ⁻¹ of (from left to right) materials in nitrogen and materials in synthetic air.	70

2.9	(from left to right) X-ray diffraction patterns, FT-IR transmittance spectra, and elemental composition from SEM-EDX of C8NZ (red), C8LZ (blue), and C8LK (green).	71
2.10	Scanning electron microscopy (first row) and Scanning transmission electron microscopy (second row) of (from left to right) C8LZ, C8NZ, and C8LK.	72
2.11	(From left to right) N ₂ isotherms at 77K, DFT calculated pore size distribution, and CO ₂ adsorption isotherm at 273K for C8NZ (red), C8LZ (blue), and C8LK (green).	73
2.12	Thermogravimetric analysis at 10 K min ⁻¹ of (from left to right) materials in nitrogen and materials in synthetic air.	74
2.13	(from left to right) X-ray diffraction patterns, FT-IR transmittance spectra, and elemental composition from SEM-EDX.	75
2.14	Scanning electron microscopy (first row) and Scanning transmission electron microscopy (second row) of (from left to right) C5LZ, C6LZ, C7LZ, and C8LZ. . .	76
2.15	(From left to right) N ₂ isotherms at 77K, DFT calculated pore size distribution, and CO ₂ adsorption isotherm at 273K for C5LZ, C6LZ, C7LZ, and C8LZ. . . .	77
3.1	Graphical representation of different methods for ink preparation. From left to right: a. stirring, b. sonication and c. ballmilling.	83
3.2	a. N ₂ isotherm at 77 K, b. DFT pore size distribution from N ₂ isotherm at 77 K, c. CO ₂ adsorption isotherm at 273 K, d. FT-IR spectra, e. X-ray diffraction pattern, and f. thermogravimetric analysis in synthetic air at 10 K min ⁻¹ for CF7NZ, CF8NZ, Kur, and N-Kur.	87
3.3	50 th cycle charging and discharging curve of a. different composite materials and b. CF7NZ derived composites with and without prior ball milling.	89
3.4	Scanning electron microscopy of the cathode material with and without prior ball milling and energy-dispersive X-ray spectroscopy of the cathode material with and without prior ball milling.	89
3.5	a. Integrated cyclic voltammograms at 5 mV s ⁻¹ , b. Cyclic voltammetry at varying scan rates, c. Open circuit voltage of the cell before cyclic voltammetry test, d. calculated surface-controlled contribution to capacity, e. assessment of the model used for surface-controlled contribution evaluation, f. cyclic voltammogram at 1 mV s ⁻¹ as calculated and as measured.	91
3.6	a. Charging-discharging test at varying current densities, b. Charging-discharging profiles at different current densities, c. charging-discharging test at 0.8 A g ⁻¹ for 300 cycles.	92
4.1	Graphical representation of nitrogen functions in a carbon network and electrical dipole moment in a carbon-nitrogen covalent bond.	97

4.2	Reduction of nitrobenzene to aniline in presence of hydrazine and a catalyst and catalytic performances of different catalysts.	98
4.3	Oxidation reaction of TMB in presence of hydrogen peroxide, Visible spectra of TMB and its oxidized product (TMB _{ox}), and kinetic profiles of absorbance at 652 nm for the different catalysts.	99
4.4	Kinetic profiles of C8LZ in presence of different hydrogen peroxide concentrations and linear fitting of the inverse initial speed at given inverse concentration according to Michaelis-Menten analysis.	100
4.5	CO ₂ cycloaddition reaction to epichlorohydrine and catalytic conversions reported against different materials.	101
4.6	acid-catalyzed hydrolysis of (dimethozymethyl)benzene (DMB) to benzaldehyde (BA) followed by a base-mediated Knoevenagel condensation that yields benzomalononitrile (BMN) and relative kinetic of conversions of the reagents for different materials	102
4.7	Graphical representation as columns of the conversions at 1h for acidic (red) and basic (blue) catalysis for the different materials.	103
4.8	C1s (left column) and N1s (right column)XPS regions and relative deconvolution for C5LZ, C6LZ, C7LZ, and C8LZ.	104
4.9	Stacked bar plot representing moles per 100 g of C1s and N1s species calculated from XPS deconvolution and SEM-EDX composition.	105
4.10	Ammonia temperature programmed desorption (TPD) plotted as TCD signal versus bed temperature.	106
5.1	Graphical representation of a nitrogen coordinated nickel single atom involved in the CO ₂ RR.	113
5.2	(left) Graphic representation of the synthesis of Ni-decorated materials and (right) thermogravimetric analysis in air (10 K min ⁻¹) of the support material and the nickel precursor.	114
5.3	(from left to right) X-ray diffraction patterns and elemental composition from SEM-EDX of the pristine support and the Ni-decorated materials.	115
5.4	(From left to right) N ₂ isotherms at 77K, DFT calculated pore size distribution, and CO ₂ adsorption isotherm at 273K of the pristine support and the Ni decorated materials.	116
5.5	C1s (left column), N1s (center column), and Ni2p (right column) XPS spectra of the pristine support and the Ni decorated materials.	118
5.6	Scanning electron microscopy (first row) and Scanning transmission electron microscopy (second row) of the pristine support and the Ni decorated materials.	119
5.7	Bright field (first row) and high angle annular dark field (second row) scanning transmission electron microscopy images of (from left to right) 2Ni@C8NZ, 6Ni@C8NZ, and 10Ni@C8NZ.	119

5.8	(From left to right) Normalized XANES spectra of Ni, NiO, Ni(acac) ₂ , and Ni-decoration materials, linear combination fitting of Ni-decorated materials with Ni, NiO, and Ni(acac) ₂ , Fourier Transformed EXAFS spectra of Ni decorated materials and Ni(acac) ₂ (no phase correction applied).	120
5.9	Snapshot of the modeled lowest energy structures (first row) and electron density isosurfaces of the same area (second row) of samples 6Ni@C8NZ (left column) and 10Ni@C8NZ (right column). Color code: carbon (black), nitrogen (blue), oxygen (red), nickel (orange).	122
5.10	LSVs using NaOH 1M saturated with different gasses.	123
5.11	a. LSVs in CO ₂ -saturated NaOH 1M obtained using different electrode materials, b. FEs vs. applied potential of 10Ni@C8NZ in CO ₂ -saturated NaOH 1M, c. FEs of 6Ni@C8NZ, 10Ni@C8NZ, and 14Ni@C8NZ at -1.2 V vs RHE in CO ₂ -saturated NaOH 1M, d. Tafel slope calculated using 10Ni@C8NZ as cathode, e. chronoamperometry in CO ₂ -saturated NaOH 1M at -1.2 V vs RHE, f. formic acid concentration evolution using 10Ni@C8NZ as catalyst.	124
7.1	Graphical representation of the Swagelot cell used for the Li-ion capacitor tests.	148
7.2	Graphical representation of the H-cell used during the CO ₂ RR experiments. . .	149

List of Tables

2.1	Summary of the material synthesized, codes and yields.	64
2.2	Composition summary of materials obtained from different precursors.	66
2.3	Gas adsorption data obtained from BET and DFT calculations applied on N ₂ and CO ₂ isotherms at 77K and 273K.	69
2.1	Summary of material synthesized from different salt, melting temperature of these salts, code given to the materials and relative yields.	70
2.2	Composition summary of materials obtained from different precursors.	71
2.3	Gas adsorption data obtained from BET and DFT calculations applied on N ₂ and CO ₂ isotherms at 77K and 273K.	73
2.1	Summary of the material synthesized, codes and yields.	74
2.2	Composition summary of materials obtained at different temperatures.	76
2.3	Gas adsorption data obtained from BET and DFT calculations applied on N ₂ and CO ₂ isotherms at 77K and 273K.	77
3.1	Summary of the material synthesized, codes and yields.	84
3.2	Elemental composition calculated from ECA and ICP-AES for CF7NZ, CF8NZ, Kur, and N-Kur.	85
3.3	specific surface area calculated through BET equation and pore volume from N ₂ isotherm at 77 K and pore volume calculated from CO ₂ isotherm at 273 K for CF7NZ, CF8NZ, Kur, and N-Kur.	86
3.4	Elemental composition calculated from ECA and ICP-AES for CF7NZ, CF8NZ, Kur, and N-Kur after ball milling with stainless steel jar in open atmosphere for 50 min.	86
5.1	Summary of the material synthesized, codes and yields.	114
5.2	Composition summary of the pristine support and the Ni decorated materials.	115
5.3	Gas adsorption data obtained from BET and DFT calculations applied on N ₂ and CO ₂ isotherms at 77K and 273K.	116
5.1	Nickel coordination numbers obtained by radial distribution function integration of simulated 6Ni@C8NZ and 10Ni@C8NZ.	122

5.2	Average net atomic charges calculated using the DDEC6 method from simulated 6Ni@C8NZ and 10Ni@C8NZ.	122
7.1	List of substances used in this thesis with relative CAS registry number, supplier, and purity grade. All the substances were used without further purification. . .	144

Nomenclature

AC Activated carbon

BA Benzaldehyde

BET Brunauer–Emmett–Teller theory

BMN Benzomalononitrile

CO₂RR Carbon dioxide reduction reaction

CV Cyclovoltammetry

DFT Density Functional Theory

DMC (Dimethozymethyl)benzene

ECA Elemental chemical analysis

EDLC Electrostatic double-layer capacitors

EDX Energy-dispersive X-ray spectroscopy

EXAFS Extended X-ray absorption fine structure

FE Faradaic efficiency

FTIR Fourier-transform infrared spectroscopy

HER Hydrigen evolution reaction

HPLC High-performance liquid chromatography

ICP-OES Inductively coupled plasma optical emission spectrometry

IUPAC International Union of Pure and Applied Chemistry

LC Linear combination

LSV Linear sweep voltammetry

MOF	Metal organic framework
Ni(acac) ₂	Nickel acetylacetonate
NRR	Nitrogen reduction reaction
OER	Oxygen evolution reaction
ORR	Oxygen reduction reaction
PSD	Pair distribution function
RHE	Reversible hydrogen electrode
SAC	Single-atom catalyst
SEM	Scanning electron microscopy
STEM	Scanning transmission electron microscopy
tBuOOH	Tert-buthyl peroxide
TGA	Thermogravimetric analysis
TMB	3,3',5,5'-Tetramethylbenzidine
TPD	Temperature programmed desorption
XANES	X-ray absorption near edge structure
XAS	X-ray absorption spectroscopy
XPS	X-ray photoelectron spectroscopy
XRD	X-ray diffraction

Chapter 1

Introduction to carbonaceous materials and their applications

1.1 The role of materials science

From stone to semiconductors, humankind's society evolved proportionally to its knowledge of the surrounding materials. Historians and other scholars have named certain eras after determined class of materials (e.g., *Stone Age*, *Bronze Age*, and *Iron Age*), and the humankind's consciousness seems to be growing in parallel to the increased usage and development of more and more sophisticated materials. Yet, until recently, mastery of materials has been achieved mainly by empirical means or by a form of alchemy. Systematic research was performed only from the nineteenth century, leading to the interdisciplinary field of study named *materials science*.^[1]

This systematic research facilitated the development of more complex devices such as chips and transistors, leading to the computers and the *Silicon age*.^[2] Nevertheless, focusing only on silicon seems to limit the description of the uncountable results that materials science reached over the last 50 years. Polymers are the first example of these achievements and were described as "*the biggest thing that chemistry has done*" by Alexander R. Todd in 1980.^[3] Materials for Li-ion batteries must be the second example as they were recognized by the Nobel Prize in 2019 and hold great potential for the future.^[4] Even though the list can go further, this will go out of the scope of this thesis, and further information might be found in the literature.^[5, 6]

Nevertheless, the advancement of our society thanks to materials science has not come without a price as the adage "*there's no such thing as a free lunch*".^[7] Indeed, better living conditions and a growing population increased our society's energy demand, which is satisfied mainly by the combustion of fossil fuels. The main products of this process are energy, water, and carbon dioxide. While energy is used to sustain our society as mentioned, water and carbon dioxide are emitted into the atmosphere. In particular, carbon dioxide emissions were correlated to the increasing average global temperature measured in recent years, and the phenomenon is known as "*global warming*".^[8, 9]

As result, different scenarios are foresighted depending on how our society will react.^[10] However, it is doubtful that no consequences will be experienced, and our community needs to act to buffer the changes or respond to them. The actions required are multiple, involving single citizens, private companies, and nations. However, finding the balance between a sustainable society in social, economic, and environmental terms is difficult. No decision-making or actions will be fruitful if we base them on wrong perceptions of reality.

In this context, the responsibility of fundamental research is to provide reliable world representations and foster better decision-making. Focusing on materials science, it needs to find more accurate materials descriptions to improve their performances and promote their application in potential sectors for a sustainable economy. In particular, this thesis will describe the properties of carbon-based materials for energy and catalytic applications.

1.2 Carbon-based materials

1.2.1 General introduction to carbon-based materials

Carbon is a nonmetallic chemical element. Its atomic number is 6, and it is the 15th most abundant element in Earth's crust. Its chemical properties are characterized by four electrons in its valence shell, which allow a unique diversity of compounds compared to other elements. This diversity is at the foundation of earth's life, its amplitude pushed chemists to study its properties and reactivity (i.e., organic chemistry), and it expanded to materials science in studying carbon allotropes.[11]

Allotropes are different structural modifications of an element.[12] The family of carbon allotropes includes diamond - carbon atoms arranged in a cubic lattice or tetrahedral - and graphite - characterized by stacked sheets of carbon atoms organized in a hexagonal lattice.[13] These solids have outstanding properties in terms of hardness,[14] conductivity,[15, 16] and friction.[17] Nevertheless, new carbon allotropes were predicted, synthesized, and characterized during the last decades, showing more exceptional properties. These materials are known as nanocarbons, and they include fullerene, carbon nanotubes, and graphene.[18]

Nanocarbons research promises to provide the next generation material that will be more sustainable and perform better in different application. For example, carbon nanotubes were reported as having exceptionally high Young's modulus by Treacy et al. in 1996 and different potential applications by Baughman et al. in 2002.[19, 20] Few years later, Lee et al. measured graphene elastic properties and intrinsic strength, demonstrating that it was the strongest material ever measured.[21] In addition, graphene was reported to have unique electronic properties by Novoselov et al. in 2004.[22] These outstanding characteristics pushed academic research to focus extensively on the fundamental and applied study of these materials (see **Figure 1.1**) and many references from their study will be included in this work.

Parallel to crystalline and nano allotropes of carbon, amorphous allotropes of carbon - defined as carbon materials without a long-range order - have an essential role in our society. Coal has been the first fossil fuel used by humans since ancient times - the name carbon derives from the Latin name of coal: *carbon* - and it led to the first industrial revolution during the Eighteenth Century.[23] Carbon fibers are widely used to produce light materials with superior mechanical properties.[13] Porous carbons have almost uncountable applications as energy storage devices,[24, 25] adsorbents for pollutants,[26, 27] and heterogeneous catalysis.[28]

Despite their numerous applications, amorphous carbons struggled to get popularity as high as the crystalline and nano analogs in fundamental research. Indeed, **Figure 1.1** reports the number of publications per year from Web of Science, and it shows how fundamental research focused mostly on nanocarbons, with a peak of publications in 2019 equal to 39132 (107 publications per day) only on graphene. In the same year, porous carbon got the same

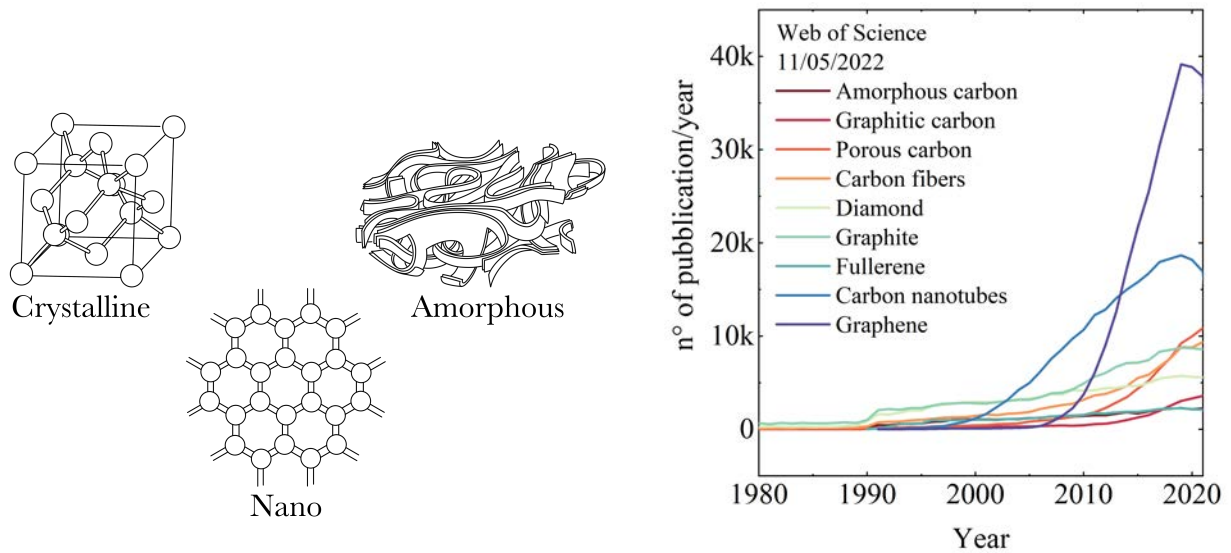


Figure 1.1: (On the left) Graphical representation of crystalline, amorphous, and nano carbons structures, and (on the right) number of publication per year from Web of Science in 2022.

amount of scientific publications as graphite for the first time in history as a result of a constant increment of research on the topic from 2010.

Interestingly, the number of graphene and carbon nanotubes publications showed a downward trend in 2020 and 2021, while porous carbon and carbon fibers value still has a positive derivative in the same time frame. Even though one might think that the downward trend for these nanocarbons is significant, it is unlikely that such promising materials will disappear from fundamental research. Still, instead, it will equilibrate to a more reasonable number. Nevertheless, the increasing interest in understanding porous carbons - and amorphous allotropes in general - is understandable not only by the rising number of publications but from daily interaction with colleagues in the department and outside of it.

The potential of amorphous carbon materials relies on their easy preparation method, which involves the heat treatment at a high temperature of organic precursor. During this process, small molecules such as water, carbon dioxide, or ammonia are generated from the precursor decomposition favoring the formation of C-C bonds.[13] These are stable at the working temperature and results in a disordered carbon network. Different studies tried to provide a model to describe accurately this disordered structure.[29–32] Yet, a comprehensive and accepted understanding is still missing among researches.

Despite the lack of precise knowledge on their structure, carbon materials are characterized by a wide range of tunable properties which can be adjusted by the ambient conditions of the synthesis (e.g., working temperature, heating rate, atmosphere, etc.),[33–37] the type of precursor (e.g., glucose, MOFs, polymers, etc.),[38–40] the kind of additive during the synthesis (e.g., templates, metals, salts, etc.),[41–44] or even modifying the structure with a post-treatment

(e.g., metal impregnation, surface activation, etc.).[45–48] The resulting materials will differentiate by the morphology on a macro scale (e.g., powders, membranes, monoliths, fibers, etc.),[49–53] on the micron scale (e.g., colloids, sheets, etc.),[54, 55] and the nanoscale (e.g., porosity, graphitic stacking, etc.),[56–58] or by the composition (e.g., oxygen, nitrogen, boron, etc. doping or metal decoration),[59, 60] and the chemical structure (e.g., carboxylic acids, quaternary nitrogen, carbene-like sites, etc.).[61–63]

All these variables interact with each other in a dynamic equilibrium (**Figure 1.2**). Hence, it is not an easy challenge to modify one without affecting the others, and carbonization remains a black box for this reason. As a long-term goal, the carbon community is trying to increase the knowledge and control of this process to produce a more specific carbon-based material for the targeted application. For example, decreasing the carbonization temperature is a promising strategy to gain control over the chemical reactions involved in the process. Hydrothermal carbonization is one example of such strategy as its working temperature is usually lower than 200 °C.[64] Differently, this work will pursue systematic research over a conscious selection of molecules with similar chemical structures. In particular, it aims to expand the experimental data connecting precursor, synthesis conditions, and final materials properties, providing general guidelines to control the synthesis of highly doped porous carbonaceous materials.

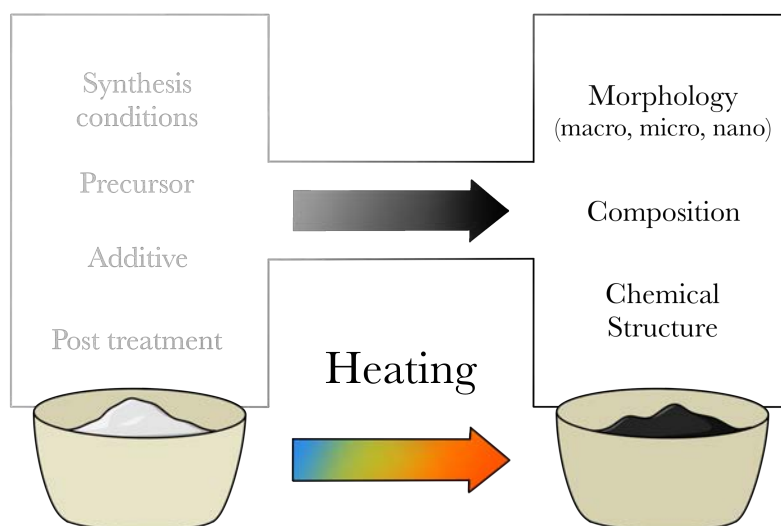


Figure 1.2: Graphical representation of the variables controllable and parameter measurable during the carbonization process.

1.2.2 Control of the porous structure

Porous materials are widely used in multiple applications such as gas capture, energy storage, or heterogeneous catalysis.[65] Their role in materials science is central, and so is the part of porous carbons among porous materials. According to the IUPAC guidelines,[66] they are classified as a function of the diameter of their pores (d):

- Microporous materials: $d \leq 2 \text{ nm}$
- Mesoporous materials: $2 \text{ nm} < d \leq 50 \text{ nm}$
- Macroporous materials: $d > 50 \text{ nm}$

In carbon-based materials, porosity can be controlled through different strategies (**Figure 1.3**) and the most popular are: activation and templating.[67] In general terms, activation methodologies use a chemical agent to promote material decomposition and the consequent formation of pores in the structure. On the other hand, templated methods use an additive to guide the construction of the desired nanoscale pores.

Activation methods are considered well-established top-down approaches to generate porosity in carbon-based materials. Based on the physical state of the activating agent, they are often divided in two class: *physical* (gaseous agent) or *chemical* activation (solid or liquid agent).[68] More in detail, physical activation implies a two-step synthesis during which the material is first synthesized, and CO_2 or steam are successively used to decompose it.[69] Differently, chemical activation implies that the activating agent (e.g., ZnCl_2 , KOH , etc.) is used to impregnate the material precursor, and their mix is submitted to the heat treatment.[45, 70, 71] After chemical activation, the additive must be washed out from the final product. Even though they have both distinctive advantages and disadvantages, activation methods stand for simplicity, but they lack control and tunability of the pore structure. Indeed, only microporous materials can be obtained from the decomposition of the material structure, while no meso- or macropores can be developed through these methods.

Templating methods are optimal for higher control over the porosity than the activation method. They use a structure-directing agent to give a preferential shape to the final material.[72, 73] Once the material is developed, the agent can be removed, leaving a hollow structure - the porous structure - in the material. The templating methods can be differentiated as *soft* or *hard* depending on the ability of the structure-directing agent to maintain its shape. Generally, a soft template is obtained by self-assembly, and it decomposes easily once the materials are formed.[74, 75] Differently, a hard template has a robust structure that needs to be produced before the material synthesis.[76–78] The hard template does not decompose upon synthetic conditions but has to be removed afterward. Similar to activation, templated methods hold a specific trade-off which need to be balanced depending on the needs. Indeed, the higher control over the final porous structure demands a higher energy investment in the synthesis compared to activation methods.

An alternative to these two methods is sol-gel synthesis.[79–82] This is based on a monomer solution, which starts to condensate upon defined conditions. The polymer formation increases the viscosity of the system and the precipitation of longer chains up to the formation of a gel. The solvent can be removed from the gel upon drying, leaving a hollow structure: the porous material.[83] This synthesis is widely used for organic and inorganic polymers; the most famous application is silica production. The final porosity is dominated by the polymerization of the initial monomer, which is a widely known and controllable process. Hence, sol-gel synthesis has a higher level of control over the porosity and lower energy demand compared to the previous two methods. Nevertheless, its application in producing carbon-based materials is not trivial. Even though there are numerous examples in literature that used this method to synthesize materials precursors, the stability of the porous network is not always kept, and the heating process might lead to its collapse.[84, 85]

In 2013, a novel synthetic method was developed by Fechler et al. to produce porous carbon materials: salt melt templating.[42] This process exploits a salt as an additive to the carbon precursor. In an ideal synthesis, the salt melts before the precursor starts to react, promoting the formation of a solution. When the temperature increases, the precursor in the solution begins to react with itself, forming first a polymer and second a carbon material.[86] Even though the process is still debated,[87] the ideal material formation is similar to a sol-gel-like process.[88] Once the synthesis is concluded, the salt can be washed out by acid at room temperature, leaving a porous structure in the materials.

Salt melt templated synthesis is difficult to classify in the last three categories as it merges all their characteristic points. Like soft-templating, the structure-directing agent does not need to be synthesized before the synthesis. It can be removed easier than hard templating (often HF is used during this process). The synthesis has tunable parameters (e.g., type of salt, heating

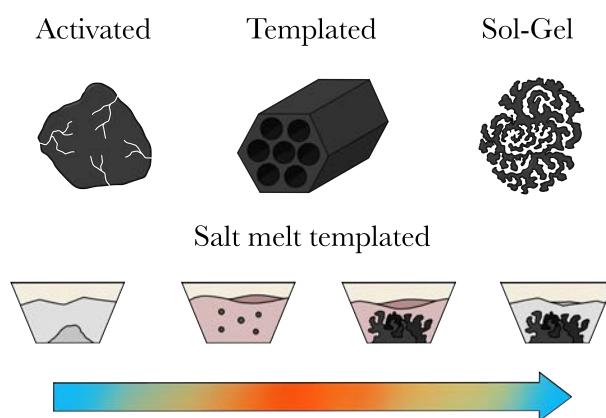


Figure 1.3: Schematic visualization of different strategies towards porous carbons.

temperature, etc.) which can be adjusted to gain higher control over the final result. The salt can contain an activating agent to promote the formation of micropores.

Nevertheless, due to its recent invention, few key parameters are understood clearly and the salt melt templated synthesis is still mainly used as a black box.[87] For example, the leading factor in the generation of pores is still under debate between the sol-gel-like process or the activation. Similarly, it is unclear how much the precursor or the salt's nature affects the final results or which is the actual mechanism behind the material formation. For these reasons, this thesis aims to expand the library of the materials produced by this synthesis to provide further experimental data while developing novel carbon-based materials.

1.2.3 Control of the composition

Doping is the action of adding a small amounts of foreign atoms to form a solid solution in the lattice of a non-metallic catalyst.[89] The ability of carbon to bind different elements enables a wide choice of dopants, and the most common are oxygen, nitrogen, boron, sulfur, and phosphorous.[59] Over the last 10 years, the understanding of doping improved remarkably for carbon-based materials thanks to numerous experimental and theoretical works on graphene as a model material for energy storage devices or catalysis.[90, 91] Among the different elements, this thesis will focus on nitrogen, but further information beyond nitrogen doping might be found in the literature.[59]

Nitrogen is a nonmetallic element, and its atomic number is 7. Its elemental form is gaseous, and 78% of the earth atmosphere is composed of it. Compared to carbon, it has one electron more in the valence shell and, nitrogen presents higher electronegativity than carbon. From nitrogen doping, one might expect the surface polarization and material conductivity to increase.[92–94] Indeed, these effects were observed and served the application of N-doped carbon-based materials for various applications.[95, 96]

Nevertheless, the bond affinity between nitrogen and carbon allows the development of materials with a broader composition range compared to traditional doping (**Figure 1.4**). Among these materials, carbon nitrides (C_3N_4) are probably the most famous due to their semiconductor properties and photocatalytic activity.[97] C_3N_4 are an entirely different phase compared to N-doped carbons, and it proves the wide range of materials obtainable from organic molecules upon heat treatment.[98] For this reason, the composition control must be central and conscious to foster the desired material characteristics.

Similar to pore structure control, different strategies can increase heteroatom content in carbon-based materials.[38] Among them, post-synthesis methods are standard and use either the heat treatment in nitrogen-containing gases or the decomposition of nitrogen-containing molecules on the material surface.[99–101] Both strategies rely on the temperature to generate active sites, which will react with nitrogen-containing species increasing the doping level.[102] Their main

advantage is to use a pre-synthesized material that might undergo mild modification apart from the doping. Nevertheless, the heteroatom content can hardly go above 10 wt% and, due to the two-step synthesis, their costs rise and limits the exploitation to a larger scale.

Differently from post-synthesis methods, using nitrogen-containing carbon precursors might lead to higher nitrogen content materials.[38] For example, g- C_3N_4 was obtained from the heat treatment of melamine.[98] Hence, different polymers and metal-organic frameworks (MOFs) characterized by a high starting nitrogen content can be used as carbon precursors.[39] Nevertheless, the need to synthesize a material before the heat treatment makes this strategy less favorable than molecular precursors direct carbonization.

In this context, Antonietti et al. proposed the concept of *noble carbons* in 2018.[103] The authors described that the wise choice of molecular precursor with high oxidation potential leads to carbon-based material with a low HOMO level comparable with gold - from here, the adjective noble. From this concept, nucleobases, ionic liquids, and many dyes were identified as good, noble carbon precursors, and they all shared the presence of conjugated or aromatic heterocycles. In particular, these functionalities hinder heteroatoms from leaving the structure as small molecules and foster their integration into the material structure.

The work of Kossmann et al. proved these statements correct and produced a novel class of carbon nitrides with a C_1N_1 chemical structure from guanine.[104] The authors further proved that starting from nucleobases or nucleobase-like precursors, it is possible to develop materials with surprisingly high carbon dioxide selectivity and high water adsorption.[105, 106] This thesis will directly follow their research, focusing on the synthesis of high-nitrogen-content carbonaceous materials (i.e., from 10wt% to 30wt%, C_7N to C_3N) and their application in electrical storage devices and catalytic applications.

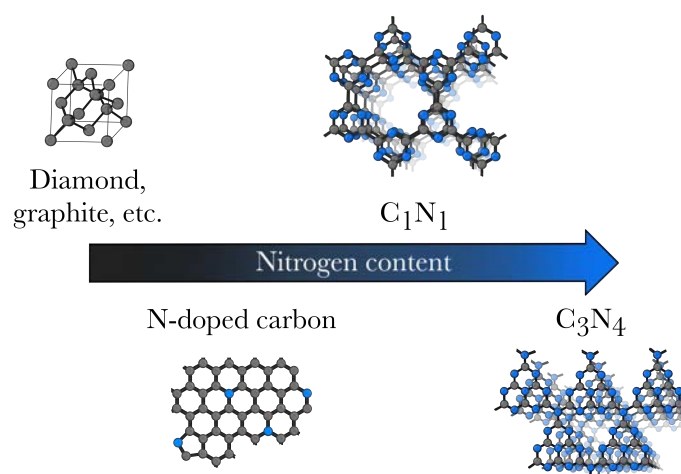


Figure 1.4: Schematic visualization of different carbon-based materials with increasing nitrogen content.

1.3 Electrochemical energy storage

1.3.1 Devices for electrochemical energy storage

As previously introduced, carbon dioxide emission is an urgent problem, and material scientists are committed to find a solution. Among the possibilities, the implementation of renewable energy sources (e.g., solar energy, wind energy, etc.) and the further electrification of our society are the most promising in terms of economic cost and social acceptance.[10] Both alternatives depends on electrical energy storage devices to provide a continuous flux of energy from discontinuous natural sources and to compete with fossil fuel based technologies. Hence, these devices gained higher and higher interest from fundamental science to police makers and multinational companies (e.g., Tesla, Toyota, etc.).

Energy storage devices are usually described by their energy and power densities accordingly to the Ragone plot.[107] In particular, conventional electrical energy devices are limited by the trade-off between energy density and power density. On one hand, batteries utilize two different redox reactions occurring on the opposite electrodes and provide high energy density and low power densities.[108] On the other hand, conventional capacitors use the polarization of two conductive materials giving high power density but low energy density.[107] Increasing the speed of batteries or the energy storage of capacitors has been a central topic for the last decades and numerous studies can be found in literature.[109]

Electrochemical capacitors - or supercapacitors - rose up from these studies by using surface adsorption of charges to store electrical energy as electrochemical energy.[110, 111] This process provides higher power than batteries and higher energy densities than capacitors. Hence, electrochemical capacitor are considered complementary devices to the two previous examples. Moreover, the surface storage assures only minor electrode modification during operation and results in long cycle life. They are generally classified based on the charge adsorption mechanism which can be electrostatic (in electrical double-layer capacitors) or faradic (in pseudocapacitative materials).[112] Nonetheless, it is often difficult to differentiate this two processes which can happen simultaneously.

A different classification of electrochemical capacitors is based on their electrode configuration. This can be symmetrical - the two electrodes have the same capacitance - or asymmetrical - the two electrodes have different capacitance values.[113] In particular, asymmetric electrochemical capacitor uses different storage mechanism at each electrode to provide higher power and energy densities. Among the different combinations, hybrid electrochemical capacitor are based on one battery-like electrode and one capacitor-like electrode and attracted high interest over the last decades.[114] In particular, Li-ion capacitor are among the most popular hybrid electrochemical capacitor. They were first introduced by Anatucci et al. in 2001 and are now commercially available from several companies.[115]

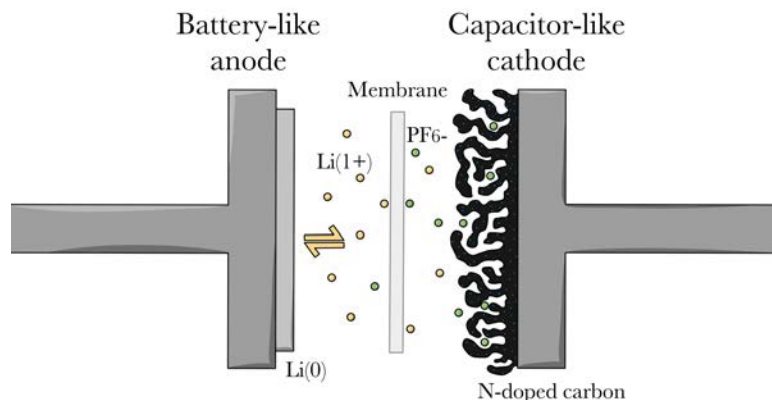


Figure 1.5: Graphical representation of an ideal ion capacitor.

Li-ion capacitors are based on a Li-intercalating phase as battery-like electrode (anode), a carbon material as capacitor-like electrode (cathode), and LiPF_6 in organic carbonate as electrolyte. Upon charging, the Li^+ is intercalated in the anode while PF_6^- is adsorbed on the cathode surface.[116] Ongoing research is focusing on the investigation of different materials for anodes and cathodes in order to maximize the energy and power densities, while different electrolytes are being tested in order to improve the environmental impact and safety of these devices. In particular, this thesis will focus on the preparation composite materials for cathodes.

1.3.2 Carbon materials for electrochemical energy storage

As previously introduced, carbon-based materials presents multiple favorable physical and chemical properties. They are relative cheap, conductive, easy to process and they have a wide rage of tunable properties. For these reasons, they are highly used in electrical energy storage devices (e.g. graphite in batteries, porous carbons in EDLCs). Even though nanocarbons were used as cathode showing good performances, their high production price is still hindering their commercialization. On the other hand, activated carbons (AC) are the first choice for the electrode material and it is the only one which has been commercialized. Hence, the further improvement of Li-ion capacitor is focused on the activated carbon characteristics rather than exploring novel materials.[117]

Activated carbons are characterized by fast kinetic of adsorption/desorption of ion which provides high power densities devices. Nonetheless, the energy stored by ion adsorption is still lower compared to redox processes used in batteries. To improve the energy densities, increasing the amount of charges adsorpted on the material surface is crucial and this can be achieved by three strategies: control of the porous nanostructure, heteroatom doping, and high

conductibility.[118] More in detail, porous structure influence the ion diffusion increasing the surface accessibility. Similarly, heteroatom doping can improve the wettability of the material, its conductivity and the interaction between ions and surface. On the other hand, higher conductivity allows to have higher current at lower potential.

In this context, the control over porosity and composition mentioned in the previous sections are essential tools to prepare carbon-based materials with favorable properties for Li-ion capacitor. Salt melt templating synthesis allows to generate high specific surface areas and hierarchical pores structures starting from molecular precursors. Nucleobase derived materials were reported as highly doped carbonaceous materials. Indeed, in 2018, Antonietti et al. identified noble carbons as promising electrodes for EDLCs.[103] This statement was further repeated by Simon and Gogotsi in 2020 which highlighted the role of oxidation resistance and conductivity. [111]

Nonetheless, the high nitrogen content of noble carbons might promote a decrease in conductivity. Oschatz et al. discussed this as the *functionality-conductivity dilemma* and proposed using composite materials as a possible solution.[119] In particular, the authors discussed the potential of mixing an active phase with a conductive phase to provide composite materials, merging the advantages of both phases. For example, Feng et al. published a method to synthesize nitrogen-doped materials over a graphene layer. The resulting composite material showed improved performances compared to the single components for EDLCs and Li-ion capacitors.[120, 121] Nonetheless, the high costs associated with the starting materials and the synthetic procedure might hinder the applicability of similar approaches. In 2021, Ilic et al. used ball milling as a cost-efficient mixing process to obtain a composite material from tannic acid and conductive carbon.[122] Despite criticism over the not efficient mixing of the two phases,[119] the authors reported a higher performance for the composite materials in lithium-based energy storage devices.

Following Ilic et al., harsher ball milling conditions are needed to promote the development of Li-ion capacitors by ensuring a good contact area between the active and conductive phases. Yet, such conditions might induce materials oxidation, resulting in their deactivation. Hence, using noble carbons is ideal for testing the potential of ball milling in the electrode preparation and verifying the predicted resistance against oxidation of such materials.

1.4 Heterogeneous catalysis

Catalysis is the process that increases the rate of a reaction without modifying its overall standard Gibbs energy change. A catalyst is the substance that promotes such a process while preserving its chemical nature before and after the reaction.[123] Chemical industry uses catalysts in 90% of the processes to speed up reactions and reduce the energy consumption.[124] Catalysis is also essential to decompose pollutants (e.g., the catalytic converter in cars or water waste treatment) or promote novel energy sources (e.g., fuel cells or zinc-air batteries).

Recently, the catalytic upgrading of waste (e.g., carbon dioxide reduction or chemical recycling of polymers) attracted attention in the scientific community as a potential promoter of a cyclic economy. Hence, catalysis is doubtless an essential tool toward a more sustainable society without losing industrial development's privileges.

Catalysis is usually divided into two categories depending on the physical state of the catalyst: *homogeneous catalysis*, which studies the process of a catalyst in the same phase of the reagents, and *heterogeneous catalysis*, which investigates the function of a catalyst in a different phase compared to the reagents.[123] Nonetheless, a third category called *enzymatic catalysis* is often used to identify the catalytic processes promoted by enzymes.[125] In particular, when developing more sustainable processes, these three catalysis categories must be analyzed by their advantages and disadvantages (**Figure 1.6**). Homogeneous catalysis is notorious for its high atom efficiency, high turnover frequencies, and high selectivity. However, separating the catalyst from the reaction media is complex, energy-demanding, and, hence, less convenient than the other two categories. Heterogeneous catalysis is characterized by the easy separation of the catalyst from the reaction media because of their different phases. However, the reagents surface adsorption and the products surface desorption limit the activity that is generally lower compared to an homogeneous catalyst. Moreover, selectivity is often an issue due to the defective nature of the material surfaces. Enzymatic catalysis presents both an easy separation and high activity/selectivity, but its performance is highly susceptible to the reaction conditions, leading to a fast deactivation.

This thesis will focus on heterogeneous catalysis because of its relevance for industrial application (80% of the industrial catalytic processes are heterogeneous) and the need for a more reliable description of active sites on the surface.[124] In particular, it is crucial to understand structure-performance relationships and identify strategies to improve catalysts activity, similar

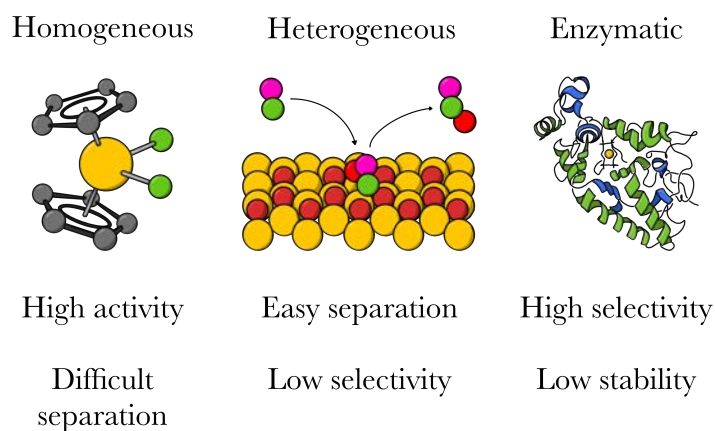


Figure 1.6: Schematic visualization of different categories of catalysis.

to homogeneous catalysis. Nonetheless, this can be achieved through challenging solid surface characterization, which involves sophisticated instrumental techniques (e.g., gas adsorption, electron microscopy, X-ray absorption, etc.) and needs higher investigation.

Moreover, heterogeneous catalysis often relies on heavy and noble metals. These are expensive, their synthesis is a highly polluting process, and their stability is problematic in transitioning to more sustainable reaction conditions (e.g., they are sensitive to water or sulfur). Hence, in the context of this thesis, it is a mandatory endeavor to find alternatives to reduce or remove their use in heterogeneous catalysis.[126] To this goal, two strategies (i.e., *carbocatalysis* and *single-atom catalysis*) will be described and investigated to determine their structure-performances relationships and determine the active surface sites.

1.4.1 Carbocatalysis

Carbocatalysis studies the activity of carbon-based materials in heterogeneous catalytic processes. Even though this activity has been reported in the literature for over a century,[127] it has gained more and more attention only over the last decade.[126] In particular, its popularity raised after the noble prize to graphene and the understanding of the high activity for electrochemical processes when nanocarbons are used in the electrodes.[126, 128] Combined with the need to reduce the use of noble metals; these two factors increased the awareness of the potential of carbon-based materials for catalysis.

More in detail, in 2009, Gong et al. first reported the high activity towards electrochemical oxygen reduction by nitrogen-doped carbon nanotubes array.[129] Similarly, in 2010, N-doped graphene was shown as active for the same reaction.[130] From 2013, different metal-free carbon-based catalysts were reported as active for oxygen evolution reaction (OER),[131] carbon dioxide reduction reaction (CO₂RR),[132] hydrogen evolution reaction (HER),[133]. After these vanguard works, numerous papers were published, expanding the understanding of the active sites and the possible applications as reported in different reviews.[134, 135] Nevertheless, among this rich literature, the work of Guo et al. stands as one of the best for the active site determination in the ORR with nitrogen-doped carbon materials.[136]

Different from electrocatalysis, chemocatalysis with carbon-based materials has much older literature.[137, 138] Indeed, oxidation reactions catalyzed by amorphous carbon or graphite are often the first example cited by reviews when a historical perspective is given. Among these, the oldest example was reported in a work from Antonietti et al.,[126] which refers to the oxidation of organic gases by activated carbon written by J. Stenhouse in 1855.[127] As well as oxidation reaction, reduction reaction catalyzed by similar materials can be found from 1985.[139] Yet, these germinal works consider carbon surfaces as electron transfer platforms rather than mentioning the possible activation of the reagents.[140] The absence of this concept hindered the development of carbon-based catalysts favoring the more active metal-based catalysts.

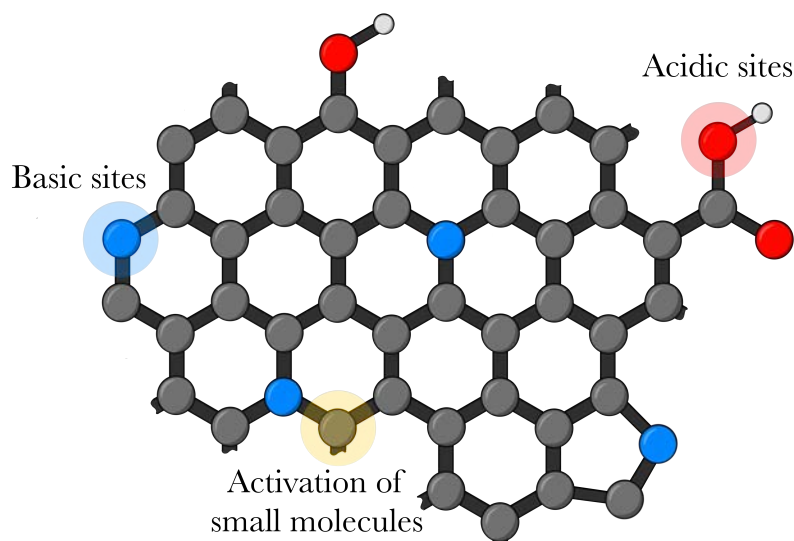


Figure 1.7: Schematic visualization of different functionalities and their activity in carbocatalysis.

The graphene trend mentioned before changed this view. Together with electrocatalysis and photocatalysis, more and more information about the activation of molecules by functionalized carbon surfaces was collected in the literature.[141] Nanostructured carbon-based materials such as graphene,[142] graphene oxide,[143] reduced graphene oxide, carbon nanotubes, and carbon nanodots were found to catalyze oxidation, reduction, and acid/base reactions.[126, 128, 144] More in detail, by the use of these materials, it is possible to catalyze efficiently: the oxidation of alcohols,[145] of α -C-H bond of ethylbenzene,[146] and benzene,[147] reduction of nitroarenes with hydrazine,[148] different coupling reactions,[149–151] transesterification,[152] hydrolysis reactions,[153] Knoevenagel condensations.[154]

Even though most of the papers use nanocarbons inspired by their surprising properties, the presence of specific functionalities (e.g., unsaturated edges, quaternary nitrogen, carboxylic acid, etc.) appears to be crucial when their catalytic performances are considered (**Figure 1.7**).[155] For example, the activation of small molecules for oxidation reactions is often correlated to oxygen or nitrogen functionalities.[156] Indeed, nitrogen is reported to withdraw electron density from the carbon next to it and helps the formation of radical oxygen species from hydrogen peroxide (H_2O_2) or tert-butyl peroxide (tBuOOH).[157, 158] Moreover, basic properties are known to be improved when nitrogen doping is implemented in the materials, thanks to pyridinic-like nitrogen functionalities.[159, 160] Similarly, acid properties can be enhanced by inserting oxygen or sulfur functionalities.[161, 162] In particular, the sulfonation of carbon-based materials gave the most promising acid properties compared to metal-based catalysis, even though their stability under reaction conditions is still a problem.[163]

This extensive research highlighted the potential of carbocatalysts and their limitations. Indeed,

their use is often related to high catalyst loading, and their activity rarely outperforms the metal analogs.[141] In addition, using mainly nanocarbons is detrimental in terms of price as they are the most expensive among the known carbon allotropes.[164] Moreover, severe criticism over metal-free claims and role of the heteroatoms was recorded by the scientific community.[165, 166] Hence, further research is needed to confirm the activation mechanism of these catalysts and improve their performances in activity, selectivity, and stability.

Accordingly to the up-to-date knowledge, increasing the heteroatom content is a straightforward strategy to improve the catalytic properties (e.g., graphitic carbon-nitride). Indeed, most of the catalytic activity rises from the presence of heteroatoms in the carbon backbone. Yet, few reports consider this approach due to the synthetic limitations mentioned before, and the nitrogen doping between 10 wt% and 30 wt% is underrepresented in the literature. It is essential to note that such high nitrogen content might profoundly influence the material's nature and drastically change its performance. Hence, this thesis will focus on investigating the catalytic properties of such carbonaceous materials.

1.4.2 Single-atom catalysis

Single-atom catalysis studies the activity of isolated metal atoms anchored on solid supports.[167] Despite similar catalysts having been investigated over the last century under different names (i.e., metal doped carbon, highly dispersed metal, impregnated carbon, etc.),[168–170] the introduction of the single-atom catalyst definition by Zhang et al. in 2011 can be described as a watershed in the field.[171] Indeed, a rich literature has built up since 2011 covering multiple metal atoms, supports, and applications under this definition.[172–174] Compared to older works, the recent advancement in atomic-resolution characterization techniques, theoretical modeling, and *in operando* investigations were central in the development of the field, providing a clear description of atom dispersion, coordination environment, and oxidation state.

Downsizing the metal dispersion from nanoparticles to isolated atoms is a relevant challenge to improve atom efficiency and selectivity in heterogeneous catalysis (**Figure 1.8**).[167] Indeed, while only surface atoms are potential active sites in nanoparticle dispersions, all metal atoms are potential active sites in single atoms distributions. In addition, nanoparticles might give low selectivity because faces, edges, and corners can promote different reactions at different rates. On the contrary, isolated atoms selectivity will depend on their coordination environment, which ideally is controllable and homogeneous. For these reasons, single-atom catalysts are considered a potential bridge between heterogeneous, homogeneous, and enzymatic catalysis.[173]

Despite the promising properties, implementing SACs as an alternative to nanoparticle-based catalysts is still held by numerous challenges. In first place, isolated metal atoms have high internal free energy and tend to aggregate spontaneously into nanoparticles. Hence, single-atom catalysts are often characterized by low loading (≤ 5 wt%) to prevent aggregation.[175] This

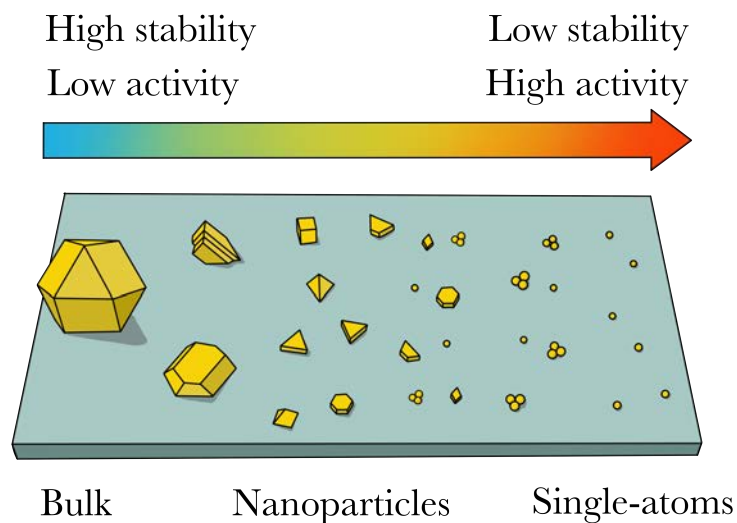


Figure 1.8: Schematic visualization of bulk to single-atom distribution supported on an ideal surface.

low loading limits the absolute activity of the catalyst and makes SACs less competitive for industrial applications. Increasing the metal loading above 5wt% is a direct strategy to foster better performances. Yet, it is still challenging and only a few reports can be found in the literature.[176]

To obtain isolated atoms at high loading, the type of support and synthesis are the two most crucial parameters to consider. Heteroatom-doped carbon-based materials outnumbered the other supports (e.g., metal oxide or metals) in terms of publications and interest.[177] Their popularity arises from the ability of nitrogen, oxygen, or sulfur to coordinate and stabilize metal atoms preventing their aggregation. Moreover, they can easily be synthesized by convenient bottom-up approaches that require few synthetic steps. Hence, the carbonization of small molecules containing metals or pre-prepared materials became a widely used synthetic approach for high-loading SACs.[178, 179] Among the different reports, the work of Zhao et al. from 2018 stands out by because they reported a one-step synthesis of Ni-SAC with 20 wt% of loading and activity for CO₂RR with high Faradaic efficiency.[180]

Even though bottom-up approaches provide easily high loading of isolated atoms, the accessibility of the metal sites is not always ensured because the metal atoms might be included in the structure during the synthesis.[174] Moreover, the metal coordination environment is challenging to control, and different active sites might be found. For example, the work of Zhang et al. demonstrated that, among various Fe sites, only the unsaturated ones were the active sites for the oxidation of ethyl benzene.[181] Hence, SACs derived from bottom-up approaches hold

similar problems to the nanoparticle-based catalyst as (1) not all the metal distribution is active and (2) the absence of single active sites due to the inhomogeneous coordination environment.

Alternative to bottom-up, top-down methods are characterized by a two-step approach that involves synthesizing support material and its post-decoration.[182] These methods favor the metal sites surface distribution, improving their accessibility. As discussed, top-down methods are less efficient in metal loading than bottom-up approaches, but few key parameters can be tuned to improve their performance. For example, by adjusting the specific surface area and the heteroatom content of the materials, it is possible to generate enough spatially distanced binding sites, which prevents the atoms aggregation.[176, 183] To this goal, salt melt templating synthesis with wisely chosen precursors is an ideal strategy for the support preparation as high specific surface area and high heteroatom content can be obtained.

Top-down methods can be classified as gas-phase techniques, electrochemical methods, and wet-deposition. Gas-phase techniques (e.g., mass-selected soft-landing, physical vapor deposition, and atomic layer deposition) are characterized by high control over the atomic distribution. However, they are expensive and difficult to scale up. Electrochemical methods are less costly than gas-phase techniques and still present reasonable control. Nonetheless, they are subjected to easy cross-contamination, and the atoms' adhesion is weaker than in the other two methods. Wet-deposition is economically favorable, involves easy synthetic steps, and has high potential scalability. Nonetheless, it lacks control over the chemical environment of the single sites and can give spatially inhomogeneous distributions.[174]

In this context, increasing the control over wet-deposition methods is the primary goal to promote their use in SACs synthesis. Similar to carbon-based materials, the wise choice of the precursors is central because it can influence the atoms dispersion and adhesion over the support surface. The most common and effective anchoring sites are nitrogen atoms, which present favorable interaction with metal atoms.[168] Hence, complexes with nitrogen ligands (e.g., porphyrins, bipyridines, etc.) or metal salts mixed with nitrogen-containing heterocycles are the ideal choices to favor the atomic dispersion in carbon-based materials.[184, 185] Moreover, nitrogen-coordinated metals were shown to be more active than the homogeneous counterpart in Suzuki couplings,[186] and good electrocatalysts for HER, OER, ORR, CO₂RR, and nitrogen reduction reaction (NRR).[187]

Among the different metals, this thesis will focus on nickel for its broad catalytic properties, relatively low cost, and central role in catalysis. Indeed, Paul Sabatier used nickel to conduct his first studies on ethylene reduction reaction, leading him to the Nobel Prize in chemistry in 1912.[188] Even though he described nickel as difficult to control, this metal is known nowadays as a good catalyst for couplings reactions,[189], reduction,[190] and oxidation reactions.[191] Moreover, nickel has been highly investigated for single atom catalysts in HER,[192] OER,[193] ORR,[178] CO₂RR,[194] electrochemical dechlorination,[195] methanol oxidation,[196] lithium-

sulfur batteries,[197] photocatalytic reduction of CO₂,[198] reverse water-gas shift reaction,[199] dry reforming of CH₄,[200] selective hydrogenation,[201] and cellulose valorization.[202]

In particular, nickel single-atoms supported on N-doped carbon nanotubes showed higher catalytic activity than Ni nanoparticles for the electrocatalytic reduction of CO₂ to CO with almost 99% Faradaic efficiency.[203, 204] Hong Bin Yang et al. identified Ni(I) coordinated by four nitrogen atoms as the origin of the superior activity of nickel single-atoms for CO₂RR.[194] In 2019, Yun-Nan Gong et al. contradicted this result and suggested that the nickel coordination environment plays a more important role.[205] The authors identified that Ni(II) coordinated by two nitrogen atoms and two carbon atoms (Ni-N₂C₂) is more active compared to more nitrogen-rich coordination environments (i.e., Ni-N₃C or Ni-N₄). In contrast, Xin Rong et al. highlighted the role of atom vacancy in the nickel coordination environment as a leading factor in improving atom nickel catalytic activity.[206] Hence, despite the numerous work and advanced characterizations, the effect of the nickel oxidation state and its coordination environment is still under debate, and further investigations are needed.

Interestingly, oxygen-rich coordination environments are not found among these studies because similar coordination is less common for nickel dispersion on carbon surfaces. Nonetheless, their effect on a different reaction (i.e., ORR) was reported in two independent papers by Xiaozhe Song et al. and Yulin Wang et al. in 2020.[207, 208] These works indicated that oxygen-coordinated nickel atoms are optimal catalysts for the oxygen reduction to hydrogen peroxide. In contrast, nitrogen-coordinated nickel atoms promote the complete reduction of oxygen to water.[209] In 2017, Pander III et al. described in their review the potential of metal oxide for CO₂RR, suggesting the role of the metal-oxygen coordination environment.[210] In particular, these materials exceed the theoretical expectations of kinetic stability and product distribution. Hence, the investigation of oxygen-coordinated nickel single atoms holds a high potential to tune the selectivity from CO to more valuable products such as formic acid, methanol, or methane, which will be discussed in this thesis.

Bibliography

- [1] Hummel, R. E. *The First Materials (Stone Age and Copper—Stone Age)*, 3–11 (Springer New York, New York, NY, 2004).
- [2] Siffert, P. & Krimmel, E. *Silicon: Evolution and Future of a Technology* (Springer Berlin Heidelberg, 2013). URL https://books.google.de/books?id=Qxj_CAAAQBAJ.
- [3] Lord todd: the state of chemistry. *Chemical & Engineering News Archive* **58**, 28–33 (1980).
- [4] The nobel prize in chemistry 2019. *Press release: Nobel Prize Outreach* (2019). URL <https://www.nobelprize.org/prizes/chemistry/2019/press-release/>.
- [5] Hummel, R. E. *Understanding Materials Science: History · Properties · Applications* (Springer New York, New York, NY, 2004).
- [6] Wood, J. The top ten advances in materials science. *Materials Today* **11**, 40–45 (2008).
- [7] Friedman, M. *There's No Such Thing as a Free Lunch* (Open Court, 1975).
- [8] Lacis, A. A., Schmidt, G. A., Rind, D. & Ruedy, R. A. Atmospheric control knob governing earth's temperature. *Science* **330**, 356–359 (2010).
- [9] Stocker, T. *et al.* *IPCC, 2013: Climate Change 2013: The Physical Science Basis. Contribution of Working Group I to the Fifth Assessment Report of the Intergovernmental Panel on Climate Change* (Cambridge University Press, Cambridge, United Kingdom and New York, NY, USA, 1535 pp, 2013).
- [10] Pörtner, H. *et al.* *IPCC, 2022: Climate Change 2022: Impacts, Adaptation, and Vulnerability. Contribution of Working Group II to the Sixth Assessment Report of the Intergovernmental Panel on Climate Change* (Cambridge University Press. In Press, 2022).
- [11] Carbon. *Encyclopedia Britannica* URL <https://www.britannica.com/science/carbon-chemical-element>.
- [12] McNaught, A. D. & Wilkinson, A. *IUPAC. Compendium of Chemical Terminology, 2nd*

- ed. (the "Gold Book")* (Blackwell Scientific Publications, Oxford, 1997). URL <https://doi.org/10.1351/goldbook.A00243>.
- [13] Inagaki, M. & Kang, F. Chapter 2 - fundamental science of carbon materials. In Inagaki, M. & Kang, F. (eds.) *Materials Science and Engineering of Carbon: Fundamentals (Second Edition)*, 17–217 (Butterworth-Heinemann, Oxford, 2014), second edition edn.
- [14] Irifune, T., Kurio, A., Sakamoto, S., Inoue, T. & Sumiya, H. Ultrahard polycrystalline diamond from graphite. *Nature* **421**, 599–600 (2003).
- [15] Collins, A. T., Lettington, A. H. & Steeds, J. W. The optical and electronic properties of semiconducting diamond. *Philosophical Transactions of the Royal Society of London. Series A: Physical and Engineering Sciences* **342**, 233–244 (1993).
- [16] Deprez, N. & McLachlan, D. S. The analysis of the electrical conductivity of graphite conductivity of graphite powders during compaction. *Journal of Physics D: Applied Physics* **21**, 101–107 (1988).
- [17] Dienwiebel, M. *et al.* Superlubricity of graphite. *Physical Review Letters* **92**, 126101 (2004).
- [18] Khan, A., Jawaid, M., Inamuddin & Asiri, A. M. *Nanocarbon and its Composites*. Woodhead Publishing Series in Composites Science and Engineering (Woodhead Publishing, 2019).
- [19] Treacy, M., Ebbesen, T. & Gibson, J. Exceptionally high young's modulus observed for individual carbon nanotubes. *Nature* **381**, 678–680 (1996).
- [20] Baughman, R., Zakhidov, A. & de Heer, W. Carbon nanotubes - the route toward applications. *Science* **297**, 787–792 (2002).
- [21] Lee, C., Wei, X., Kysar, J. W. & Hone, J. Measurement of the elastic properties and intrinsic strength of monolayer graphene. *Science* **321**, 385–388 (2008).
- [22] Novoselov, K. *et al.* Electric field effect in atomically thin carbon films. *Science* **306**, 666–669 (2004).
- [23] Landes, D. S. *the unbound prometheus, Technological change and industrial development in Western Europe from 1750 to the present* (Cambridge University Press, 1969).
- [24] Zhang, L. L. & Zhao, X. S. Carbon-based materials as supercapacitor electrodes. *Chemical Society Reviews* **38**, 2520–2531 (2009).
- [25] Wang, Y., Song, Y. & Xia, Y. Electrochemical capacitors: mechanism, materials, systems, characterization and applications. *Chemical Society Reviews* **45**, 5925–5950 (2016).

- [26] Zhang, X., Gao, B., Creamer, A. E., Cao, C. & Li, Y. Adsorption of vocs onto engineered carbon materials: A review. *Journal of Hazardous Materials* **338**, 102–123 (2017).
- [27] Bhatnagar, A., Hogland, W., Marques, M. & Sillanpaa, M. An overview of the modification methods of activated carbon for its water treatment applications. *Chemical Engineering Journal* **219**, 499–511 (2013).
- [28] Serp, P. & Machado, B. *Nanostructured Carbon Materials for Catalysis*. Catalysis Series (The Royal Society of Chemistry, 2015).
- [29] Crawford, D. & Johnson, D. High-resolution electron microscopy of high-modulus carbon fibres. *Journal of Microscopy* **94**, 51+ (1971).
- [30] Ban, L., Crawford, D. & Marsh, H. Lattice-resolution electron-microscopy in structural studies of non-graphitizing carbons from polyvinylidene chloride (pvdc). *Journal of Applied Crystallography* **8**, 415–420 (1975).
- [31] Robertson, J. Amorphous carbon. *Advances in Physics* **35**, 317–374 (1986).
- [32] Harris, P. J. F. New perspectives on the structure of graphitic carbons. *Critical Reviews in Solid State and Materials Sciences* **30**, 235–253 (2005).
- [33] Antal, M. J. & Grønli, M. The art, science, and technology of charcoal production. *Industrial & Engineering Chemistry Research* **42**, 1619–1640 (2003).
- [34] Li, W. *et al.* Effects of carbonization temperatures on characteristics of porosity in coconut shell chars and activated carbons derived from carbonized coconut shell chars. *Industrial Crops and Products* **28**, 190–198 (2008).
- [35] Üner, O. & Bayrak, Y. The effect of carbonization temperature, carbonization time and impregnation ratio on the properties of activated carbon produced from arundo donax. *Microporous and Mesoporous Materials* **268**, 225–234 (2018).
- [36] Martin, C., Purdy, K., Dubayeh, S., Kerr, C. & GARR, T. The effect of carbonization heating rate on charcoal and active-carbon fields. *Applied Biochemistry and Biotechnology* **28-9**, 21–32 (1991).
- [37] Song, C., Wang, T., Qiu, Y., Qiu, J. & Cheng, H. Effect of carbonization atmosphere on the structure changes of pan carbon membranes. *Journal of Porous Materials* **16**, 197–203 (2009).
- [38] Deng, Y., Xie, Y., Zou, K. & Ji, X. Review on recent advances in nitrogen-doped carbons: preparations and applications in supercapacitors. *Journal of Materials Chemistry A* **4**, 1144–1173 (2016).

- [39] Chaikittisilp, W., Ariga, K. & Yamauchi, Y. A new family of carbon materials: synthesis of mof-derived nanoporous carbons and their promising applications. *Journal of Materials Chemistry A* **1**, 14–19 (2013).
- [40] Dutta, S., Bhaumik, A. & Wu, K. C. W. Hierarchically porous carbon derived from polymers and biomass: effect of interconnected pores on energy applications. *Energy & Environmental Science* **7**, 3574–3592 (2014).
- [41] Benzigar, M. R. *et al.* Recent advances in functionalized micro and mesoporous carbon materials: synthesis and applications. *Chemical Society Reviews* **47**, 2680–2721 (2018).
- [42] Fechler, N., Feller, T.-P. & Antonietti, M. “salt templating”: A simple and sustainable pathway toward highly porous functional carbons from ionic liquids. *Advanced Materials* **25**, 75–79 (2013).
- [43] Liu, S. *et al.* Large-scale synthesis of porous carbon via one-step cucl₂ activation of rape pollen for high-performance supercapacitors. *Journal of Materials Chemistry A* **6**, 12046–12055 (2018).
- [44] Hayashi, J., Kazehaya, A., Muroyama, K. & Watkinson, A. Preparation of activated carbon from lignin by chemical activation. *Carbon* **38**, 1873–1878 (2000).
- [45] Wang, J. & Kaskel, S. Koh activation of carbon-based materials for energy storage. *Journal of Materials Chemistry* **22**, 23710–23725 (2012).
- [46] Deffernez, A., Hermans, S. & Devillers, M. Preparation of carbon-supported pd and au-pd catalysts via optimized adsorption of metallic complexes. In Gaigneaux, E. *et al.* (eds.) *Scientific Bases for the Preparation of Heterogeneous Catalysts*, vol. 162 of *Studies in Surface Science and Catalysis*, 79–86 (Elsevier, 2006).
- [47] Kovach, N. C., Russell-Parks, G. A. & Trewyn, B. G. Strategies for post-synthetic functionalization of mesoporous carbon nanomaterial surfaces. *Microporous and Mesoporous Materials* **329**, 111453 (2022).
- [48] Yin, C. Y., Aroua, M. K. & Daud, W. M. A. W. Review of modifications of activated carbon for enhancing contaminant uptakes from aqueous solutions. *Separation and Purification Technology* **52**, 403–415 (2007).
- [49] Zhu, X. *et al.* Synthesis of porous, nitrogen-doped adsorption/diffusion carbonaceous membranes for efficient co₂ separation. *Macromolecular Rapid Communications* **34**, 452–459 (2013).
- [50] Hu, Y.-S. *et al.* Synthesis of hierarchically porous carbon monoliths with highly ordered microstructure and their application in rechargeable lithium batteries with high-rate ca-

- pability. *Advanced Functional Materials* **17**, 1873–1878 (2007).
- [51] Hao, G.-P. *et al.* Structurally designed synthesis of mechanically stable poly(benzoxazine-co-resol)-based porous carbon monoliths and their application as high-performance CO₂ capture sorbents. *Journal of the American Chemical Society* **133**, 11378–11388 (2011).
- [52] Derbyshire, F. *et al.* Synthesis of isotropic carbon fibers and activated carbon fibers from pitch precursors. *Fuel* **80**, 345–356 (2001).
- [53] Boskovic, B. *et al.* Low temperature synthesis of carbon nanofibres on carbon fibre matrices. *Carbon* **43**, 2643–2648 (2005).
- [54] Paraknowitsch, J. P., Thomas, A. & Antonietti, M. Carbon colloids prepared by hydrothermal carbonization as efficient fuel for indirect carbon fuel cells. *Chemistry of Materials* **21**, 1170–1172 (2009).
- [55] Hou, J., Cao, C., Idrees, F. & Ma, X. Hierarchical porous nitrogen-doped carbon nanosheets derived from silk for ultrahigh-capacity battery anodes and supercapacitors. *ACS Nano* **9**, 2556–2564 (2015).
- [56] Ma, T.-Y., Liu, L. & Yuan, Z.-Y. Direct synthesis of ordered mesoporous carbons. *Chemical Society Reviews* **42**, 3977–4003 (2013).
- [57] Schuepfer, D. B. *et al.* Assessing the structural properties of graphitic and non-graphitic carbons by Raman spectroscopy. *Carbon* **161**, 359–372 (2020).
- [58] Wu, Q., Yang, L., Wang, X. & Hu, Z. From carbon-based nanotubes to nanocages for advanced energy conversion and storage. *Accounts of Chemical Research* **50**, 435–444 (2017).
- [59] Paraknowitsch, J. P. & Thomas, A. Doping carbons beyond nitrogen: an overview of advanced heteroatom doped carbons with boron, sulphur and phosphorus for energy applications. *Energy & Environmental Science* **6**, 2839–2855 (2013).
- [60] Georgakilas, V. *et al.* Decorating carbon nanotubes with metal or semiconductor nanoparticles. *Journal of Materials Chemistry* **17**, 2679–2694 (2007).
- [61] Boehm, H. Surface oxides on carbon and their analysis: a critical assessment. *Carbon* **40**, 145–149 (2002). Third International Conference on Carbon Black.
- [62] Pels, J., Kapteijn, F., Moulijn, J., Zhu, Q. & Thomas, K. Evolution of nitrogen functionalities in carbonaceous materials during pyrolysis. *Carbon* **33**, 1641–1653 (1995).
- [63] Radovic, L. R. & Bockrath, B. On the chemical nature of graphene edges: origin of stability and potential for magnetism in carbon materials. *Journal of the American*

- Chemical Society* **127**, 5917–5927 (2005).
- [64] Titirici, M.-M. & Antonietti, M. Chemistry and materials options of sustainable carbon materials made by hydrothermal carbonization. *Chemical Society Reviews* **39**, 103–116 (2010).
- [65] Sun, M.-H. *et al.* Applications of hierarchically structured porous materials from energy storage and conversion, catalysis, photocatalysis, adsorption, separation, and sensing to biomedicine. *Chemical Society Reviews* **45**, 3479–3563 (2016).
- [66] Thommes, M. *et al.* Physisorption of gases, with special reference to the evaluation of surface area and pore size distribution (iupac technical report). *Pure and Applied Chemistry* **87**, 1051–1069 (2015).
- [67] Lee, J., Kim, J. & Hyeon, T. Recent progress in the synthesis of porous carbon materials. *Advanced Materials* **18**, 2073–2094 (2006).
- [68] Ahmadpour, A. & Do, D. The preparation of active carbons from coal by chemical and physical activation. *Carbon* **34**, 471–479 (1996).
- [69] Molina-Sabio, M., Gonzalez, M., Rodriguez-Reinoso, F. & Sepúlveda-Escribano, A. Effect of steam and carbon dioxide activation in the micropore size distribution of activated carbon. *Carbon* **34**, 505–509 (1996).
- [70] Molina-Sabio, M. & Rodriguez-Reinoso, F. Role of chemical activation in the development of carbon porosity. *Colloids and Surfaces A: Physicochemical and Engineering Aspects* **241**, 15–25 (2004). Proceedings of the Third International TRI/Princeton Workshop "Characterization of Porous Materials: from Angstroms to Millimeters".
- [71] Caturla, F., Molina-Sabio, M. & Rodríguez-Reinoso, F. Preparation of activated carbon by chemical activation with ZnCl_2 . *Carbon* **29**, 999–1007 (1991).
- [72] Inagaki, M., Toyoda, M., Soneda, Y., Tsujimura, S. & Morishita, T. Templated mesoporous carbons: Synthesis and applications. *Carbon* **107**, 448–473 (2016).
- [73] Liang, C., Li, Z. & Dai, S. Mesoporous carbon materials: Synthesis and modification. *Angewandte Chemie International Edition* **47**, 3696–3717 (2008).
- [74] Li, Z., Yan, W. & Dai, S. A novel vesicular carbon synthesized using amphiphilic carbonaceous material and micelle templating approach. *Carbon* **42**, 767–770 (2004).
- [75] Kowalewski, T., Tsarevsky, N. V. & Matyjaszewski, K. Nanostructured carbon arrays from block copolymers of polyacrylonitrile. *Journal of the American Chemical Society* **124**, 10632–10633 (2002).

- [76] Joo, S. *et al.* Ordered nanoporous arrays of carbon supporting high dispersions of platinum nanoparticles. *Nature* **412**, 169–172 (2001).
- [77] Lee, J.-S., Joo, S. H. & Ryoo, R. Synthesis of mesoporous silicas of controlled pore wall thickness and their replication to ordered nanoporous carbons with various pore diameters. *Journal of the American Chemical Society* **124**, 1156–1157 (2002).
- [78] Tanaka, S., Nishiyama, N., Egashira, Y. & Ueyama, K. Synthesis of ordered mesoporous carbons with channel structure from an organic–organic nanocomposite. *Chemical Communications* 2125–2127 (2005).
- [79] Pekala, R. Organic aerogels from the polycondensation of resorcinol with formaldehyde. *Journal of Materials Science* **24**, 3221–3227 (1989).
- [80] Lin, C. & Ritter, J. A. Carbonization and activation of sol–gel derived carbon xerogels. *Carbon* **38**, 849–861 (2000).
- [81] Biener, J. *et al.* Advanced carbon aerogels for energy applications. *Energy Environmental Science* **4**, 656–667 (2011).
- [82] Lee, J.-H. & Park, S.-J. Recent advances in preparations and applications of carbon aerogels: A review. *Carbon* **163**, 1–18 (2020).
- [83] Hench, L. L. & West, J. K. The sol-gel process. *Chemical Reviews* **90**, 33–72 (1990).
- [84] Al-Muhtaseb, S. & Ritter, J. Preparation and properties of resorcinol–formaldehyde organic and carbon gels. *Advanced Materials* **15**, 101–114 (2003).
- [85] Zhang, S. *et al.* The investigation of the adsorption character of carbon aerogels. *Nanostructured Materials* **11**, 375–381 (1999).
- [86] Liu, X., Fechner, N. & Antonietti, M. Salt melt synthesis of ceramics, semiconductors and carbon nanostructures. *Chemical Society Reviews* **42**, 8237–8265 (2013).
- [87] Díez, N., Fuertes, A. B. & Sevilla, M. Molten salt strategies towards carbon materials for energy storage and conversion. *Energy Storage Materials* **38**, 50–69 (2021).
- [88] Fellingner, T.-P. Sol-gel carbons from ionothermal syntheses. *Journal of Sol-Gel Science and Technology* **81**, 52–58 (2017). 18th International Sol-Gel Conference, Kyoto, JAPAN, SEP 06-11, 2015.
- [89] Haber, J. Manual on catalyst characterization (recommendations 1991). *Pure and Applied Chemistry* **63**, 1227–1246 (1991).
- [90] Wang, H., Maiyalagan, T. & Wang, X. Review on recent progress in nitrogen-doped graphene: Synthesis, characterization, and its potential applications. *ACS Catalysis* **2**,

- 781–794 (2012).
- [91] Wang, X. *et al.* Heteroatom-doped graphene materials: syntheses, properties and applications. *Chemical Society Reviews* **43**, 7067–7098 (2014).
- [92] Strelko, V. & Lavrinenko-Ometsinkaya, Y. A quantum chemical study of the effect of nitrogen heteroatoms on the chemical parameters of carbon sorbents. *Journal of Molecular Structure: THEOCHEM* **188**, 193–197 (1989).
- [93] Duan, X., O'Donnell, K., Sun, H., Wang, Y. & Wang, S. Sulfur and nitrogen co-doped graphene for metal-free catalytic oxidation reactions. *Small* **11**, 3036–3044 (2015).
- [94] Scardamaglia, M. *et al.* Tuning nitrogen species to control the charge carrier concentration in highly doped graphene. *2D Materials* **3**, 011001 (2016).
- [95] Li, M., Xu, F., Li, H. & Wang, Y. Nitrogen-doped porous carbon materials: promising catalysts or catalyst supports for heterogeneous hydrogenation and oxidation. *Catalysis Science Technology* **6**, 3670–3693 (2016).
- [96] Wu, J., Pan, Z., Zhang, Y., Wang, B. & Peng, H. The recent progress of nitrogen-doped carbon nanomaterials for electrochemical batteries. *Journal of Materials Chemistry A* **6**, 12932–12944 (2018).
- [97] Wang, X. *et al.* A metal-free polymeric photocatalyst for hydrogen production from water under visible light. *Nature Materials* **8**, 76–80 (2009).
- [98] Thomas, A. *et al.* Graphitic carbon nitride materials: variation of structure and morphology and their use as metal-free catalysts. *Journal of Materials Chemistry* **18**, 4893–4908 (2008).
- [99] Luo, W. *et al.* Pyrolysis of cellulose under ammonia leads to nitrogen-doped nanoporous carbon generated through methane formation. *Nano Letters* **14**, 2225–2229 (2014).
- [100] Yun, Y. S., Yoon, G., Kang, K. & Jin, H.-J. High-performance supercapacitors based on defect-engineered carbon nanotubes. *Carbon* **80**, 246–254 (2014).
- [101] Yu, X. *et al.* Facile synthesis of nitrogen-doped carbon nanosheets with hierarchical porosity for high performance supercapacitors and lithium–sulfur batteries. *Journal of Materials Chemistry A* **3**, 18400–18405 (2015).
- [102] Li, X. *et al.* Simultaneous nitrogen doping and reduction of graphene oxide. *Journal of the American Chemical Society* **131**, 15939–15944 (2009).
- [103] Antonietti, M. & Oschatz, M. The concept of “noble, heteroatom-doped carbons,” their directed synthesis by electronic band control of carbonization, and applications in catal-

- ysis and energy materials. *Advanced Materials* **30**, 1706836 (2018).
- [104] Kossmann, J., Heil, T., Antonietti, M. & López-Salas, N. Guanine-derived porous carbonaceous materials: Towards c1n1. *ChemSusChem* **13**, 6643–6650 (2020).
- [105] Kossmann, J. *et al.* Guanine condensates as covalent materials and the concept of cryptopores. *Carbon* **172**, 497–505 (2021).
- [106] Kossmann, J., Rothe, R., Heil, T., Antonietti, M. & López-Salas, N. Ultrahigh water sorption on highly nitrogen doped carbonaceous materials derived from uric acid. *Journal of Colloid and Interface Science* **602**, 880–888 (2021).
- [107] Christen, T. & Carlen, M. W. Theory of ragone plots. *Journal of Power Sources* **91**, 210–216 (2000).
- [108] Winter, M., Barnett, B. & Xu, K. Before li ion batteries. *Chemical Reviews* **118**, 11433–11456 (2018).
- [109] Dubal, D. P., Ayyad, O., Ruiz, V. & Gómez-Romero, P. Hybrid energy storage: the merging of battery and supercapacitor chemistries. *Chemical Society Reviews* **44**, 1777–1790 (2015).
- [110] Simon, P. & Gogotsi, Y. Materials for electrochemical capacitors. *Nature Materials* **7**, 845–854 (2008).
- [111] Simon, P. & Gogotsi, Y. Perspectives for electrochemical capacitors and related devices. *Nature Materials* **19**, 1151–1163 (2020).
- [112] Wang, G., Zhang, L. & Zhang, J. A review of electrode materials for electrochemical supercapacitors. *Chemical Society Reviews* **41**, 797–828 (2012).
- [113] Liang, J. & Wang, D.-W. Design rationale and device configuration of lithium-ion capacitors. *Advanced Energy Materials* **12**, 2200920 (2022).
- [114] Lukatskaya, M. R., Dunn, B. & Gogotsi, Y. Multidimensional materials and device architectures for future hybrid energy storage. *Nature Communications* **7** (2016).
- [115] Amatucci, G. G., Badway, F., Pasquier, A. D. & Zheng, T. An asymmetric hybrid nonaqueous energy storage cell. *Journal of The Electrochemical Society* **148**, A930 (2001).
- [116] Han, P. *et al.* Lithium ion capacitors in organic electrolyte system: Scientific problems, material development, and key technologies. *Advanced Energy Materials* **8**, 1801243 (2018).
- [117] Jagadale, A. *et al.* Lithium ion capacitors (lics): Development of the materials. *Energy Storage Materials* **19**, 314–329 (2019).

- [118] Zou, K. *et al.* Carbon materials for high-performance lithium-ion capacitor. *Current Opinion in Electrochemistry* **21**, 31–39 (2020). Energy Storage Energy Transformation.
- [119] Ilic, I. K. & Oschatz, M. The functional chameleon of materials chemistry—combining carbon structures into all-carbon hybrid nanomaterials with intrinsic porosity to overcome the “functionality-conductivity-dilemma” in electrochemical energy storage and electrocatalysis. *Small* **17**, 2007508 (2021).
- [120] Su, Y. *et al.* Compact coupled graphene and porous polyaryltriazine-derived frameworks as high performance cathodes for lithium-ion batteries. *Angewandte Chemie International Edition* **54**, 1812–1816 (2015).
- [121] Zhuang, X., Zhang, F., Wu, D. & Feng, X. Graphene coupled schiff-base porous polymers: Towards nitrogen-enriched porous carbon nanosheets with ultrahigh electrochemical capacity. *Advanced Materials* **26**, 3081–3086 (2014).
- [122] Ilic, I. K. *et al.* Sustainable cathodes for lithium-ion energy storage devices based on tannic acid—toward ecofriendly energy storage. *Advanced Sustainable Systems* **5**, 2000206 (2021).
- [123] Laidler, K. J. A glossary of terms used in chemical kinetics, including reaction dynamics (iupac recommendations 1996). *Pure and Applied Chemistry* **68**, 149–192 (1996).
- [124] Hagen, J. *Industrial catalysis: a practical approach* (John Wiley & Sons, 2015).
- [125] Benkovic, S. J. & Hammes-Schiffer, S. A perspective on enzyme catalysis. *Science* **301**, 1196–1202 (2003).
- [126] Antonietti, M., Lopez-Salas, N. & Primo, A. Adjusting the structure and electronic properties of carbons for metal-free carbocatalysis of organic transformations. *Advanced Materials* **31**, 1805719 (2019).
- [127] Stenhouse, J. Ueber entfärbende kohle und ihr vermögen, einige gase zu absorbiren. *Justus Liebigs Annalen der Chemie* **101**, 243–252 (1857).
- [128] Liu, X. & Dai, L. Carbon-based metal-free catalysts. *Nature Reviews Materials* **1** (2016).
- [129] Gong, K., Du, F., Xia, Z., Durstock, M. & Dai, L. Nitrogen-doped carbon nanotube arrays with high electrocatalytic activity for oxygen reduction. *Science* **323**, 760–764 (2009).
- [130] Qu, L., Liu, Y., Baek, J.-B. & Dai, L. Nitrogen-doped graphene as efficient metal-free electrocatalyst for oxygen reduction in fuel cells. *ACS nano* **4**, 1321–1326 (2010).
- [131] Zhao, Y., Nakamura, R., Kamiya, K., Nakanishi, S. & Hashimoto, K. Nitrogen-doped

- carbon nanomaterials as non-metal electrocatalysts for water oxidation. *Nature Communications* **4**, 1–7 (2013).
- [132] Kumar, B. *et al.* Renewable and metal-free carbon nanofibre catalysts for carbon dioxide reduction. *Nature Communications* **4**, 1–8 (2013).
- [133] Zheng, Y. *et al.* Hydrogen evolution by a metal-free electrocatalyst. *Nature Communications* **5**, 1–8 (2014).
- [134] Yan, X., Jia, Y. & Yao, X. Defects on carbons for electrocatalytic oxygen reduction. *Chemical Society Reviews* **47**, 7628–7658 (2018).
- [135] Hu, C. & Dai, L. Doping of carbon materials for metal-free electrocatalysis. *Advanced Materials* **31**, 1804672 (2019).
- [136] Guo, D. *et al.* Active sites of nitrogen-doped carbon materials for oxygen reduction reaction clarified using model catalysts. *Science* **351**, 361–365 (2016).
- [137] Rideal, E. K. & Wright, W. M. Clxxxiv.—low temperature oxidation at charcoal surfaces. part i. the behaviour of charcoal in the absence of promoters. *Journal of the Chemical Society, Transactions* **127**, 1347–1357 (1925).
- [138] Kutzelnigg, A. Zur kenntnis der sauerstoff-übertragenden wirkung von stoffen mit großer spezifischer oberfläche. *Berichte der deutschen chemischen Gesellschaft (A and B Series)* **63**, 1753–1758 (1930).
- [139] Byung, H. H., Dae, H. S. & Sung, Y. C. Graphite catalyzed reduction of aromatic and aliphatic nitro compounds with hydrazine hydrate. *Tetrahedron letters* **26**, 6233–6234 (1985).
- [140] Larsen, J. W., Freund, M., Kim, K. Y., Sidovar, M. & Stuart, J. L. Mechanism of the carbon catalyzed reduction of nitrobenzene by hydrazine. *Carbon* **38**, 655–661 (2000).
- [141] Su, D. S., Wen, G., Wu, S., Peng, F. & Schlögl, R. Carbocatalysis in liquid-phase reactions. *Angewandte Chemie International Edition* **56**, 936–964 (2017).
- [142] Navalon, S., Dhakshinamoorthy, A., Alvaro, M. & Garcia, H. Carbocatalysis by graphene-based materials. *Chemical Reviews* **114**, 6179–6212 (2014).
- [143] Su, C. & Loh, K. P. Carbocatalysts: Graphene oxide and its derivatives. *Accounts of Chemical Research* **46**, 2275–2285 (2013).
- [144] Dreyer, D. R. & Bielawski, C. W. Carbocatalysis: Heterogeneous carbons finding utility in synthetic chemistry. *Chemical Science* **2**, 1233–1240 (2011).
- [145] Dreyer, D. R., Jia, H.-P. & Bielawski, C. W. Graphene oxide: a convenient carbocatalyst

- for facilitating oxidation and hydration reactions. *Angewandte Chemie* **122**, 6965–6968 (2010).
- [146] Luo, J., Peng, F., Yu, H., Wang, H. & Zheng, W. Aerobic liquid-phase oxidation of ethylbenzene to acetophenone catalyzed by carbon nanotubes. *ChemCatChem* **5**, 1578–1586 (2013).
- [147] Yang, J.-H. *et al.* Direct catalytic oxidation of benzene to phenol over metal-free graphene-based catalyst. *Energy & Environmental Science* **6**, 793–798 (2013).
- [148] Gao, Y., Ma, D., Wang, C., Guan, J. & Bao, X. Reduced graphene oxide as a catalyst for hydrogenation of nitrobenzene at room temperature. *Chemical Communications* **47**, 2432–2434 (2011).
- [149] Huang, H. *et al.* Graphite oxide as an efficient and durable metal-free catalyst for aerobic oxidative coupling of amines to imines. *Green Chemistry* **14**, 930–934 (2012).
- [150] Jia, H.-P., Dreyer, D. R. & Bielawski, C. W. Graphite oxide as an auto-tandem oxidation–hydration–aldol coupling catalyst. *Advanced Synthesis & Catalysis* **353**, 528–532 (2011).
- [151] Gao, Y. *et al.* Graphene oxide catalyzed c–h bond activation: The importance of oxygen functional groups for biaryl construction. *Angewandte Chemie International Edition* **55**, 3124–3128 (2016).
- [152] Stellwagen, D. R., van der Klis, F., van Es, D. S., de Jong, K. P. & Bitter, J. H. Functionalized carbon nanofibers as solid-acid catalysts for transesterification. *ChemSusChem* **6**, 1668–1672 (2013).
- [153] Zhao, X. *et al.* Graphene oxide for cellulose hydrolysis: how it works as a highly active catalyst? *Chemical communications* **50**, 3439–3442 (2014).
- [154] van Dommele, S., de Jong, K. P. & Bitter, J. H. Nitrogen-containing carbon nanotubes as solid base catalysts. *Chemical communications* 4859–4861 (2006).
- [155] Kong, X.-K., Chen, C.-L. & Chen, Q.-W. Doped graphene for metal-free catalysis. *Chemical Society Reviews* **43**, 2841–2857 (2014).
- [156] Duan, X., Sun, H. & Wang, S. Metal-free carbocatalysis in advanced oxidation reactions. *Accounts of Chemical Research* **51**, 678–687 (2018).
- [157] Hu, Y. *et al.* Nitrogen-doped carbon nanomaterials as highly active and specific peroxidase mimics. *Chemistry of Materials* **30**, 6431–6439 (2018).
- [158] Gao, Y. *et al.* Nitrogen-doped sp²-hybridized carbon as a superior catalyst for selective oxidation. *Angewandte Chemie International Edition* **52**, 2109–2113 (2013).

- [159] Kan-nari, N., Okamura, S., Fujita, S.-i., Ozaki, J.-i. & Arai, M. Nitrogen-doped carbon materials prepared by ammoxidation as solid base catalysts for knoevenagel condensation and transesterification reactions. *Advanced Synthesis & Catalysis* **352**, 1476–1484 (2010).
- [160] Li, B., Sun, X. & Su, D. Calibration of the basic strength of the nitrogen groups on the nanostructured carbon materials. *Physical Chemistry Chemical Physics* **17**, 6691–6694 (2015).
- [161] Wen, G. *et al.* Acid properties of nanocarbons and their application in oxidative dehydrogenation. *ACS Catalysis* **5**, 3600–3608 (2015).
- [162] Liu, F. *et al.* Sulfated graphene as an efficient solid catalyst for acid-catalyzed liquid reactions. *Journal of Materials Chemistry* **22**, 5495–5502 (2012).
- [163] Anderson, J. M., Johnson, R. L., Schmidt-Rohr, K. & Shanks, B. H. Solid state nmr study of chemical structure and hydrothermal deactivation of moderate-temperature carbon materials with acidic so₃h sites. *Carbon* **74**, 333–345 (2014).
- [164] Rao, R. *et al.* Carbon nanotubes and related nanomaterials: Critical advances and challenges for synthesis toward mainstream commercial applications. *ACS Nano* **12**, 11756–11784 (2018).
- [165] Rimmel, A. Why chemists can't quit palladium. *Nature* **606**, 448–451 (2022).
- [166] Wang, L., Sofer, Z. & Pumera, M. Will any crap we put into graphene increase its electrocatalytic effect? *ACS nano* **14**, 21–25 (2020).
- [167] Yang, X.-F. *et al.* Single-atom catalysts: a new frontier in heterogeneous catalysis. *Accounts of Chemical Research* **46**, 1740–1748 (2013).
- [168] Stoyanov, S. R., Titov, A. V. & Král, P. Transition metal and nitrogen doped carbon nanostructures. *Coordination Chemistry Reviews* **253**, 2852–2871 (2009). Functional Hybrid Nanomaterials:.
- [169] Lefevre, M. & Dodelet, J.-P. Fe-based catalysts for the reduction of oxygen in polymer electrolyte membrane fuel cell conditions: determination of the amount of peroxide released during electroreduction and its influence on the stability of the catalysts. *Electrochimica Acta* **48**, 2749–2760 (2003).
- [170] Cavalier, J., Chornet, E., Beauregard, B. & Coquard, G. Preparation of metal-impregnated peat carbons and characterization of the platinum dispersion. *Carbon* **16**, 21–26 (1978).
- [171] Qiao, B. *et al.* Single-atom catalysis of co oxidation using Pt₁/FeO_x. *Nature Chemistry* **3**, 634–641 (2011).

- [172] Liu, J. Catalysis by supported single metal atoms. *ACS Catalysis* **7**, 34–59 (2017).
- [173] Wang, A., Li, J. & Zhang, T. Heterogeneous single-atom catalysis. *Nature Reviews Chemistry* **2**, 65–81 (2018).
- [174] Kaiser, S. K., Chen, Z., Faust Akl, D., Mitchell, S. & Pérez-Ramírez, J. Single-atom catalysts across the periodic table. *Chemical Reviews* **120**, 11703–11809 (2020).
- [175] Liu, P. *et al.* Photochemical route for synthesizing atomically dispersed palladium catalysts. *Science* **352**, 797–800 (2016).
- [176] Wu, J., Xiong, L., Zhao, B., Liu, M. & Huang, L. Densely populated single atom catalysts. *Small Methods* **4**, 1900540 (2020).
- [177] Gawande, M. B., Fornasiero, P. & Zbořil, R. Carbon-based single-atom catalysts for advanced applications. *ACS Catalysis* **10**, 2231–2259 (2020).
- [178] Zhao, L. *et al.* Cascade anchoring strategy for general mass production of high-loading single-atomic metal-nitrogen catalysts. *Nature Communications* **10**, 1–11 (2019).
- [179] Zuo, Q. *et al.* Ultrathin metal–organic framework nanosheets with ultrahigh loading of single pt atoms for efficient visible-light-driven photocatalytic h₂ evolution. *Angewandte Chemie International Edition* **58**, 10198–10203 (2019).
- [180] Cheng, Y. *et al.* Atomically dispersed transition metals on carbon nanotubes with ultrahigh loading for selective electrochemical carbon dioxide reduction. *Advanced Materials* **30**, 1706287 (2018).
- [181] Liu, W. *et al.* Discriminating catalytically active fe_nc species of atomically dispersed fe–n–c catalyst for selective oxidation of the c–h bond. *Journal of the American Chemical Society* **139**, 10790–10798 (2017).
- [182] Wang, J., Li, Z., Wu, Y. & Li, Y. Fabrication of single-atom catalysts with precise structure and high metal loading. *Advanced Materials* **30**, 1801649 (2018).
- [183] Wang, L. *et al.* A sulfur-tethering synthesis strategy toward high-loading atomically dispersed noble metal catalysts. *Science Advances* **5**, eaax6322 (2019).
- [184] Su, H. *et al.* Grouping effect of single nickel- n₄ sites in nitrogen-doped carbon boosts hydrogen transfer coupling of alcohols and amines. *Angewandte Chemie International Edition* **130**, 15414–15418 (2018).
- [185] Xu, W.-F., Chen, W.-J., Li, D.-C., Cheng, B.-H. & Jiang, H. Highly dispersed manganese based mn/n–c/al₂o₃ catalyst for selective oxidation of the c–h bond of ethylbenzene. *Industrial & Engineering Chemistry Research* **58**, 3969–3977 (2019).

- [186] Chen, Z. *et al.* A heterogeneous single-atom palladium catalyst surpassing homogeneous systems for suzuki coupling. *Nature Nanotechnology* **13**, 702+ (2018).
- [187] Zhang, Q. & Guan, J. Single-atom catalysts for electrocatalytic applications. *Advanced Functional Materials* **30**, 2000768 (2020).
- [188] Che, M. Nobel prize in chemistry 1912 to sabatier: Organic chemistry or catalysis? *Catalysis Today* **218**, 162–171 (2013).
- [189] Ananikov, V. P. Nickel: the “spirited horse” of transition metal catalysis (2015).
- [190] Yang, Y., Ren, Y., Sun, C. & Hao, S. Facile route fabrication of nickel based mesoporous carbons with high catalytic performance towards 4-nitrophenol reduction. *Green Chemistry* **16**, 2273–2280 (2014).
- [191] Park, E. J. *et al.* Toluene oxidation catalyzed by nio/sio2 and nio/tio2/sio2: Towards development of humidity-resistant catalysts. *Catalysis Today* **260**, 100–106 (2016).
- [192] Qiu, H.-J. *et al.* Nanoporous graphene with single-atom nickel dopants: an efficient and stable catalyst for electrochemical hydrogen production. *Angewandte Chemie International Edition* **54**, 14031–14035 (2015).
- [193] Ohn, S. *et al.* Molecularly dispersed nickel-containing species on the carbon nitride network as electrocatalysts for the oxygen evolution reaction. *Carbon* **124**, 180–187 (2017).
- [194] Yang, H. B. *et al.* Atomically dispersed ni (i) as the active site for electrochemical co2 reduction. *Nature Energy* **3**, 140–147 (2018).
- [195] Xu, Y. *et al.* Single-ni-atom catalyzes aqueous phase electrochemical reductive dechlorination reaction. *Applied Catalysis B: Environmental* **277**, 119057 (2020).
- [196] Li, M. *et al.* Single-atom tailoring of platinum nanocatalysts for high-performance multifunctional electrocatalysis. *Nature Catalysis* **2**, 495–503 (2019).
- [197] Zhang, L. *et al.* Single nickel atoms on nitrogen-doped graphene enabling enhanced kinetics of lithium–sulfur batteries. *Advanced Materials* **31**, 1903955 (2019).
- [198] Zhong, W. *et al.* A covalent organic framework bearing single ni sites as a synergistic photocatalyst for selective photoreduction of co2 to co. *Journal of the American Chemical Society* **141**, 7615–7621 (2019).
- [199] Millet, M.-M. *et al.* Ni single atom catalysts for co2 activation. *Journal of the American Chemical Society* **141**, 2451–2461 (2019).
- [200] Akri, M. *et al.* Atomically dispersed nickel as coke-resistant active sites for methane dry

- reforming. *Nature Communications* **10**, 1–10 (2019).
- [201] Riley, C. *et al.* Design of effective catalysts for selective alkyne hydrogenation by doping of ceria with a single-atom promotor. *Journal of the American Chemical Society* **140**, 12964–12973 (2018).
- [202] Liu, W. *et al.* A durable nickel single-atom catalyst for hydrogenation reactions and cellulose valorization under harsh conditions. *Angewandte Chemie International Edition* **130**, 7189–7193 (2018).
- [203] Zhao, S. *et al.* One-pot pyrolysis method to fabricate carbon nanotube supported ni single-atom catalysts with ultrahigh loading. *ACS Applied Energy Materials* **1**, 5286–5297 (2018).
- [204] Lu, P. *et al.* Facile synthesis of single-nickel-atomic dispersed n-doped carbon framework for efficient electrochemical co₂ reduction. *Applied Catalysis B: Environmental* **241**, 113–119 (2019).
- [205] Gong, Y.-N. *et al.* Regulating the coordination environment of mof-templated single-atom nickel electrocatalysts for boosting co₂ reduction. *Angewandte Chemie International Edition* **59**, 2705–2709 (2020).
- [206] Rong, X., Wang, H.-J., Lu, X.-L., Si, R. & Lu, T.-B. Controlled synthesis of a vacancy-defect single-atom catalyst for boosting co₂ electroreduction. *Angewandte Chemie International Edition* **59**, 1961–1965 (2020).
- [207] Song, X. *et al.* Graphene-supported single nickel atom catalyst for highly selective and efficient hydrogen peroxide production. *ACS Applied Materials & Interfaces* **12**, 17519–17527 (2020).
- [208] Wang, Y. *et al.* High-efficiency oxygen reduction to hydrogen peroxide catalyzed by nickel single-atom catalysts with tetradentate n₂o₂ coordination in a three-phase flow cell. *Angewandte Chemie International Edition* **59**, 13057–13062 (2020).
- [209] Cai, Z. *et al.* Single-atom-sized ni–n₄ sites anchored in three-dimensional hierarchical carbon nanostructures for the oxygen reduction reaction. *Journal of Materials Chemistry A* **8**, 15012–15022 (2020).
- [210] Pander III, J. E. *et al.* Understanding the heterogeneous electrocatalytic reduction of carbon dioxide on oxide-derived catalysts. *ChemElectroChem* **5**, 219–237 (2018).

Chapter 2

Salt melt templated synthesis

2.1 Synthetic procedure

The salt melt templated synthesis is a versatile and convenient method to synthesize porous materials.[1] Ideally, a salt acts simultaneously as solvent and porogen in a sol-gel-like mechanism during the heating process.[2] Once the system is cooled down to room temperature, the salt can be washed out with an acidic solution while the porous material remains insoluble and can be separated by filtration (**Figure 2.1**). Material final porosity is a function of precursor, salt, the ratio between precursor and salt, working temperature, heating ratio, and atmosphere inside of the oven.

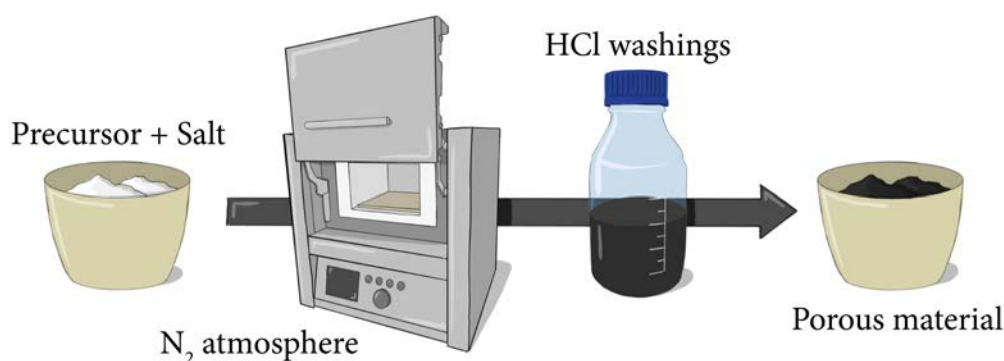


Figure 2.1: Graphical representation of the salt melt templated synthesis.

As introduced in **Chapter 1**, different salts can be used as melts to develop porous materials.[3] Among all, zinc-based salt melts are the most popular and many papers have been published after the first work from Fellingner et al.[4] In this series of studies, different variables were investigated such as polarity, viscosity, and molar ratios of the melt. The conclusion from these remarkable works was that porosity is generated by a sol-gel mechanism and negligible chemical effect was appreciable.[3] Yet, most of the studies were conducted at high temperatures and without comparing different precursors. However, these parameters are key points in the synthesis and need further exploration.

For these reasons, in order to obtain a better picture of the process, different precursors, salt mixtures and temperatures will be taken into account and compared in this chapter. The materials will be named hereafter as "**PTSM**", where P will be an alphanumeric character to indicate the precursor (i.e., A for adenine, C for cytosine, and CF for caffeine), T indicates the temperature of the heating procedure (i.e., 8 for 800 °C, 7 for 700 °C, 6 for 600 °C, 5 for 500 °C), and SM stands for the salt melt used (i.e., LZ for LiCl/ZnCl₂, NZ for NaCl/ZnCl₂, and LK for LiCl/KCl). To observe the effect of these variables all the remaining parameters were kept constant unless specified. The heating process was run in nitrogen atmosphere at a constant heating ratio (i.e., 1 °C/min). The salt-precursor ratio was kept equal to 20 g to 1 g. Sample were washed twice at room temperature and once at 50 °C.

2.2 Precursor dependence

Nucleobases, also known as nitrogenous bases, are heterocyclic compounds formed by carbon and nitrogen atoms. They are classified as pyrimidine or purine bases depending on the mono- or bi-cyclic nature, respectively.[5] They present different functionalities such as amines or carbonyls, which can act as proton bond donors or acceptors. Moreover, they were pointed as promising noble carbon precursors by Antonietti et al. due to their high oxidation potential.[6] Finally, the low carbon to nitrogen ratio (i.e., high nitrogen content) makes them suitable candidates to promote the formation of highly nitrogen-doped carbonaceous structures even at high temperatures. For these reasons, two different nucleobases (i.e., cytosine and adenine, **Figure 2.2**) and a chemically related purine (i.e., caffeine, **Figure 2.2**) were chosen to understand the precursor role during the salt melt templated synthesis (**Table 2.1**).

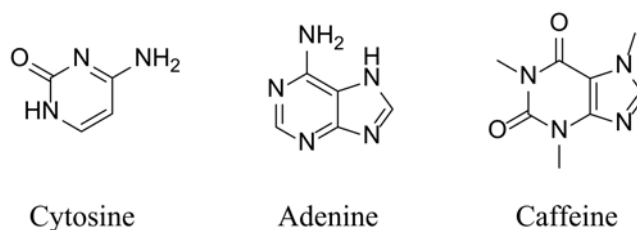


Figure 2.2: (From left to right) Molecular structure of cytosine, adenine and caffeine.

The thermal decomposition of these nucleobases was studied through thermogravimetric analysis (TGA) in nitrogen atmosphere (**Figure 2.3**). Cytosine showed the highest thermal stability among all the precursors, having 30 wt% of the initial mass left at 800 °C. On the other hand, adenine and caffeine showed both the complete loss of mass around 350 °C. This was associated with the sublimation or evaporation (consequential to the melting) of the initial precursor.[7, 8] Interestingly, adenine and caffeine resulted in giving a product at 800 °C (**Table 2.1**) despite their thermal stability, suggesting the critical role of the salt melt (LiCl/ZnCl₂) during the material synthesis.

To test the thermal properties of the materials, TGA in nitrogen and synthetic air atmosphere was used (**Figure 2.3**). The thermal profiles of the materials do not show a remarkable decomposition in nitrogen atmosphere until 600 °C, and more than 80% of the mass is conserved up to

Table 2.1: Summary of the material synthesized, codes and yields.

Precursor	Salt	T _{synthesis} °C	Code	Yield ^a wt%
Cytosine	LiCl/ZnCl ₂	800	C8LZ	28
Adenine			A8LZ	30
Caffeine			CF8LZ	25

^a The yield was calculated as a fraction between the final material mass and the initial precursor mass.

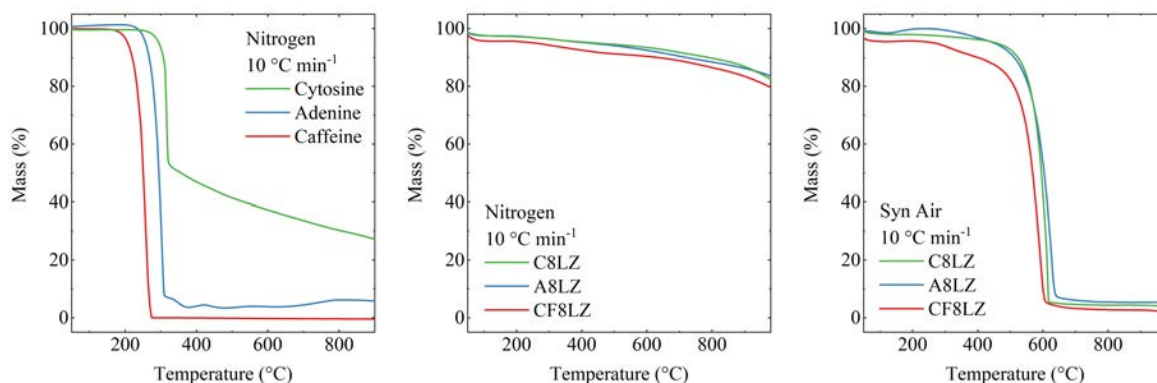


Figure 2.3: Thermogravimetric analysis at 10 K min^{-1} of (from left to right) precursor in nitrogen, materials in nitrogen, materials in synthetic air.

$1000 \text{ }^{\circ}\text{C}$. All the TGA profiles recorded in synthetic air are characterized by a complete material decomposition at $600 \text{ }^{\circ}\text{C}$. CF8LZ profile in synthetic air indicates that a partial decomposition of the material starts after $300 \text{ }^{\circ}\text{C}$, suggesting that the caffeine-derived material is less stable in air compared to C8LZ and A8LZ.

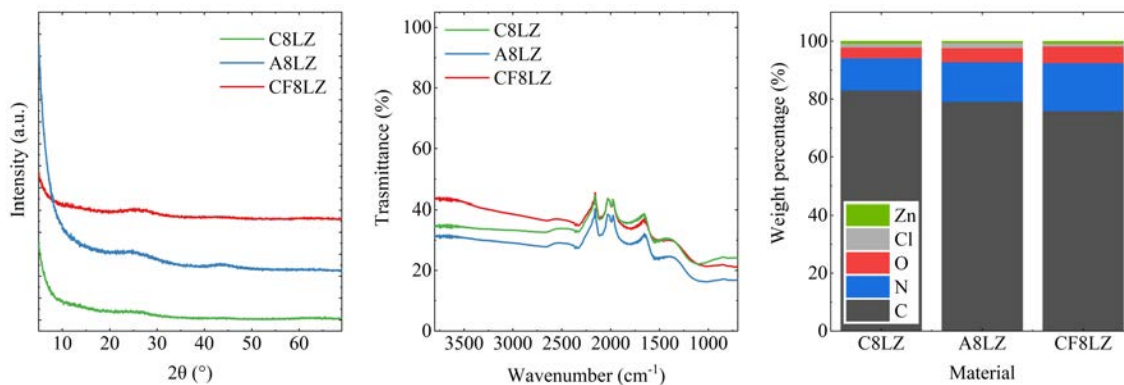
Structural properties were analyzed through X-ray diffraction (XRD), Fourier-transform infrared spectroscopy (FTIR), and Energy Dispersive X-ray Analysis (SEM-EDX) and reported in **Figure 2.4**. Remarkably, XRD patterns do not show any diffraction peak coming from the salt used as a porogen indicating the successful washing procedure with hydrochloric acid. Moreover, XRD patterns are characterized by high-intensity signals at low angles and a broad band with low intensity at 26.5° indicating the presence of micropores and poor graphitic stacking, respectively.[10, 11] Purine derived materials (i.e., A8LZ and CF8LZ) presents a slight increase in the intensity from the 26.5° band, which may indicate a better stacking of layers when purine bases are used in the synthesis.[11]

In order to observe the presence of characteristic vibrations, FTIR spectroscopy was applied on the three different materials. However, no specific difference in the spectra was appreciated (**Figure 2.4**). Indeed, all spectra show a low percentage of IR transmittance (i.e., 30-45%) and the absence of defined vibration peaks. Both observations suggest that the materials are characterized by highly condensed structures. This suggests that the initial precursor functions are either included in the structure or lost upon heat treatment.[12]

SEM-EDX was used to elucidate material compositions (**Table 2.2** and **Figure 2.4**). This analysis revealed that all materials are composed mainly of carbon atoms (i.e., 75.9 wt% for CF8LZ, 79.1 wt% for A8LZ, 82.9 wt% for C8LZ). Yet, the nitrogen content is very high (i.e., 11.1 wt% for C8LZ, 13.7 wt% for A8LZ, and 16.6 wt% for CF8LZ), confirming that the use of heterocycles as starting molecules to develop highly heteroatom doped materials is a more convenient strategy compared to the post-treatment procedure, which can include lower heteroatom percentages (up to 10 wt%).[13, 14] Moreover, materials derived from purine bases

Table 2.2: Composition summary of materials obtained from different precursors.

Material	SEM-EDX					ICP-EOS
	wt%					wt%
	C	N	O	Cl	Zn	Zn
C8LZ	82.9	11.1	3.7	1.3	0.8	0.97
A8LZ	79.1	13.7	4.8	1.8	0.5	0.75
CF8LZ	75.9	16.6	5.7	0.9	0.8	1.67

**Figure 2.4:** (from left to right) X-ray diffraction patterns, FT-IR transmittance spectra, and elemental composition from SEM-EDX of C8LZ (green), A8LZ (blue) and CF8LZ (red).

(i.e., CF8LZ and A8LZ) presents higher nitrogen doping than pyrimidine bases derived materials (i.e., C8LZ). Moreover, molecular structure with oxygen atoms might preserve oxygen atoms in the structure, too (i.e., 3.7 wt% for C8LZ and 5.7 wt% for CF8LZ from SEM-EDX). However, despite adenine does not contain any oxygen atom in its molecular structure, the final material A8NZ presents a small oxygen content as well (i.e., 4.8). This suggests that the oxygen content measured might be adventitious from water molecules strongly adsorbed on the materials surface. Noteworthy, Kossmann et al. reported that uric acid derived material are characterized by high water adsorption.[9] Hence, materials from nucleobase and nucleobase-like molecules might be characterized by high water uptake which hinders the determination of structural oxygen. Finally, a small percentage of chlorine (SEM-EDX) and zinc were observed (SEM-EDX and ICP-EOS). This indicates that even though the washing procedure successfully removed bulk salt, yet, small leftovers remain in the materials.

Scanning electron microscopy (SEM) shows that C8LZ and A8LZ are formed by condensed colloidal structures suggesting a sol-gel-like mechanism and a spinodal decomposition during the heating process (**Figure 2.5**).[2] Ideally, colloidal morphology can be obtained by a four steps process involving:

1. **solvation** of the precursor or oligomers;
2. **condensation** of the precursor into oligomers
3. **growing** of the oligomers;
4. **precipitation** of the bigger oligomers (not soluble in the melt);

The final morphology of the material will be influenced by the competition between these steps, which is itself influenced by the characteristic kinetic. More in detail, SEM imaging reveals that A8LZ presents smaller colloids compared to C8LZ indicating that precipitation occurs faster than condensation when adenine is used as the precursor. This might be induced by: (a) oligomers from adenine are less soluble than the ones from cytosine or (b) cytosine derived dissolved species are more reactive than adenine ones. However, the discrimination between these two possibilities is not trivial and needs further investigation. Remarkably, CF8LZ shows different morphology characterized by big flakes (length $>1\mu\text{m}$) and balls (c.a. diameter = 200nm). This is ascribed to a bad solvation (process 1) for caffeine-derived intermediate species, which promotes the formation of different morphology than colloids. This matches the importance of precursor solubility during the synthesis as reported in literature.[4] The choice of the precursor must be done taking into account a molecule that condensates slowly and at higher temperatures in order to let melt the salt and promote step 1.

Scanning transmission electron microscopy (STEM) confirms the previous observation from SEM analysis. A8LZ and C8LZ present a colloidal structure and the higher degree of disorder

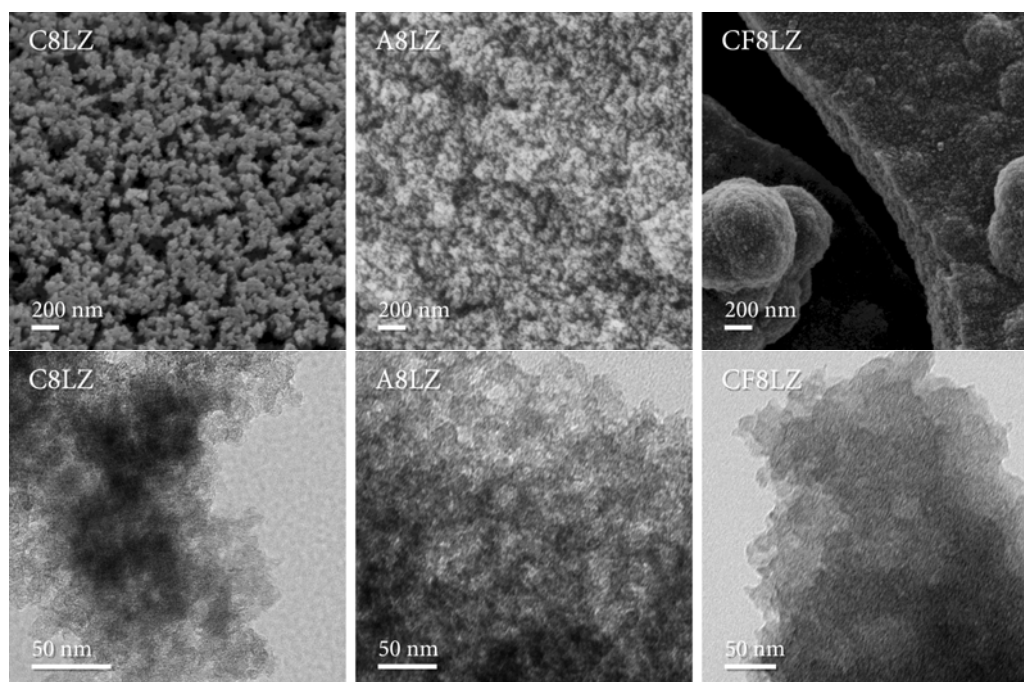


Figure 2.5: Scanning electron microscopy (first row) and Scanning transmission electron microscopy (second row) of (from left to right) C8LZ, A8LZ, and CF8LZ.

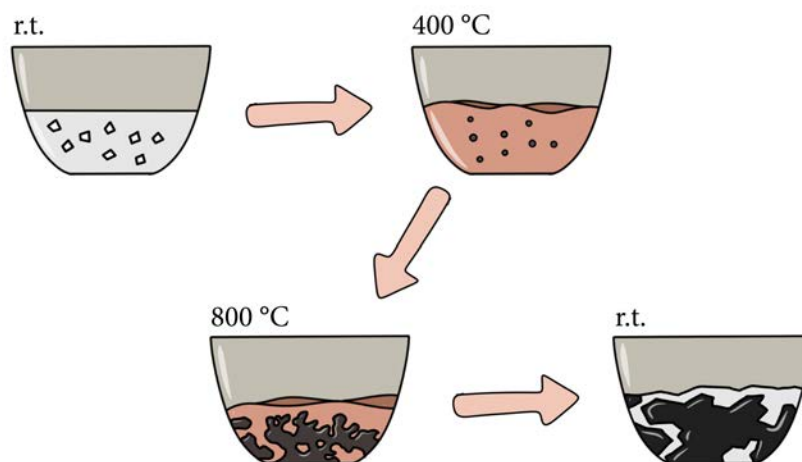


Figure 2.6: Graphical representation of the sol-gel-like mechanism proposed.

observed for A8LZ matches the lower dimension of the colloids while CF8LZ STEM picture shows a compact structure. The differences in the STEM images correlate to different solvation/precipitation processes, which influences the structure in the nanoscale. Remarkably, the more condensed structure observed for CF8LZ suggests lower mesopores volume compared to C8LZ and A8NZ.

Finally, gas adsorption was used to characterize the pore structure of the materials prepared (**Figure 2.7**). Nitrogen isotherms at 77K display a clear difference among the three materials highlighting the precursor role in the development of the pore structure. Accordingly to IUPAC guidelines, C8LZ isotherm is a type I and II, A8LZ isotherm is a type IV, and CF8LZ isotherm is a type I.[15] The different shapes of nitrogen isotherms indicate that C8LZ is a material characterized by micro-, meso-, and macropores, while A8LZ presents micro- and mesopores and CF8LZ only micropores. The analysis of DFT derived pore size distribution of the samples revealed the presence of an asymmetric distribution of pores with a maximum at 5 nm for C8LZ and A8LZ, while CF8LZ presents a small population of small meso-pores at 2 nm. Total pore volume measured from nitrogen isotherms (**Table 2.3**) reveals higher gas uptake for C8LZ and A8NZ ($2.1 \text{ cm}^3 \text{ g}^{-1}$ and $2.5 \text{ cm}^3 \text{ g}^{-1}$) compared to CF8NZ ($0.3 \text{ cm}^3 \text{ g}^{-1}$) and it agrees with STEM imaging. Finally, the BET equation was applied on the nitrogen adsorption branch to calculate the specific surface areas of the materials prepared. The analysis results with $1834 \text{ m}^2 \text{ g}^{-1}$, $2334 \text{ m}^2 \text{ g}^{-1}$, and $556 \text{ m}^2 \text{ g}^{-1}$ for C8LZ, A8LZ, and CF8LZ, respectively (**Table 2.3**).

CO_2 adsorption isotherms at 273K were used to further characterize the microporous structure of the prepared materials (**Figure 2.7**). The total pore volumes derived from CO_2 follow a similar trend compared to the one followed by specific surface areas (**Table 2.3**) with A8LZ having the highest volume (i.e., $0.21 \text{ cm}^3 \text{ g}^{-1}$), followed by C8LZ ($0.18 \text{ cm}^3 \text{ g}^{-1}$) and CF8LZ ($0.06 \text{ cm}^3 \text{ g}^{-1}$). C8LZ isotherm shows higher CO_2 adsorbed than A8LZ at low pressures (i.e., 100 Torr). This difference is related to the nature of carbon dioxide, which is less chemical inert than molecular nitrogen and it can interact with basic sites. Hence, surface properties

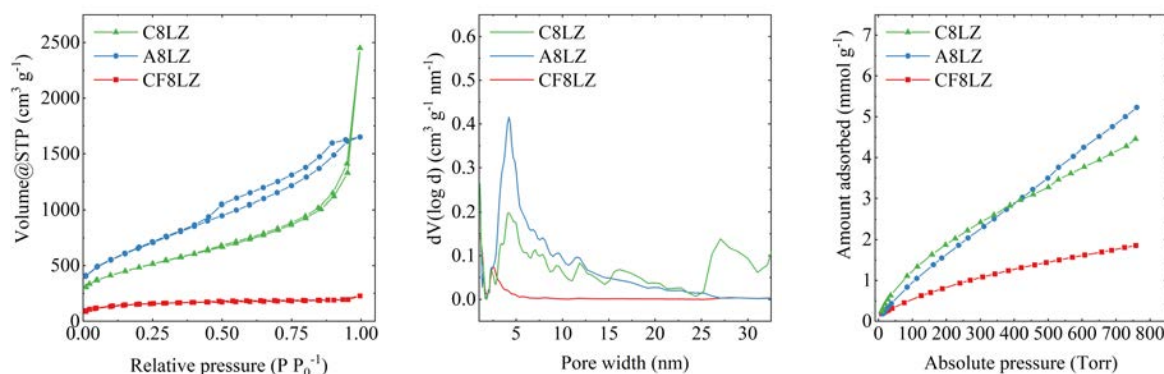


Figure 2.7: (From left to right) N₂ isotherms at 77K, DFT calculated pore size distribution, and CO₂ adsorption isotherm at 273K for C8LZ (green), A8LZ (blue), and CF8LZ (red).

Table 2.3: Gas adsorption data obtained from BET and DFT calculations applied on N₂ and CO₂ isotherms at 77K and 273K.

Material	Specific surface area ^a	Total pore volume (<40 nm) ^a	Total pore volume (<10 nm) ^b
	m ² g ⁻¹	cm ³ g ⁻¹	cm ³ g ⁻¹
C8LZ	1701	2.1	0.18
A8LZ	2335	2.5	0.21
CF8LZ	556	0.3	0.06

^a Calculated from nitrogen isotherm at 77 K.

^b Calculated from carbon dioxide isotherm at 273 K.

might influence dramatically the adsorption at lower pressures. Thus, the data suggest that C8LZ shows a higher affinity for CO₂ than A8LZ.

In conclusion, the material obtained from different nitrogenous bases at 800°C in presence of LiCl/ZnCl₂ differs mainly for the morphology which was shown as function of the starting precursor. On the other hand, chemical structures appear similar in term of composition and FT-IR. This might be induced by the high working temperature (i.e., 800 °C) which promotes similar material phases. Yet, the role of the salt melt needs to be elucidated in order to explain how precursors with low thermal stability (i.e., adenine and caffeine) shows the formation of materials at 800°C.

2.3 Salt melt dependence

The melting temperature of the salt is considered one of the most crucial parameters during the salt melt templated method. Indeed, Fechner et al. in 2013 reported it as the target to choose a salt.[1] This temperature must be lower than the decomposition temperature of the materials precursor. For example, LiCl/ZnCl₂ melting temperature (i.e., 330 °C, see **Table 2.1**) is lower than the decomposition temperature of cytosine (i.e., 350 °C); this allows a better solvation process and the formation of colloidal-like structures in the final material. However, the role of the salt as not-innocent chemical agent is often overlooked in most of the papers and needs

further discussion. For these reasons, NaCl/ZnCl₂ (NZ), LiCl/ZnCl₂ (LZ), and LiCl/KCl (LK) were chosen as salt melts to study the role of the metallic species in the development of porous materials from cytosine at 800 °C (**Table 2.1**).

Table 2.1: Summary of material synthesized from different salt, melting temperature of these salts, code given to the materials and relative yields.

Precursor	Salt	T _{melting} °C	T _{synthesis} °C	Code	Yield ^a wt%
Cytosine	NaCl/ZnCl ₂	325	800	C8NZ	30
	LiCl/ZnCl ₂	330		C8LZ	30
	LiCl/KCl	352		C8LK	30

^a The yield was calculated as a fraction between the final material mass and the initial precursor mass.

At first, the thermal properties of the carbonaceous materials were characterized by TGA analysis in synthetic air and nitrogen atmosphere (**Figure 2.8**). While C8NZ and C8LZ have similar stability in nitrogen, the C8LK profile displays a faster decomposition above 800 °C, suggesting differences in structural properties for this material. On the other hand, thermal decomposition profiles obtained in synthetic air show almost complete mass loss above 600 °C among all the materials.

As suggested by TGA in nitrogen and synthetic air, structural properties observed from XRD, FT-IR, and SEM-EDX are significantly different for C8LK compared to C8NZ or C8LZ (**Figure 2.9**). At first, the X-ray diffraction pattern from C8LK displays a broad band at 26.5 °. Moreover, the low intensity of the signal at low angles suggests the absence of micropores in this material.[10] On the other hand, C8NZ XRD pattern is extremely similar to C8LZ suggesting the presence of micropores in the material.

FT-IR spectra recorded from the three materials showed a low transmittance percentage indicating a high condensation level of the materials (**Figure 2.9**).[12]. In addition to this, no

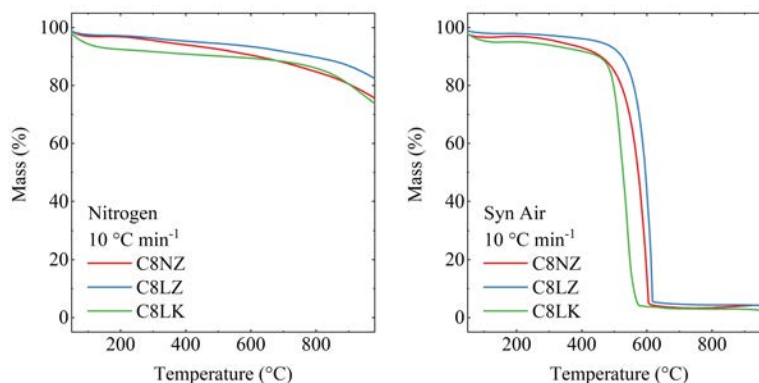
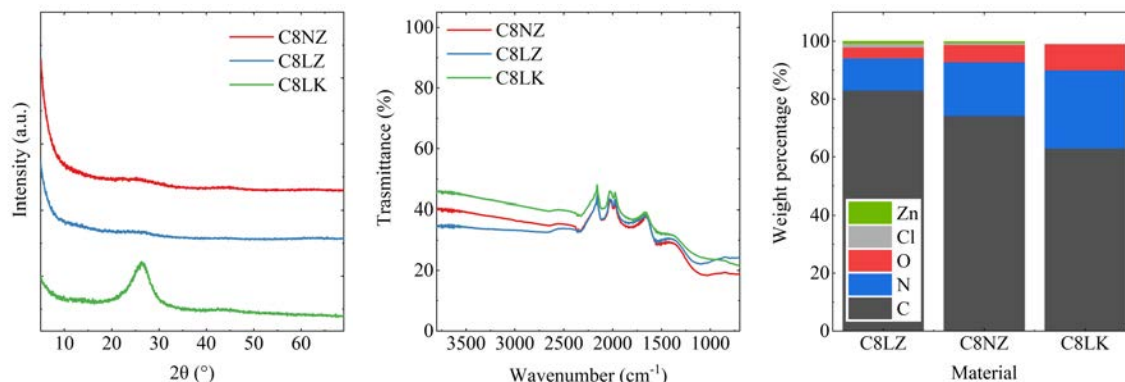


Figure 2.8: Thermogravimetric analysis at 10 K min⁻¹ of (from left to right) materials in nitrogen and materials in synthetic air.

Table 2.2: Composition summary of materials obtained from different precursors.

Material	SEM-EDX					ICP-EOS
	wt%					wt%
	C	N	O	Cl	Zn	Zn
C8NZ	74.2	18.6	5.9	0.7	0.5	1.7
C8LZ	82.9	11.1	3.7	1.3	0.8	0.97
C8LK	62.9	27.1	8.9	-	-	-

**Figure 2.9:** (from left to right) X-ray diffraction patterns, FT-IR transmittance spectra, and elemental composition from SEM-EDX of C8NZ (red), C8LZ (blue), and C8LK (green).

significant vibration peak from the precursor was detected indicating the absence of initial functionalities from the precursor itself. However, a small difference among the spectra was appreciated in the fingerprint region where the C8LK profile displayed lower intensity bands with two maximums at 1600 cm^{-1} and 1250 cm^{-1} . In agreement with XRD patterns, FT-IR spectra indicates the structural difference between samples obtained in presence of zinc chloride (C8LZ and C8NZ) and in its absence (C8LK). This difference suggests the role of the salt as not innocent species in the chemical development of the material.

SEM-EDX spectra were recorded to understand the chemical composition of the materials in function of the salt used. Remarkably, C8NZ is a carbon-rich material as LZ-derived materials. Compared to C8LZ, it presents higher nitrogen content (i.e., 18.6 wt%) and oxygen content (i.e., 5.9wt%). On the other hand, C8LK presents significantly higher nitrogen content than previously reported materials (i.e., 27.1 wt%) while carbon has lower contribution (i.e., 62.9 wt%). Remarkably, the C8LK atomic C/N ratio is equal to 2.8 indicating the formation of a C_3N -like structure, whereas C8NZ and C8LZ present atomic C/N ratios equal to 8.7 and 6.3 respectively. Again, structural characterization displays a clear difference when zinc chloride is used during material synthesis. In particular, zinc can interact as Lewis acid with electron-rich nitrogen species (Lewis bases). Therefore, it is reasonable to conclude from SEM-EDX analysis that zinc can promote carbon-rich structures.

In order to understand the effect of different salt melts on the morphology of the materials, SEM, STEM (**Figure 2.10**), and gas adsorption and (**Figure 2.11**) were recorded for C8NZ and

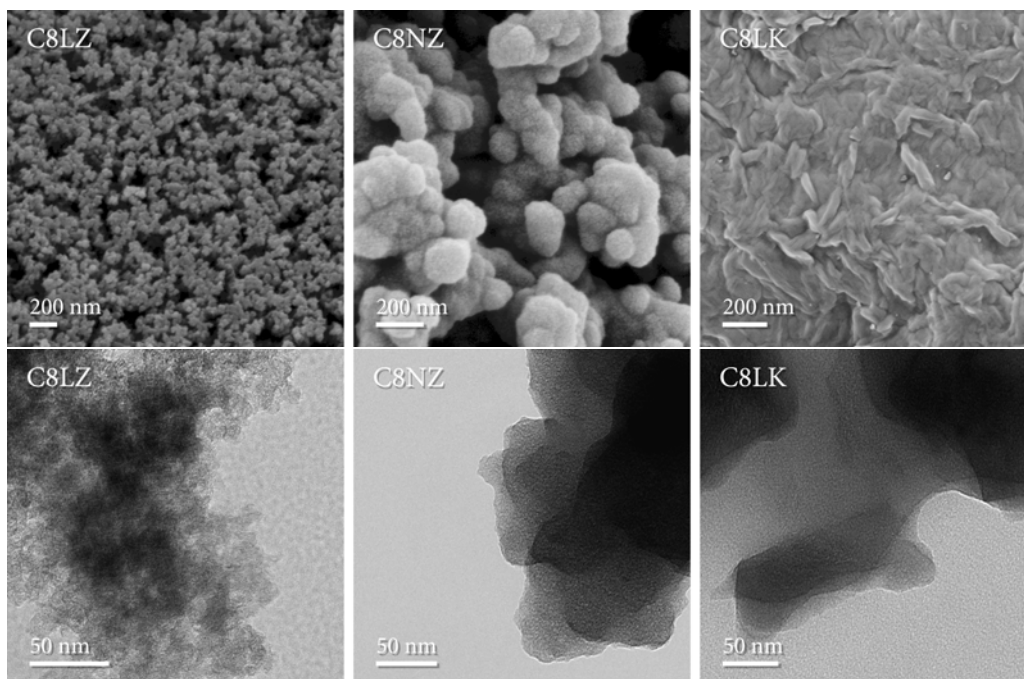


Figure 2.10: Scanning electron microscopy (first row) and Scanning transmission electron microscopy (second row) of (from left to right) C8LZ, C8NZ, and C8LK.

C8LK. SEM images show a clear difference among the samples indicating salt melt role during the material formation. While C8LZ is characterized by small colloids with a diameter smaller than 50 nm, C8NZ shows a bigger colloids (>100 nm) than C8LZ. This suggests that material growing speed was faster than nucleation speed in C8NZ. On the other hand, C8LZ forms with a faster nucleation compared to the growing speed resulting in smaller colloids. As C8LK displays flakes and blocks, a bad solvation process characterizes the formation of the material. This can be ascribed to a faster condensation than solvation due to the higher melting temperature of LiCl/KCl compared to LiCl/ZnCl₂ or LiCl/ZnCl₂ (see **Table 2.1**). Yet, zinc role in promoting solvation instead of condensation cannot be discarded and needs further investigation. STEM imaging further supports the previous statements. C8LZ and C8NZ present colloidal structures characterized by colloids of different dimensions, while C8LK shows a structure characterized by flakes. Finally, C8NZ and C8LK images appear as less porous materials compared to C8LZ suggesting the difference in surface area development when different salts are used.

Gas adsorption was used to characterize the specific surface area and the pore structures of the prepared materials (**Figure 2.11**). At first, nitrogen isotherm at 77 K indicates that C8LK has low nitrogen uptake (total pore volume equal to 0.04 cm³ g⁻¹). On the other hand, C8NZ presents higher total pore volume (2.1 cm³ g⁻¹) and its isotherm can be classified as type I accordingly to IUPAC guidelines indicating that the material is mainly microporous.[15] DFT pore size distribution confirmed these observations indicating the absence of a relevant pore structure in C8LK and a small population of pores around 2 nm for C8NZ, while C8LZ is richer in meso-pores. Specific surface was calculated by BET equation giving as results 1834 m² g⁻¹,

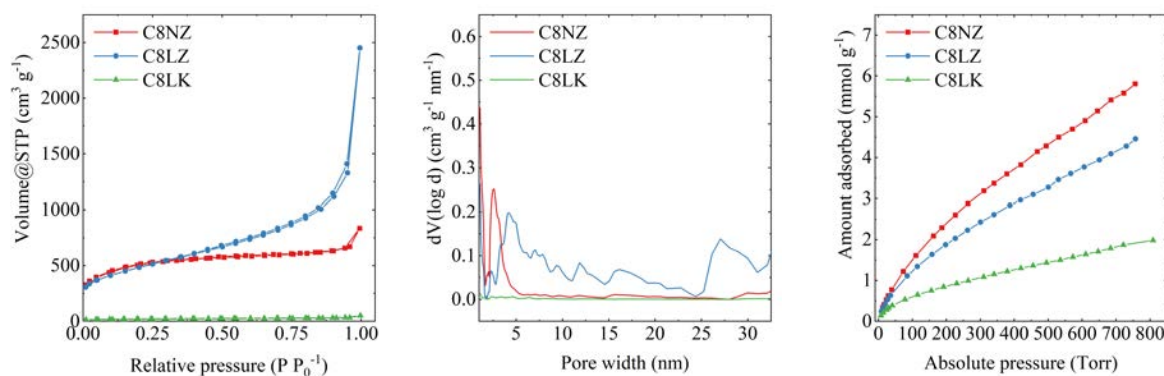


Figure 2.11: (From left to right) N₂ isotherms at 77K, DFT calculated pore size distribution, and CO₂ adsorption isotherm at 273K for C8NZ (red), C8LZ (blue), and C8LK (green).

Table 2.3: Gas adsorption data obtained from BET and DFT calculations applied on N₂ and CO₂ isotherms at 77K and 273K.

Material	Specific surface area ^a m ² g ⁻¹	Total pore volume (<40 nm) ^a cm ³ g ⁻¹	Total pore volume (<10 nm) ^b cm ³ g ⁻¹
C8NZ	1834	2.1	0.23
C8LZ	1701	2.1	0.18
C8LK	65	0.04	0.08

^a Calculated from nitrogen isotherm at 77 K.

^b Calculated from carbon dioxide isotherm at 273 K.

1701 m² g⁻¹, and 65 m² g⁻¹ for C8NZ, C8LZ, and C8LK, respectively.

CO₂ adsorption isotherms at 273 K confirm that C8LZ and C8NZ are more porous compared to C8LK. Still, C8LK adsorbed volume (i.e., 0.08 cm³ g⁻¹) is double compared to nitrogen adsorption results (0.04 cm³ g⁻¹, see **Table 2.3**). However, this is not surprising due to the higher nitrogen content of the material. C_xN are a class of materials known for their affinity towards CO₂, which explains the higher adsorption of carbon dioxide compared to nitrogen.[16] Similarly, C8NZ shows higher adsorbed volume compared to C8LZ can be ascribed to the higher nitrogen content of the NZ derived material.

To conclude, zinc chloride plays a fundamental role in the development of structural and morphological properties. C8NZ and C8LZ present lower nitrogen content and porous structures with higher surface areas compared to C8LK. It might be assumed that zinc promotes the decomposition of nitrogen-rich phases to a more porous structure. However, the bad solvation process (deduced from SEM and STEM imaging) cannot be discarded as an important variable in the discussion. Thus, lowering the temperature synthesis is fundamental to decrease the decomposition upon heat treatment and get a better picture by dividing the two variables.

2.4 Temperature dependence

As observed in the previous sections, the choice of precursor or salt melt influences the solvation and precipitation process leading to different morphologies. Moreover, zinc chloride favors material decomposition fostering carbon-rich phases. Yet, pores origin and material development during the synthesis remain unclear. Therefore, cytosine was treated in presence of LiCl/ZnCl₂ at different temperatures (i.e., 500 °C, 600 °C, 700 °C, and 800°C) in order to observe and characterize the intermediate steps which are leading to the final material (**Table 2.1**).

Table 2.1: Summary of the material synthesized, codes and yields.

Precursor	Salt	T _{synthesis} °C	Code	Yield ^a wt%
Cytosine	LiCl/ZnCl ₂	500	C5LZ	50
		600	C6LZ	50
		700	C7LZ	40
		800	C8LZ	28

^a The yield was calculated as fraction between the final material mass and the initial precursor mass.

TGA profiles obtained from C5LZ, C6LZ, and C7LZ in nitrogen show a material phase that starts to decompose above 600 °C (**Figure 2.12**). This decomposition leads to a more thermally stable phase corresponding to C8LZ. On the other hand, thermal decomposition in synthetic air is surprisingly similar among the samples indicating the stability upon heating and in presence of oxygen. This shows C5LZ, C6LZ, and C7LZ as extremely stable materials against oxidation.

Structural characterization was performed by XRD, FTIR, and SEM-EDX analysis (**Figure 2.13**). Similar to C8LZ, the C7LZ diffraction pattern is characterized by the increased intensity at low angles suggesting a microporous structure. In contrast, C5LZ and C6LZ patterns display the presence of a broad band at 26.5°, which indicates a poor graphitic stacking in C5LZ or C6LZ.[11] Its absence in C7LZ and C8LZ indicates a de-stacking process that happens above

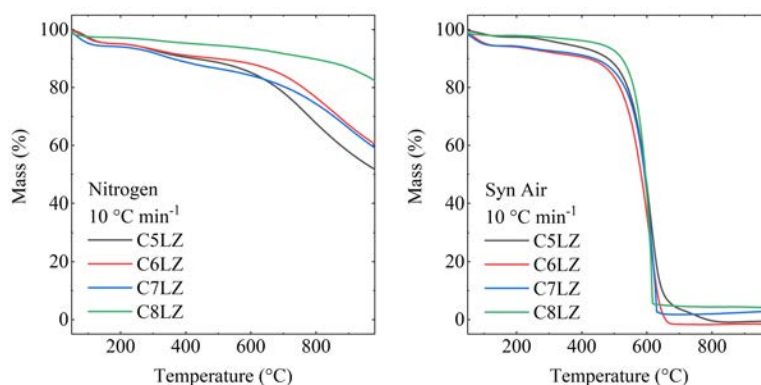


Figure 2.12: Thermogravimetric analysis at 10 K min⁻¹ of (from left to right) materials in nitrogen and materials in synthetic air.

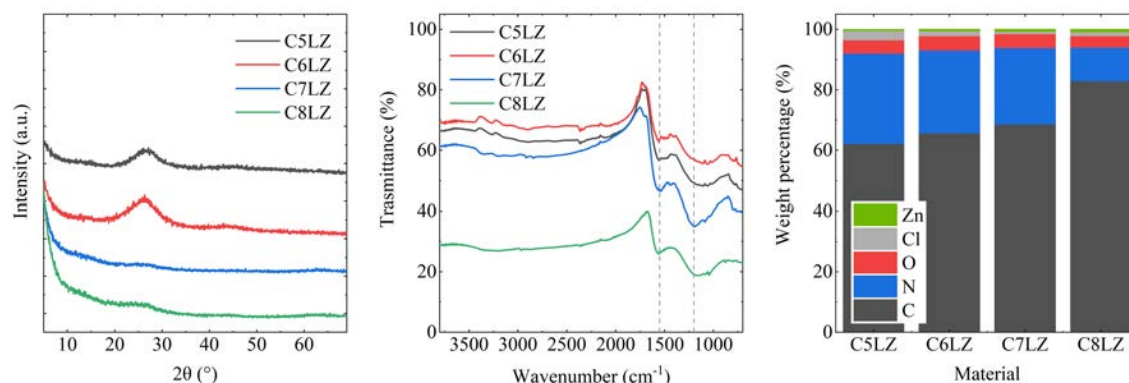


Figure 2.13: (from left to right) X-ray diffraction patterns, FT-IR transmittance spectra, and elemental composition from SEM-EDX.

700 $^\circ\text{C}$ and might be promoted by zinc chloride. Indeed, the absence of zinc chloride for C5LZ and C6LZ drove to a XRD pattern similar to C8LK (see **Figure 2.9**).

Characteristic vibration were investigated by FT-IR spectroscopy (**Figure 2.13**). The C5LZ spectrum is characterized by higher transmittance (i.e., from 80% to 40%) than the C8LZ one indicating lower conjugation in the structure. Moreover, the presence of more defined bands at 1600 cm^{-1} and 1250 cm^{-1} (C-N stretching and C-C stretching, respectively) suggest the absence of a high condensed phase as observed from C8LZ spectra. Remarkably, C5LZ, C6LZ, and C7LZ have similar average transmittance intensity, which is higher than C8LZ transmittance. This indicates that a different phase compared to C5LZ, C6LZ, and C7LZ forms at 800 $^\circ\text{C}$

SEM-EDX spectroscopy corroborates what was observed in the previous paragraphs. Material composition changes coherently from C5LZ to C8LZ with an increase in carbon content and a decrease in nitrogen weight percentage. Specifically, carbon content increases from 62.2 wt% for C5LZ to 82.9 wt% for C8LZ, while nitrogen decreases from 29.8 wt% to 11.1 wt% for the same materials. This is influenced by zinc chloride, which acts as Lewis acid and interacts with electron-rich nitrogen atoms helping their decomposition as previously hypothesized by comparing different salt melts. Remarkably, while nitrogen content decreases linearly from C5LZ to C7LZ, C8LZ composition does not follow the linear trend showing much lower nitrogen content. This result corroborates the formation of a new phase at 800 $^\circ\text{C}$ as suggested by the thermal stability in inert atmosphere observed in **Figure 2.12** and the FTIR spectra reported in **Figure 2.13**.

As in the previous sections, morphological analysis was run by SEM, STEM, and gas adsorption (**Figure 2.14**). Colloidal morphology was observed in all the samples indicating that the solvation-precipitation process happens before or at 500 $^\circ\text{C}$. Remarkably, SEM images show a more open morphology at higher synthetic temperatures, which might be the consequence of material decomposition. If so, the images suggest that this decomposition has a higher influence when the synthetic temperature is increased as observed for SEM-EDX. STEM imaging further

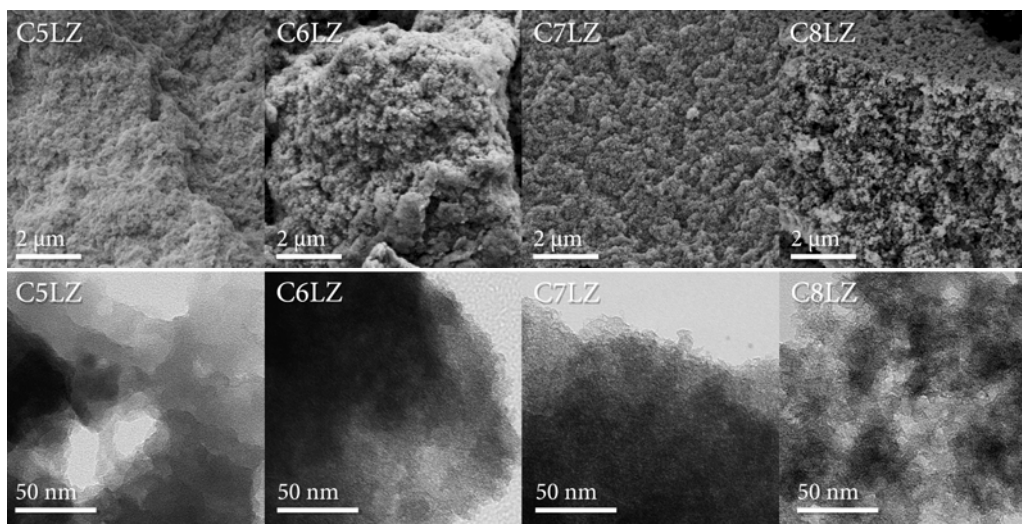


Figure 2.14: Scanning electron microscopy (first row) and Scanning transmission electron microscopy (second row) of (from left to right) C5LZ, C6LZ, C7LZ, and C8LZ.

corroborates SEM analysis. The increase in synthetic temperature induces the formation of a less compact structure with its maximum at 800 °C.

Gas adsorption isotherms help understand the temperature dependence of the porous network formation (**Figure 2.15**). Nitrogen isotherms at 77K show higher adsorbed volume when the synthetic temperature is increased (see **Table 2.3**). This increased volume is related to the formation of a microporous structure observed by the type I isotherms for C6LZ and C7LZ, which become a combination of type I and type II for C8LZ. Moreover, the micropore volume increases constantly from C5LZ to C8LZ resulting in higher surface areas calculated through BET equation: 44 m² g⁻¹, 749 m² g⁻¹, 1207 m² g⁻¹, and 1701 m² g⁻¹ (see **Table 2.3**). Noteworthy, microporous structures are often obtained from decomposition or activation processes. Therefore, the increased micropore volume and surface areas agree with a partial decomposition of the material upon heat treatment. However, this does not describe the effect of the sol-gel-like process on the mesopore structure. Hence, pore size distribution was calculated by DFT modeling to understand its development with temperature showing that all samples present a volume adsorbed by 5 nm mesopores. Similar narrow mesopores were observed in the previous sections indicating their formation as a function of the sol-gel-like process. Yet, higher

Table 2.2: Composition summary of materials obtained at different temperatures.

Material	SEM-EDX					ICP-EOS
	wt%					wt%
	C	N	O	Cl	Zn	Zn
C5LZ	62.2	29.8	4.3	3.1	0.3	0.06
C6LZ	65.7	27.4	4.7	1.6	0.5	0.25
C7LZ	68.7	25.2	4.5	0.8	0.7	0.88
C8LZ	82.9	11.1	3.7	1.3	0.8	0.97

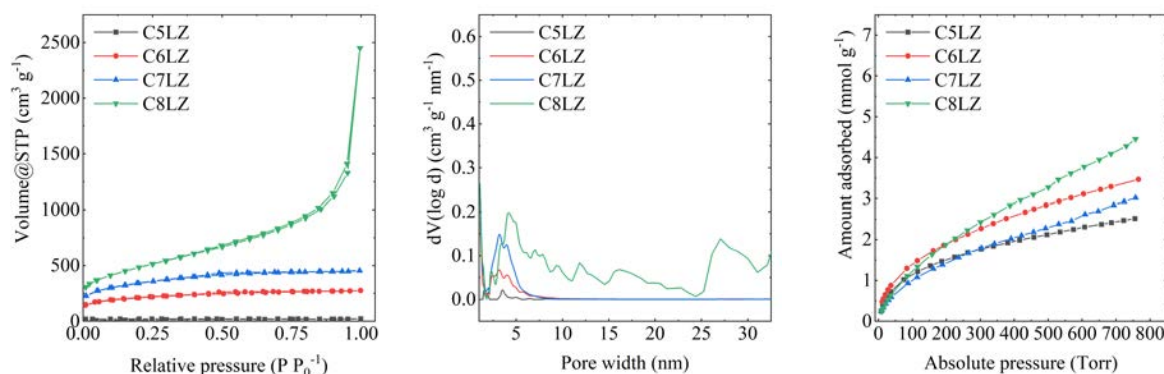


Figure 2.15: (From left to right) N₂ isotherms at 77K, DFT calculated pore size distribution, and CO₂ adsorption isotherm at 273K for C5LZ, C6LZ, C7LZ, and C8LZ.

Table 2.3: Gas adsorption data obtained from BET and DFT calculations applied on N₂ and CO₂ isotherms at 77K and 273K.

Material	Specific surface area ^a	Total pore volume (<40 nm) ^a	Total pore volume (<10 nm) ^b
	m ² g ⁻¹	cm ³ g ⁻¹	cm ³ g ⁻¹
C5LZ	44	0.03	0.10
C6LZ	749	0.4	0.14
C7LZ	1207	0.7	0.12
C8LZ	1701	2.1	0.18

^a Calculated from nitrogen isotherm at 77 K.

^b Calculated from carbon dioxide isotherm at 273 K.

mesopore volume is formed as wide distribution of pore dimensions above 800 °C in presence of LiCl/ZnCl₂. These might be the consequence of the further material degradation observed as well by SEM-EDX and electron microscopy.

Carbon dioxide adsorption isotherms at 273 K highlight high adsorbed volume. C5LZ pore volume calculated from CO₂ isotherm is higher compared to nitrogen-derived pore volume. Furthermore, C6LZ has higher carbon dioxide adsorbed volume compared to C7LZ. As described in the previous section, this is not surprisingly due to the higher affinity of highly nitrogen-doped structures.[16] Yet, once the decomposition proceeds and a high microporous volume is formed, its influence overcomes the material affinity and leads to the highest pore volume as seen for the C8LZ isotherm.

In conclusion, the material composition and the pore structure can be tuned by varying the working temperature. Indeed, lower temperature implies higher nitrogen content and more microporous structures. At 800 °C, a more carbon-rich mesoporous material is formed. Nonetheless, a small fraction of narrow mesopores (i.e., < 5 nm) was observed and associated with the sol-gel-like mechanism characteristic of the salt melt templating synthesis.

Bibliography

- [1] Liu, X., Fechler, N. & Antonietti, M. Salt melt synthesis of ceramics, semiconductors and carbon nanostructures. *Chemical Society Review* **42**, 8237–8265 (2013).
- [2] Fellinger, T.-P. Sol–gel carbons from ionothermal syntheses. *Journal of Sol-Gel Science and Technology* **81**, 52–58 (2017).
- [3] Díez, N., Fuertes, A. B. & Sevilla, M. Molten salt strategies towards carbon materials for energy storage and conversion. *Energy Storage Materials* **38**, 50–69 (2021).
- [4] Fechler, N., Fellinger, T.-P. & Antonietti, M. “salt templating”: A simple and sustainable pathway toward highly porous functional carbons from ionic liquids. *Advanced Materials* **25**, 75–79 (2013).
- [5] Soukup, G. A. *Nucleic Acids: General Properties* (John Wiley Sons, Ltd, 2003).
- [6] Antonietti, M. & Oschatz, M. The concept of “noble, heteroatom-doped carbons,” their directed synthesis by electronic band control of carbonization, and applications in catalysis and energy materials. *Advanced Materials* **30**, 1706836 (2018).
- [7] Yanson, I. K., Teplitsky, A. B. & Sukhodub, L. F. Experimental studies of molecular interactions between nitrogen bases of nucleic acids. *Biopolymers* **18**, 1149–1170 (1979).
- [8] Emel’yanenko, V. N. & Verevkin, S. P. Thermodynamic properties of caffeine: Reconciliation of available experimental data. *The Journal of Chemical Thermodynamics* **40**, 1661–1665 (2008).
- [9] Kossmann, J., Rothe, R., Heil, T., Antonietti, M. & López-Salas, N. Ultrahigh water sorption on highly nitrogen doped carbonaceous materials derived from uric acid. *Journal of Colloid and Interface Science* **602**, 880–888 (2021).
- [10] Lepre, E. I need to find this and i hope to not forget it, if not, ciao future mum (2021).
- [11] Pfaff, T. *et al.* Comparative microstructural analysis of nongraphitic carbons by wide-angle x-ray and neutron scattering. *The Journal of Physical Chemistry C* **123**, 20532–20546 (2019).

- [12] Țucureanu, V., Matei, A. & Avram, A. M. Ftir spectroscopy for carbon family study. *Critical Reviews in Analytical Chemistry* **46**, 502–520 (2016). PMID: 26941009.
- [13] Wang, H., Maiyalagan, T. & Wang, X. Review on recent progress in nitrogen-doped graphene: Synthesis, characterization, and its potential applications. *ACS Catalysis* **2**, 781–794 (2012).
- [14] Chen, W. *et al.* Heteroatom-doped carbon materials: Synthesis, mechanism, and application for sodium-ion batteries. *Small Methods* **3**, 1800323 (2019).
- [15] Thommes, M. *et al.* Physisorption of gases, with special reference to the evaluation of surface area and pore size distribution (iupac technical report). *Pure and Applied Chemistry* **87**, 1051–1069 (2015).
- [16] Kossmann, J. *et al.* Guanine condensates as covalent materials and the concept of cryptopores. *Carbon* **172**, 497–505 (2021).

Chapter 3

Oxidation resistance for Li-ion capacitor cathodes

3.1 The role of electrode preparation

Carbon-based materials are established candidates as cathodes for EES devices thanks to their low cost of production and high specific surface area.[1] Recently, the role of nitrogen doping was shown to improve the performance of the materials.[2] Yet, a massive increase in nitrogen content is followed by a decrease in conductivity.[3] Thus, the mixture with a conductive carbon is a promising strategy to develop composite materials combining a high conductive material with low performance and a high performing material with low conductivity.[4]

Even though the process of mixing is critical in the final device performance, electrodes preparation from powdery materials is not a standardized process and it varies easily depending on the laboratory.[5] Among the different strategies, the most common are stirring, ultrasonication, and ball-milling (see **Figure 3.1**). As mild mixing processes, stirring and ultrasonication consume less energy and they have lower effect on the chemical structure of the active material. On the other hand, ball-milling performs a better homogenization of the components but is harsher process. Indeed, the high speed of rotation drives to high energy collisions between metal balls and materials, which promote metal leaking from the balls and oxidation of the materials.[6]

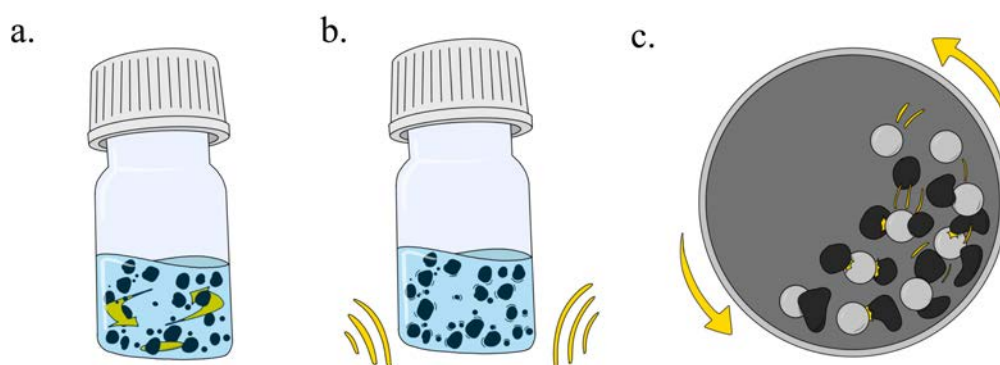


Figure 3.1: Graphical representation of different methods for ink preparation. From left to right: a. stirring, b. sonication and c. ballmilling.

Chapter 2 introduced the synthesis of materials from nucleobases and salt melt templated methods. These fit the characteristic required as active cathode materials (i.e. high specific surface area and high nitrogen content). Moreover, they are supposed to present high stability upon oxidation accordingly to Antonietti et al.[7]. This may prevent their chemical modification upon ball milling and help the production of composites materials. Hence, this chapter aims to describe the effect of ball milling on the chemical properties and the use as cathodes in Li-ion capacitor of highly nitrogen doped carbonaceous materials.

3.2 Caffeine derived materials

Caffeine, adenine, and cytosine were used as material precursors in **Chapter 2.2**. While the two nucleobases are quite expensive (i.e. 50 EUR g⁻¹ from Merk), caffeine is a much cheaper molecule (i.e. 50 EUR Kg⁻¹ from Merk). Hence, the study of cathode materials from caffeine does not only promise deep fundamental knowledge, but potentially gives a device with larger applicability compared to cytosine- or adenine-derived ones.

Nevertheless, the material obtained from caffeine and LiCl/ZnCl₂ (i.e. CF8LZ) has the lowest surface area and pore volume in **Chapter 2.2**. In order to improve the electrochemical performance of cathode materials, it is fundamental to synthesize materials with larger specific surface area and pore volumes. Hence, LiCl/KCl and NaCl/ZnCl₂ were used as alternative salts to LiCl/ZnCl₂ to obtain more porous materials. No caffeine leftover was observed from the use of LiCl/KCl highlighting the Zn role described in the previous chapter. On the other hand, NaCl/ZnCl₂ promoted the formation of a carbonaceous material at 800 °C in 25% as yield. Moreover, one lower temperature compared to 800 °C (i.e. 700 °C) was investigated to increase the nitrogen doping. These materials will be named accordingly to **Chapter 2** and **Table 5.1** reports their summary.

To further describe the ball milling effect on carbon-based materials, a commercial active carbon (i.e. Kuraray) was used as reference in this study. The commercial carbon was investigated as pristine and as nitrogen-doped. The doping was performed by the thermal decomposition of cyanamide on the material surface and it is described in detail in the experimental section. **Table 5.1** reports the summary of the materials that will be name as **Kur** (pristine Kuraray) and **N-Kur** (nitrogen-doped Kuraray).

Elemental chemical analysis helped to elucidate the composition of the materials (see **Table 3.2**). CF7NZ shows the highest nitrogen content (i.e. 19.0 wt%), while Kur presents a negligible percentage of nitrogen in the structure (i.e. 0.3 wt%). The doping method of Kur increased successfully the nitrogen level to 5 wt% in N-Kur, but it increased the oxygen content from 3.5 wt% to 7.6 wt% as well. These values remain lower than CF8NZ and CF7NZ oxygen contents

Table 3.1: Summary of the material synthesized, codes and yields.

Precursor	Salt	T _{synthesis} °C	Code	Yield ^a wt%
Caffeine	NaCl/ZnCl ₂	700	CF7LZ	28
		800	CF8LZ	25
Kuraray	-	-	Kur	
		900	N-Kur	

^a The yield was calculated as a fraction between the final material mass and the initial precursor mass.

which are equal to 13.5 wt% and 16.0 wt%, respectively. Yet, it is not possible to discriminate whether this content is structural or from adsorbed water molecules as previously described in **Chapter 2**.

Nitrogen sorption experiments at 77 K showed that CF7NZ and CF8NZ isotherms are type I (see **Figure 3.2**).[8] Both samples showed similar specific surface area from BET equation ($1496 \text{ m}^2 \text{ g}^{-1}$ and $1446 \text{ m}^2 \text{ g}^{-1}$) and pore volume (i.e. $0.654 \text{ cm}^3 \text{ g}^{-1}$ and $0.641 \text{ cm}^3 \text{ g}^{-1}$) suggesting lower dependence between temperature and pore structure when caffeine is used as precursor. The less optimal solvation process - which was pointed out for caffeine in **Chapter 2.2** - might be crucial in lowering the pore structure-temperature dependence. On the other hand, Kur and N-Kur present a similar shape (type I and type IV) but with less adsorbed volume for the nitrogen doped material (see **Table 7.11**). Accordingly to the isotherm shapes, the analysis of DFT pore size distribution indicates that all materials have 2 nm pores.

CO_2 adsorption isotherms show larger differences than N_2 isotherms (see **Figure 3.2**). Kur presents the lowest pore volume calculated from carbon dioxide ($0.189 \text{ cm}^3 \text{ g}^{-1}$) while CF7NZ has the highest value ($0.254 \text{ cm}^3 \text{ g}^{-1}$). Moreover, the pore volume increases proportionally to the nitrogen content of the materials (see **Table 7.11** and **Table 3.2**). Nitrogen doping is a well-known strategy to increase the carbon dioxide uptake in carbon-based material and the results agree with literature.[9–11]

Structural properties were evaluated by FT-IR and powder X-ray diffraction (**Figure 3.2**). Accordingly with the higher nitrogen content, CF7NZ and CF8NZ present lower transmittance compared to Kur and N-Kur. Interestingly, CF7NZ shows the presence of more defined broad peaks suggesting the presence of more defined functionalities. These are lost upon heating as observed for CF8NZ spectra, which is similar to Kur and N-Kur. On the other hand, XRD diffraction patterns are characterized by the absence of defined peaks indicating amorphous structures. A broad band at 26.5° can be observed for all the materials indicating poor graphitic stacking. However, only Kur and N-Kur patterns present the second broad band at 45° typical of in-plane C-C diffraction.[12] These are not visible for caffeine-derived materials and it might be caused by the higher nitrogen content.

Table 3.2: Elemental composition calculated from ECA and ICP-AES for CF7NZ, CF8NZ, Kur, and N-Kur.

Material	Elemental analysis			ICP-EOS
	wt%			wt%
	C	N	O	Fe
CF7NZ	61.4	19.0	16.0	0.02
CF8NZ	62.7	12.6	13.5	0.02
Kur	97.9	0.3	3.5	0.002
N-Kur	89.2	5.6	7.6	0.007

Table 3.3: specific surface area calculated through BET equation and pore volume from N₂ isotherm at 77 K and pore volume calculated from CO₂ isotherm at 273 K for CF7NZ, CF8NZ, Kur, and N-Kur.

Material	Specific surface area ^a	Pore volume (d<40 nm) ^a		Pore volume (d<10 nm) ^b
	m ² g ⁻¹	cm ³ g ⁻¹		cm ³ g ⁻¹
CF7NZ	1496	0.654		0.254
CF8NZ	1446	0.641		0.224
Kur	1672	0.763		0.189
N-Kur	1422	0.635		0.219

^a Calculated from nitrogen isotherm at 77 K.

^b Calculated from carbon dioxide isotherm at 273 K.

TGA analysis in synthetic air was used to characterize the thermal properties of the materials. Contrary to what was expected, Kur and N-Kur present the main mass loss at higher temperatures compared to CF7NZ and CF8NZ (see **Figure 3.2**). Yet, it can not be considered indicative of the material resistance to oxidation upon ball milling. Thermogravimetric analysis can not consider the effect of stainless steel ball, which undergoes through different chemical mechanism compared to simple combustion. For example, carbon-based materials were reported as unstable upon ball milling.[13, 14] The high oxidative environment induces these materials to absorb iron from the sample and it was concluded that the iron leakage was associated with the oxidation of the carbon.[5]

CF7NZ, CF8NZ, Kur, and N-Kur compositions from the elemental analysis were compared before (**Table 3.2**) and after (**Table 3.4**) ball-milling in stainless steel jar and in atmospheric air for 50 minutes. Both Kur and N-Kur presented a significant decrease in the carbon content upon grinding (from 90 wt% to 70 wt%) while CF7NZ and CF8NZ did not. The decrease in carbon is associated with an increase of oxygen (from 5 wt% to 10 wt%) and iron content (from 0 wt% to 9 wt%) for the commercial materials, which confirms the involvement of iron in the oxidation process. Remarkably, CF7NZ and CF8NZ do not show significant changes in composition or iron uptake confirming their potential to stand the harsh ball milling conditions.

Table 3.4: Elemental composition calculated from ECA and ICP-AES for CF7NZ, CF8NZ, Kur, and N-Kur after ball milling with stainless steel jar in open atmosphere for 50 min.

Material	Elemental analysis			ICP-EOS
	wt%			wt%
	C	N	O	Fe
CF7NZ	60.1	18.0	14.4	0.21
CF8NZ	60.8	12.7	15.7	0.50
Kur	73.9	1.1	12.1	9.52
N-Kur	71.2	5.0	10.0	8.24

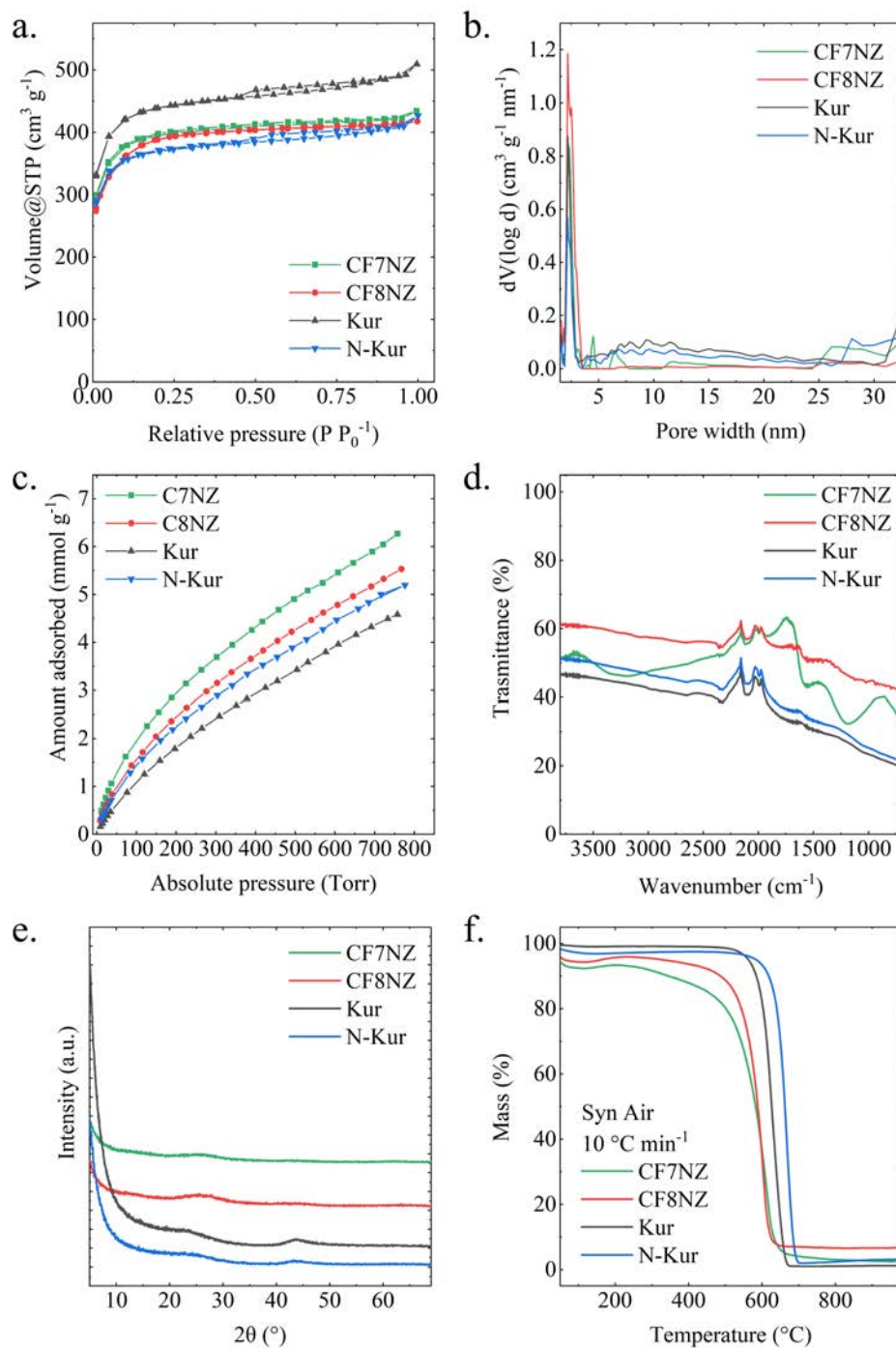


Figure 3.2: a. N_2 isotherm at 77 K, b. DFT pore size distribution from N_2 isotherm at 77 K, c. CO_2 adsorption isotherm at 273 K, d. FT-IR spectra, e. X-ray diffraction pattern, and f. thermogravimetric analysis in synthetic air at $10 K min^{-1}$ for CF7NZ, CF8NZ, Kur, and N-Kur.

3.3 Ball milled derived cathode materials

The different powder materials were mixed with a conductive additive and ground for 50 minutes. Afterward, a binder dispersion in NMP was added and the mixture was further ball milled for 10 minutes. Upon drying, the composite materials were obtained and used as cathodes for hybrid Li-ion capacitors. These materials will be named as **g-C/CODE**, where **g-** stands for ball milled, **C/** stands for the conductive additive and **CODE** is the starting material code introduced in **table 3.1**.

At first, the performances of the different composite materials were evaluated by charging-discharging measurements at 0.2 A g^{-1} . **Figure 3.3** reports the comparison of the 50th cycle and highlights the better performance of caffeine derived composite cathodes compared to commercial carbon derived composite materials. g-C/CF7NZ shows the best performances having higher capacity compared to g-C/CF8NZ and more than double performance compared to g-C/Kur and g-C/N-Kur. Due to the similar specific surface area values and pore size distributions, the cathode performances can be correlated to the higher nitrogen content observed for CF7NZ.

The importance of ball milling as a preparation method was evaluated by charging-discharging measurements. **Figure 3.3** compares the 50th cycle of charging-discharging at 0.2 A g^{-1} of two cathodes obtained with (g-C/CF7NZ) and without (C/CF7NZ) prior ball milling. The grinding process improves the capacity of the composite material almost five times compared to not ground sample proving the importance of this step.

Scanning electron microscopy and energy-dispersive X-ray spectroscopy gave a better understanding over the differences that ball milling introduces in the cathode material. SEM images reported in **Figure 3.4** show smaller particles for g-C/CF7NZ compared to C/CF7NZ. This influences the contact between the particles of CF7NZ and the conductive material. Moreover, EDX mapping reported in **Figure 3.4** shows a higher degree of homogeneity of heteroatom distribution for g-C/CF7NZ compared to C/CF7NZ. This indicates that ball milling prevents the formation of carbon-rich areas as observed for C/CF7NZ and it fosters a better mixing between the active material and the conductive additive. Hence, the higher homogeneity in composition and better contact between the two phases are identified as leading factors in the better performances observed for g-C/CF7NZ. These are directly influenced by the ball milling step which is crucial to develop cathode material for highly doped nitrogen materials.

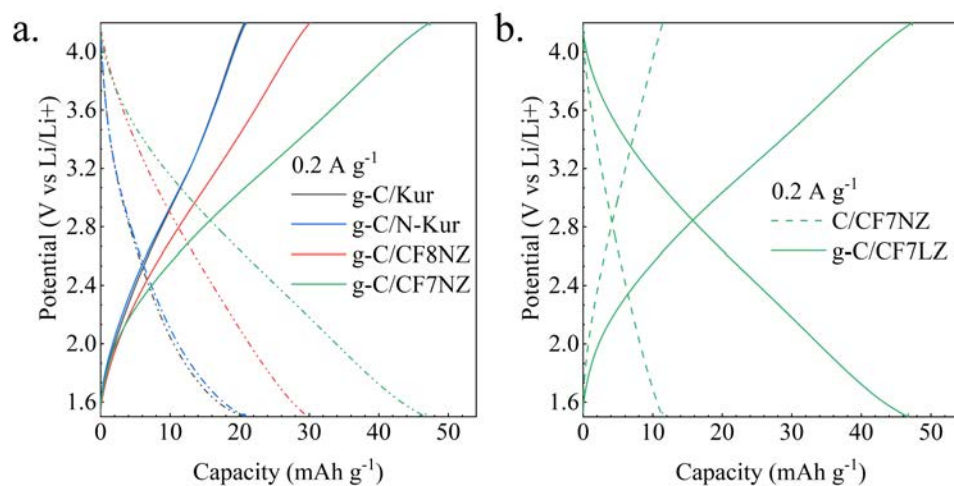


Figure 3.3: 50th cycle charging and discharging curve of a. different composite materials and b. CF7NZ derived composites with and without prior ball milling.

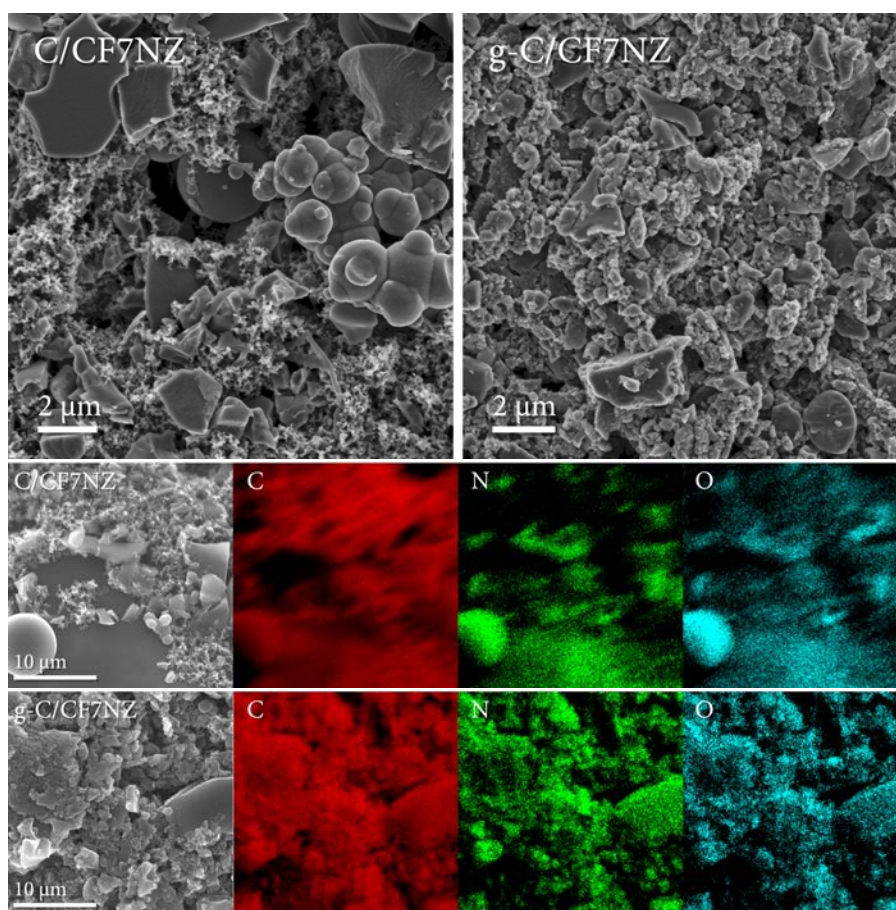


Figure 3.4: Scanning electron microscopy of the cathode material with and without prior ball milling and energy-dispersive X-ray spectroscopy of the cathode material with and without prior ball milling.

3.4 Performance of a caffeine derived cathode

Electrochemical performance of g-C/CF7NZ as Li-ion cathode was studied in depth via cyclic voltammetry and charging-discharging tests. At first, cyclic voltammetry experiments were performed at varying scan rates starting from 5 mV s^{-1} for 30 cycle in order to stabilize the integral of the voltammogram (**Figure 3.5a**). Afterward, cyclic voltammetry was measured at different scan rates without observing a significant change in the shape of the curve (**Figure 3.5b**). Cyclic voltammetry experiments are characterized by a distorted rectangular shape, which is typical for hybrid lithium capacitors. The distortion can be ascribed to the limited accessibility of cations into the pores at the potential below the open-circuits voltage (around 3.2V , as calculated from **Figure 3.5c**).[15]

From experiments at varying scan rates, surface- and diffusion-controlled contributions to the capacity were determined according to the well described model in the previous studies.[16, 17] As expected for a capacitor, an almost purely surface-controlled reaction was observed (**Figure 3.5d**).[18] Details on the calculation can be found in the **Appendix** method section, and the assessment of the model can be found in **Figure 3.5e**. The comparison of the calculated and the measured cyclic voltammetry is reported in **Figure 3.5f**.

Following cyclic voltammetry experiments, charging-discharging tests at increasing current densities were recorded from 0.05 A g^{-1} to 0.8 A g^{-1} (see **Figure 3.6**). At a current density of 0.05 A g^{-1} , the maximum observed discharge capacities are around 55 mAh g^{-1} , and they decrease upon increase in current density as expected. However, no significant reduction has been observed as discharge capacities of around 30 mAh g^{-1} are visible at a high current density to the original value of 0.05 A g^{-1} . Upon the decrease in current density to the original value of 0.05 A g^{-1} , the capacities increase reaching similar values as in the first 20 cycles, pointing that no damage was done to the samples at higher current densities.

As expected for hybrid lithium capacitors, charging-discharging profiles are distorted triangles (**Figure 3.6**). Additionally, they show that both charging and discharging are quick so that a full cycle occurs in less than 5 min at 0.8 A g^{-1} . Finally, charging-discharging tests at constant current 0.8 A g^{-1} for 300 cycles were run. After the first 100 cycles, the capacity reached 45 mAh g^{-1} retaining the said capacity without significant loss after 200 more cycles. In particular, the increasing capacity during the first 100 cycle can be ascribed to the wetting process of the electrodes.

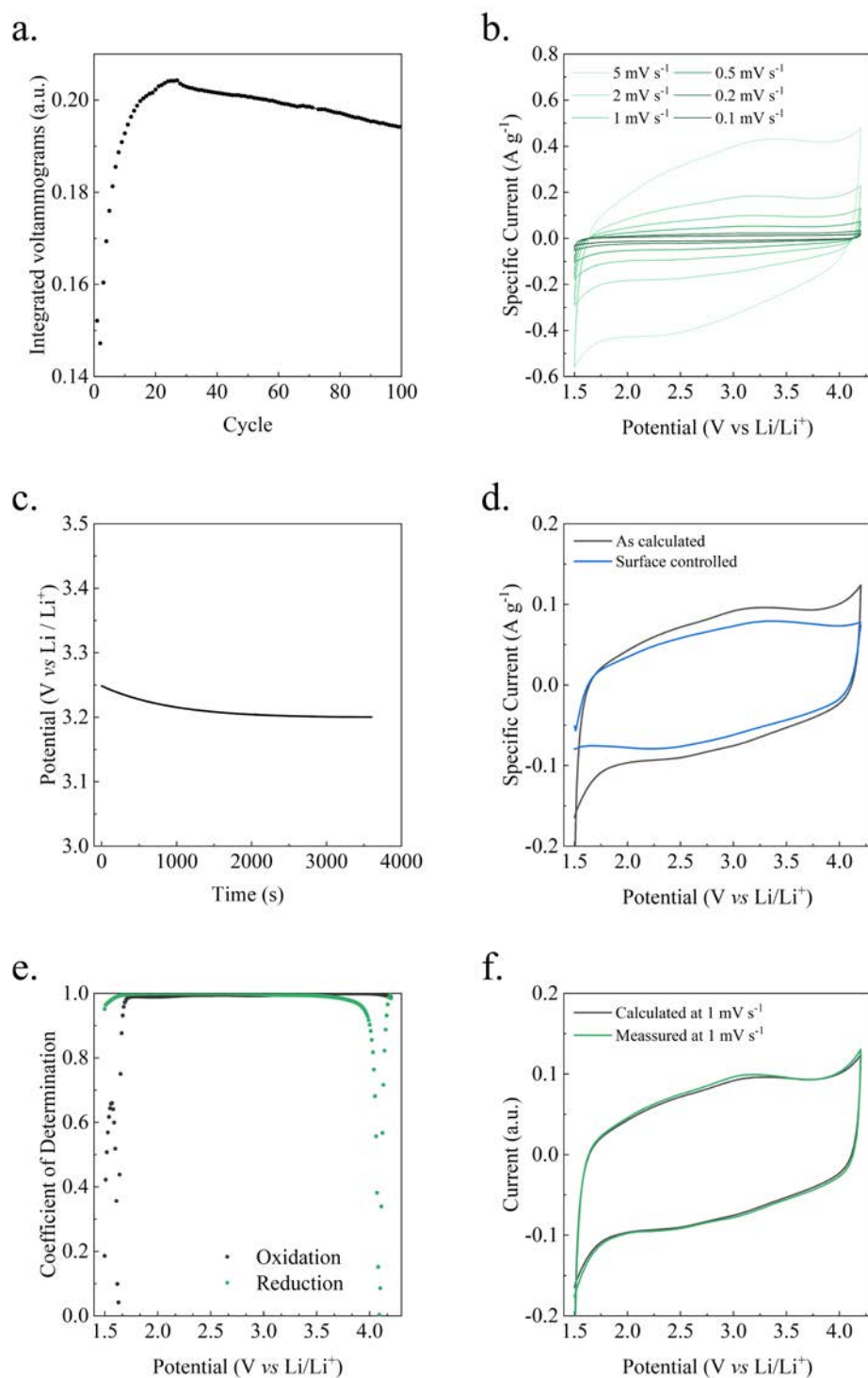


Figure 3.5: a. Integrated cyclic voltammograms at 5 mV s⁻¹, b. Cyclic voltammetry at varying scan rates, c. Open circuit voltage of the cell before cyclic voltammetry test, d. calculated surface-controlled contribution to capacity, e. assessment of the model used for surface-controlled contribution evaluation, f. cyclic voltammogram at 1 mV s⁻¹ as calculated and as measured.

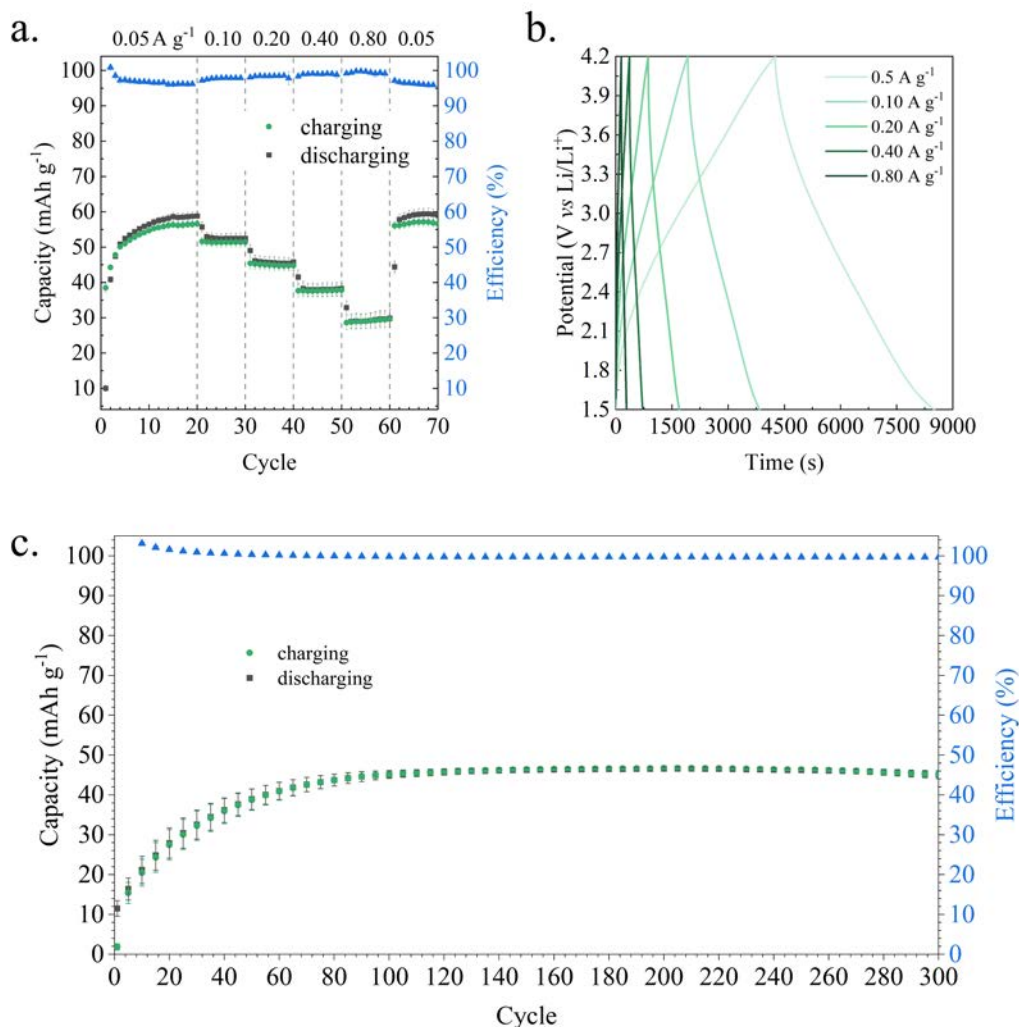


Figure 3.6: a. Charging-discharging test at varying current densities, b. Charging-discharging profiles at different current densities, c. charging-discharging test at 0.8 A g⁻¹ for 300 cycles.

Active carbon based cathode materials are characterized by 30 mAh g⁻¹ at 1 A g⁻¹. [19] Compared to active carbon, the presented capacitor performs better, and it can be related to the high heteroatom content. Nonetheless, mesoporous carbon-based cathodes are reported to have a capacity ranging from 65 mAh g⁻¹ to 80 mAh g⁻¹. [19, 20] These performances can be further improved to 120 mAh g⁻¹ at a similar current density when mesoporous doped carbon is used, achieving comparable performance to reduced graphene oxide. [21, 22] Hence, further studies are needed to study the effect of ball milling on the pore structure or use synthesis conditions to promote the formation of larger mesopores volume.

Bibliography

- [1] Simon, P. & Gogotsi, Y. Materials for electrochemical capacitors. *Nature Materials* **7**, 845–854 (2008).
- [2] Dubal, D. *et al.* Polypyrrole nanopipes as a promising cathode material for li-ion batteries and li-ion capacitors: Two-in-one approach. *Energy Technology* **7**, 193–200 (2019).
- [3] Mousavi, H. & Moradian, R. Nitrogen and boron doping effects on the electrical conductivity of graphene and nanotube. *Solid State Sciences* **13**, 1459–1464 (2011).
- [4] Ilic, I. K. & Oschatz, M. The functional chameleon of materials chemistry—combining carbon structures into all-carbon hybrid nanomaterials with intrinsic porosity to overcome the “functionality-conductivity-dilemma” in electrochemical energy storage and electrocatalysis. *Small* **17**, 2007508 (2021).
- [5] Ilic, I. K., Lepre, E. & López-Salas, N. Caffeine-derived noble carbons as ball milling-resistant cathode materials for lithium-ion capacitors. *ACS Applied Materials & Interfaces* **13**, 29612–29618 (2021).
- [6] Vujković, M. *et al.* Mechanically activated carbonized rayon fibers as an electrochemical supercapacitor in aqueous solutions. *Electrochimica Acta* **245**, 796–806 (2017).
- [7] Antonietti, M. & Oschatz, M. The concept of “noble, heteroatom-doped carbons,” their directed synthesis by electronic band control of carbonization, and applications in catalysis and energy materials. *Advanced Materials* **30**, 1706836 (2018).
- [8] Thommes, M. *et al.* Physisorption of gases, with special reference to the evaluation of surface area and pore size distribution (iupac technical report). *Pure and Applied Chemistry* **87**, 1051–1069 (2015).
- [9] Wang, L. & Yang, R. T. Significantly increased co2 adsorption performance of nanostructured templated carbon by tuning surface area and nitrogen doping. *The Journal of Physical Chemistry C* **116**, 1099–1106 (2012).
- [10] Gong, J., Lin, H., Antonietti, M. & Yuan, J. Nitrogen-doped porous carbon nanosheets derived from poly(ionic liquid)s: hierarchical pore structures for efficient co2 capture and

- dye removal. *J. Mater. Chem. A* **4**, 7313–7321 (2016).
- [11] Gong, J., Lin, H., Grygiel, K. & Yuan, J. Main-chain poly(ionic liquid)-derived nitrogen-doped micro/mesoporous carbons for CO₂ capture and selective aerobic oxidation of alcohols. *Applied Materials Today* **7**, 159–168 (2017).
- [12] Pfaff, T. *et al.* Comparative microstructural analysis of nongraphitic carbons by wide-angle x-ray and neutron scattering. *The Journal of Physical Chemistry C* **123**, 20532–20546 (2019).
- [13] Vujković, M. *et al.* Mechanically activated carbonized rayon fibers as an electrochemical supercapacitor in aqueous solutions. *Electrochimica Acta* **245**, 796–806 (2017).
- [14] Leistenschneider, D. *et al.* Mechanochemical functionalization of carbon black at room temperature. *C* **4** (2018).
- [15] Ajuria, J. *et al.* Lithium and sodium ion capacitors with high energy and power densities based on carbons from recycled olive pits. *Journal of Power Sources* **359**, 17–26 (2017).
- [16] Liu, T.-C., Pell, W. G., Conway, B. E. & Roberson, S. L. Behavior of molybdenum nitrides as materials for electrochemical capacitors: Comparison with ruthenium oxide. *Journal of The Electrochemical Society* **145**, 1882–1888 (1998).
- [17] Ilic, I. K., Perovic, M. & Liedel, C. Interplay of porosity, wettability, and redox activity as determining factors for lithium–organic electrochemical energy storage using biomolecules. *ChemSusChem* **13**, 1856–1863 (2020).
- [18] Ding, J., Hu, W., Paek, E. & Mitlin, D. Review of hybrid ion capacitors: From aqueous to lithium to sodium. *Chemical Reviews* **118**, 6457–6498 (2018).
- [19] Xia, Q. *et al.* High energy and high power lithium-ion capacitors based on boron and nitrogen dual-doped 3d carbon nanofibers as both cathode and anode. *Advanced Energy Materials* **7**, 1701336 (2017).
- [20] Wang, H. *et al.* A high-energy lithium-ion capacitor by integration of a 3d interconnected titanium carbide nanoparticle chain anode with a pyridine-derived porous nitrogen-doped carbon cathode. *Advanced Functional Materials* **26**, 3082–3093 (2016).
- [21] Li, C., Zhang, X., Wang, K., Sun, X. & Ma, Y. High-power and long-life lithium-ion capacitors constructed from n-doped hierarchical carbon nanolayer cathode and mesoporous graphene anode. *Carbon* **140**, 237–248 (2018).
- [22] Dubal, D. P. & Gomez-Romero, P. All nanocarbon Li-ion capacitor with high energy and high power density. *Materials Today Energy* **8**, 109–117 (2018).

Chapter 4

Catalytic properties of carbonaceous materials

4.1 Nitrogen role in carbocatalysis

Activated charcoal has been known to promote the aerobic oxidation of organic molecules such as ethanol for over a century.[1] However, its activity has been overlooked as better results were observed with metal-based catalysis.[2] Nevertheless, the discovery of graphene and the increased sensibility on sustainability brought back the attention to carbon-driven catalytic processes. Indeed, during the last decade, numerous studies featuring carbon-based materials generated the field of carbocatalysis.[3, 4]

Among these studies, different nanostructured materials such as graphene,[5, 6] carbon nanotubes, or carbon nanodots [7] were used as pristine, defected, or doped derivatives to promote catalytic reactions. In particular, electron density manipulation via heteroatom doping has been one of the most studied strategies to increment catalytical performances.[8] Nitrogen doping plays a central role due to the similar atom size and higher electronegativity compared to carbon. Through its incorporation in the structure (**Figure 4.1**), it is possible to generate significant dipole moments, which can act in various ways as described in the introduction.[9, 10] Nevertheless, most of the reported preparation methods fail to increase the nitrogen content above 10 wt%, which limits the observable effect of heteroatom doping on the catalytic activity.[11]

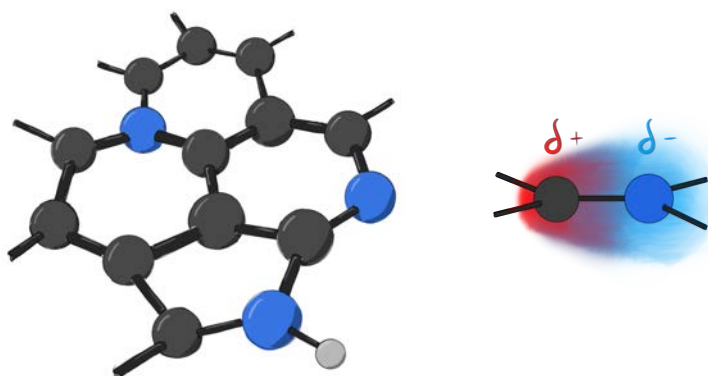


Figure 4.1: Graphical representation of nitrogen functions in a carbon network and electrical dipole moment in a carbon-nitrogen covalent bond.

Within this frame, the materials proposed in **Chapter 2** are good candidates to observe the relation between doping and catalytic activity at high nitrogen content ($50 \text{ wt\%} > x > 10 \text{ wt\%}$) in porous carbons. Hence, four materials from **Chapter 2.4** were chosen due to their different nitrogen content: C5LZ (29.8 wt%), C6LZ (27.4 wt%), C7LZ (25.2 wt%), and C8LZ (11.1 wt%). This chapter will describe their activity towards four model reactions: reduction of nitrobenzene, oxidation of 3,3',5,5'-Tetramethylbenzidine, the cycloaddition of carbon dioxide, and a two-step one-pot reaction involving acid and basic sites independently. Finally, the catalytic results will be correlated to the nitrogen speciation observed through N1s XPS.

4.2 Carbonaceous materials for redox catalysis

The reduction of nitroarenes to the corresponding amine is an important reaction in organic synthesis to produce key intermediates towards pharmaceuticals, polymers, pesticides, dyes, and other high-value products.[12, 13] For this reason, the catalytic properties were tested for the conversion of nitrobenzene to aniline as model reaction (**Figure 4.2**). Hydrazine was used as a reducing agent due to its relevance in industrial productions.[14]

Lasern et al. reported in 2000 that pure carbon materials can catalyze this reaction by creating an electron pool through the adsorption of hydrazine.[15] More recently, the importance of nitrogen doping to promote the adsorption of nitrobenzene was disclosed by Yang et al. and the role of boron-nitrogen co-doping for the adsorption of hydrazine by Li et al.[16, 17] Even though both papers show useful insights on the mechanism of the catalysis, they report carbon-based materials with the highest value of doping equal to 8 wt%. Hence, it is not possible to extrapolate the information with higher doping.

Based on these studies, the catalytic reduction of nitrobenzene with hydrazine at room temperature using a reaction time of 48 h was studied for the four carbonaceous materials taken in consideration. The molar conversion obtained through ¹H-NMR is reported in **Figure 4.2**. The desired product was obtained in high yield only when C8LZ was used and a small amount of it was observed for C7LZ as well. However, no presence of aniline was recorded for C5LZ and C6LZ. Moreover, a test without catalyst and two tests in presence of Kur and N-Kur (see **Chapter 3.2**) were run. Yet, no conversion of the reagent was observed after 48 h.

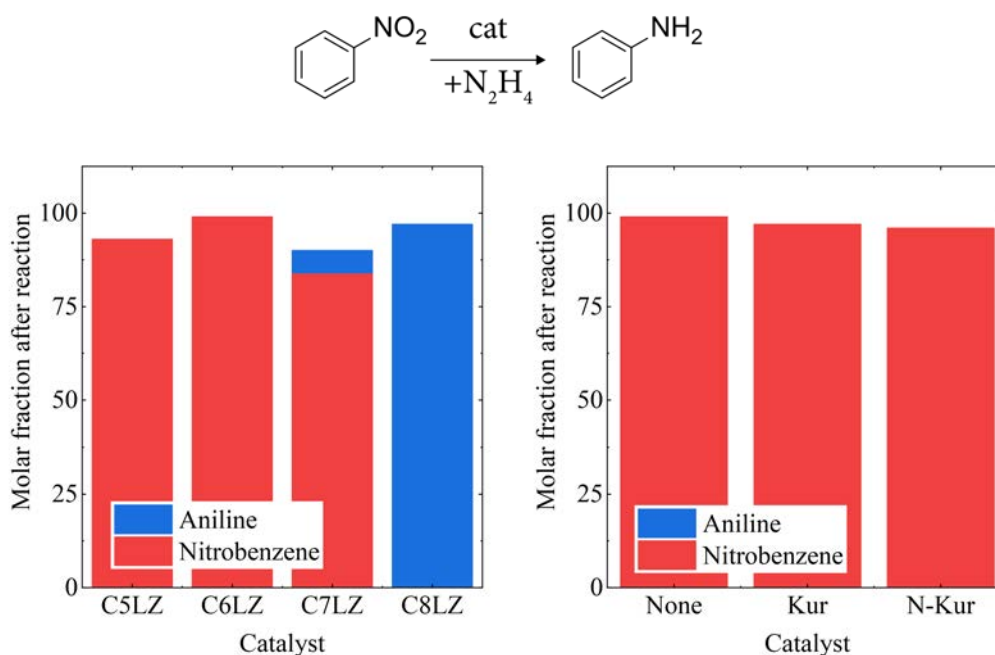


Figure 4.2: Reduction of nitrobenzene to aniline in presence of hydrazine and a catalyst and catalytic performances of different catalysts.

It is not intuitive to predict the properties of a carbonaceous material while its doping content increases. In particular, the nitrogen content has an upper limit above which the material is not catalytic active anymore for the reduction of nitrobenzene. Since the reduction process involves the movement of electrons, the nitrogen upper limit might be defined by the doping effect on the conductivity. In agreement with **Chapter 3** and the work of Larsen, higher nitrogen content implies lower conductivity which might hinder the electron transfer from hydrazine to nitrobenzene.

In order to validate this hypothesis, TMB oxidation with hydrogen peroxide was chosen as a control experiment (**Figure 4.3**). This reaction gained high interest in the past years as a model reaction for the peroxidase-like activity of nanozymes.[18–20] For this reason, there is higher knowledge about the catalytic mechanism in presence of a carbocatalyst compared to hydrazine.[21] Indeed, peroxides-mediated oxidation reactions were shown to be catalyzed by electron-poor carbon atoms next to the nitrogen atoms.[22] Moreover, the role of conjugated structures was proven to be critical in agreement with our previous statements.[23]

The oxidized product of TMB is characterized by blue color and it can be tracked through its absorbance at 652 nm in visible spectroscopy (**Figure 4.3**).[24] Hence, the performances are reported as absorbance in function of time (**Figure 4.3**). Similar to the reduction results, the production of TMB_{ox} was not observed for C5LZ and C6LZ, while a moderate product amount was observed with the use of C7LZ. The highest absorbance at 652 nm was observed for C8LZ indicating its better catalytic properties compared to the other materials.

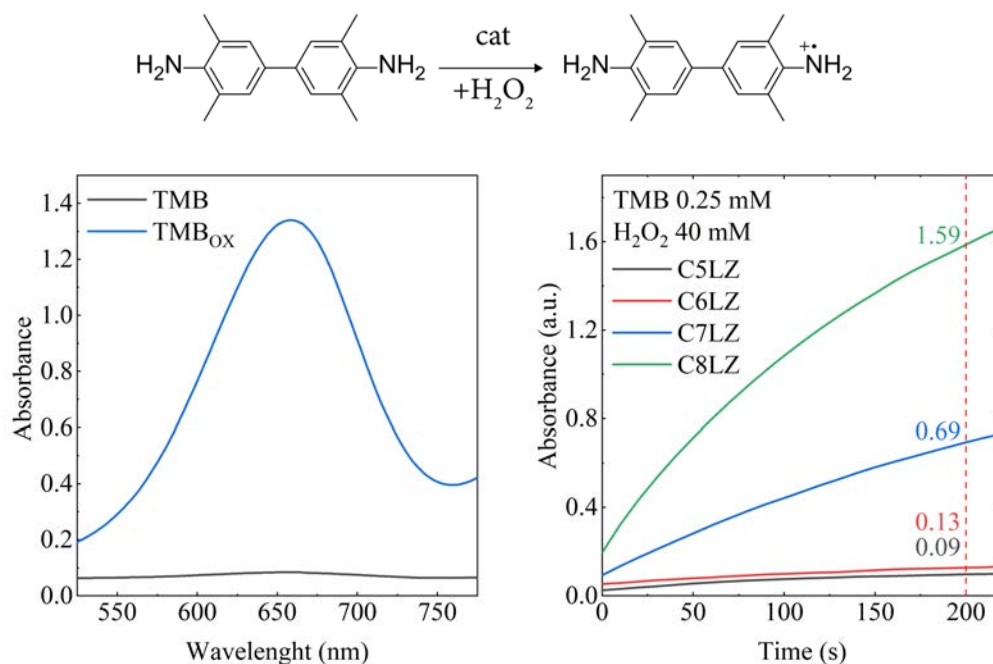


Figure 4.3: Oxidation reaction of TMB in presence of hydrogen peroxide, Visible spectra of TMB and its oxidized product (TMB_{ox}), and kinetic profiles of absorbance at 652 nm for the different catalysts.

The reaction using C8LZ was further analyzed through Michaelis-Menten kinetics (**Figure 4.4**) similarly to other nanozymes reports.[21] The maximum rate at a saturating substrate concentration (v_{\max}) was found to be $0.8 \mu\text{M/s}$. The substrate concentration at which the reaction rate is half of v_{\max} (K_M) was 28.0 mM . A comparison with previously published carbonaceous materials as catalysts for the same transformation shows that C8LZ presents the highest v_{\max} and the second-highest K_M reported to date.[24–26] This indicates the presence of a high number of active sites and it is in line with the high nitrogen content (14 wt%) of the material.

Accordingly with the similarity between results from reduction and oxidation reactions, these redox processes might involve similar mechanisms and active sites. The sites are most likely found on the electron-poor carbon atoms adjacent to the nitrogen as described by previous reports.[22] However, their amount or their strength are likely not the key parameters to promote these reactions. Indeed, C5LZ or C6LZ should presents a higher amount of electron-poor carbon due to the larger nitrogen content, but their activity is kept low. Even though the surface area and pore structure might play a role, it must be pointed out that C6LZ presents already a larger surface area than previously reported nitrogen-doped carbonaceous materials active for the same reaction.[26] Therefore, the effect of nitrogen on conductivity appears critical and hinders further conclusions.

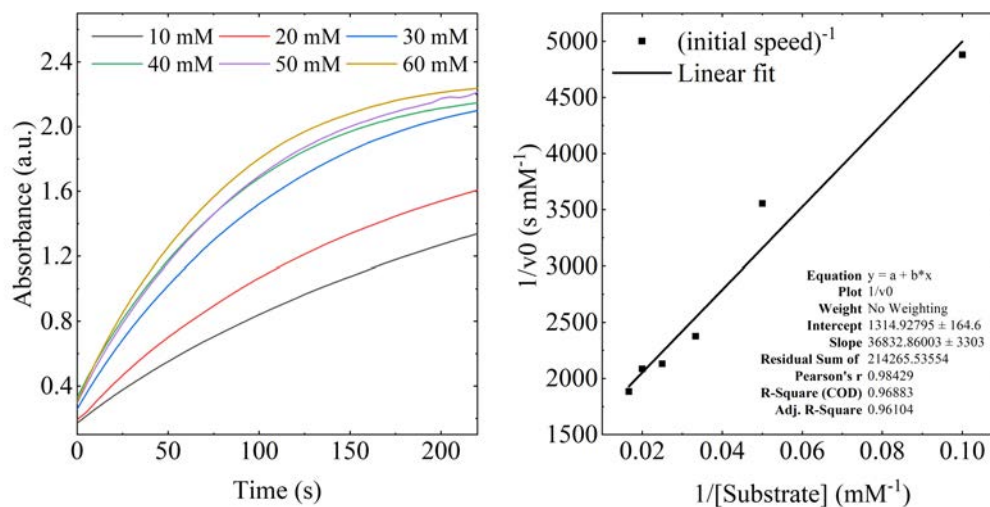


Figure 4.4: Kinetic profiles of C8LZ in presence of different hydrogen peroxide concentrations and linear fitting of the inverse initial speed at given inverse concentration according to Michaelis-Menten analysis.

4.3 Carbonaceous materials for acid-base catalysis

Cyclic carbonates are important molecules which can be used as aprotic solvents, electrolytes in secondary batteries, valuable precursors for polymers, or intermediates in organic synthesis.[27–29] Their production got more attention as the cycloaddition of CO₂ to diverse epoxides is a promising reaction to use the known greenhouse gas as a reagent.[30] Despite its reputation, carbon dioxide is a promising renewable C1 source, but is rarely used due to its chemical inertness.[30] Its cycloaddition process is based the cooperation between acidic and basic centers in order to open the epoxide ring and activate the CO₂ molecule.[31, 32] As described in **Chapter 2**, the prepared materials have high affinity for carbon dioxide. Hence, their use in the production of cyclocarbonates can be a relevant application to produce valuable products and study the acid-base nature of the materials.

A model synthesis of cyclocarbonates was performed from epichlorohydrin at 130 °C in presence of CO₂ (5 Bar). The product formation was followed by ¹H-NMR in presence of an internal standard and the results are reported in **Figure 4.5**. C6LZ is the material which gave the highest conversion of epichlorohydrin (58%) with a moderate selectivity towards the desired product (61%). No side-products were detected using ¹H-NMR analysis, suggesting that polymerization reactions might be responsible for the low selectivity.[28] C7LZ showed less conversion (36%) and low selectivity, while C8LZ catalysis gave the highest selectivity (95%), but a lower conversion (27%). On the other hand, no product formation could be observed from the catalysis with C5LZ.

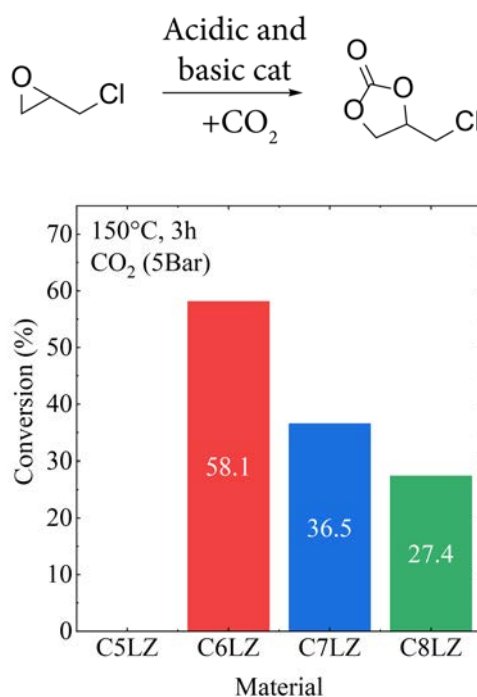


Figure 4.5: CO₂ cycloaddition reaction to epichlorohydrine and catalytic conversions reported against different materials.

As introduced previously, the cycloaddition reaction is fostered by an acidic and a basic site. In order to ensure the presence of these, many reports use the addition of a co-catalyst such as tertammonium bromide, which can act as nucleophile.[32] The ability of C6LZ in catalyzing the reaction without further co-cocatalyst might imply the presence of higher amount of basic sites, which can act similar to the bromide. Yet, the difference in the selectivity are not clear and further studies are needed.

For an in depth analysis, we studied the acid-catalyzed hydrolysis of (dimethoxymethyl)benzene (DMB) to benzaldehyde (BA) followed by a base-mediated Knoevenagel condensation that yields benzomalononitrile (BMN).[33] The two-step one-pot reaction (**Figure 4.6**) was monitored by $^1\text{H-NMR}$ analysis. The results are reported in **Figure 4.6**, which shows that all the materials presented good activity towards both reactions. C8LZ and C7LZ gave 100% conversion of DMB after 4 h, while C6LZ shows the highest conversion to BMN (80%) after the same time.

In order to obtain a better comparison, **Figure 4.7** summarizes the conversions from the acidic and the basic catalysis. The findings show that C8LZ is a better Lewis acid (80% DMB conversion) than C7LZ (65% DMB conversion) and C6LZ (53% DMB conversion). On the other hand, C6LZ is a better Lewis base (51% BA conversion) than C7LZ (38% BA conversion) and C8LZ (32% BA conversion). C5LZ shows good activity in the Lewis acid catalysis (58% DMB conversion), but performs poorly as Lewis base (29% BA conversion). While the low conversion from basic catalysis from C5LZ might be influenced by the low specific surface area, the acid-

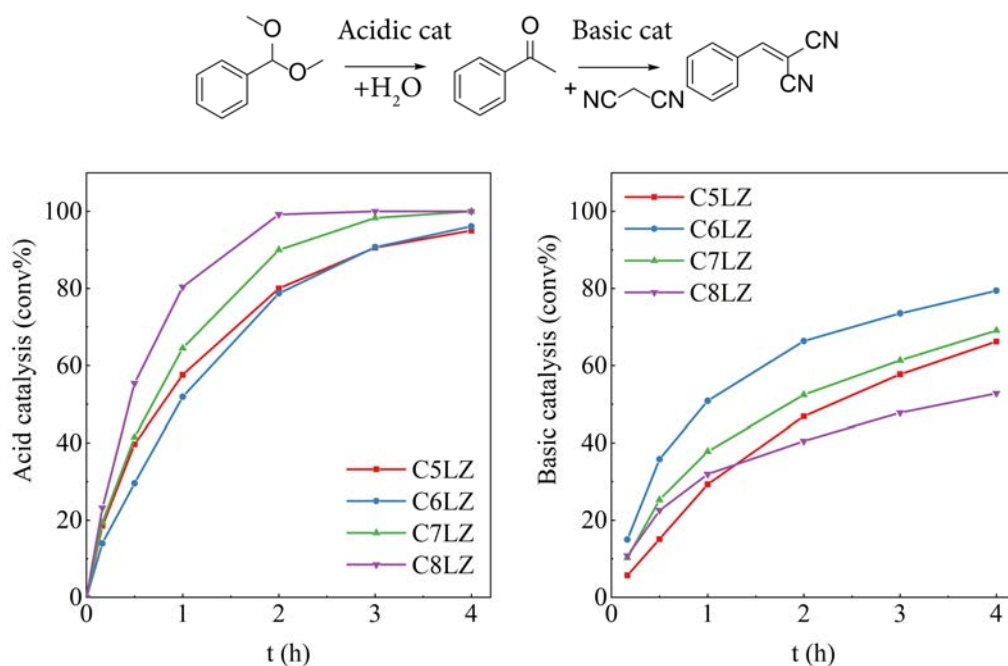


Figure 4.6: acid-catalyzed hydrolysis of (dimethoxymethyl)benzene (DMB) to benzaldehyde (BA) followed by a base-mediated Knoevenagel condensation that yields benzomalononitrile (BMN) and relative kinetic of conversions of the reagents for different materials

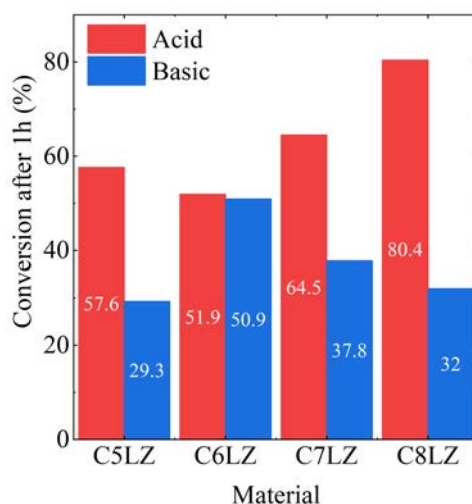


Figure 4.7: Graphical representation as columns of the conversions at 1h for acidic (red) and basic (blue) catalysis for the different materials.

base trends observed from C6LZ, C7LZ, and C8LZ correlates to the nitrogen content of the materials, suggesting the role of the doping in the acid-base nature of the materials.

4.4 Catalytic influence of nitrogen speciation

X-ray photoelectron spectroscopy (XPS) is a powerful tool to observe the change in the oxidation state of atoms on the surface of a material.[34] Hence, this technique was used to characterize the surface functionalities of the materials used as catalysts in the previous sections. The aim of this analysis is to connect and rationalize the catalytic results accumulated in this chapter by understanding of the oxidation state of the atoms that might be involved in the catalysis.

Figure 4.8 reports the C1s and N1s XPS regions measured for C5LZ, C6LZ, C7LZ and C8LZ. C1s XPS region was deconvoluted by three Gaussian functions centered at 284 eV, 286 eV and 288 eV. While many reports define the kind of atom bound to the carbon through the binding energy of the Gaussian function, only the C-C related signal will be clearly specified as the one at 284 eV. On the other hand, 286 eV and 288 eV will be described as carbon atoms bound to one or more heteroatom.[35] Similar approach will be used for N1s region deconvolution, which was performed by four Gaussian functions centered at 398 eV, 400 eV, 401 eV and 402 eV. These functions will be described based on the oxidation state (low for 398 eV and 400 eV, high for 401 eV and 402 eV) of nitrogen atoms instead of the functionality type (e.g. pyridinic, pyrrolic or quaternary).[36] The change in nomenclature described is driven by the amorphous nature of the materials combined to the high level of nitrogen doping, which do not assure that pure pyridinic or pyrrolic cycles can be found in the structure.

The deconvolution percentages obtained from **Figure 4.8** were used to calculate the amount

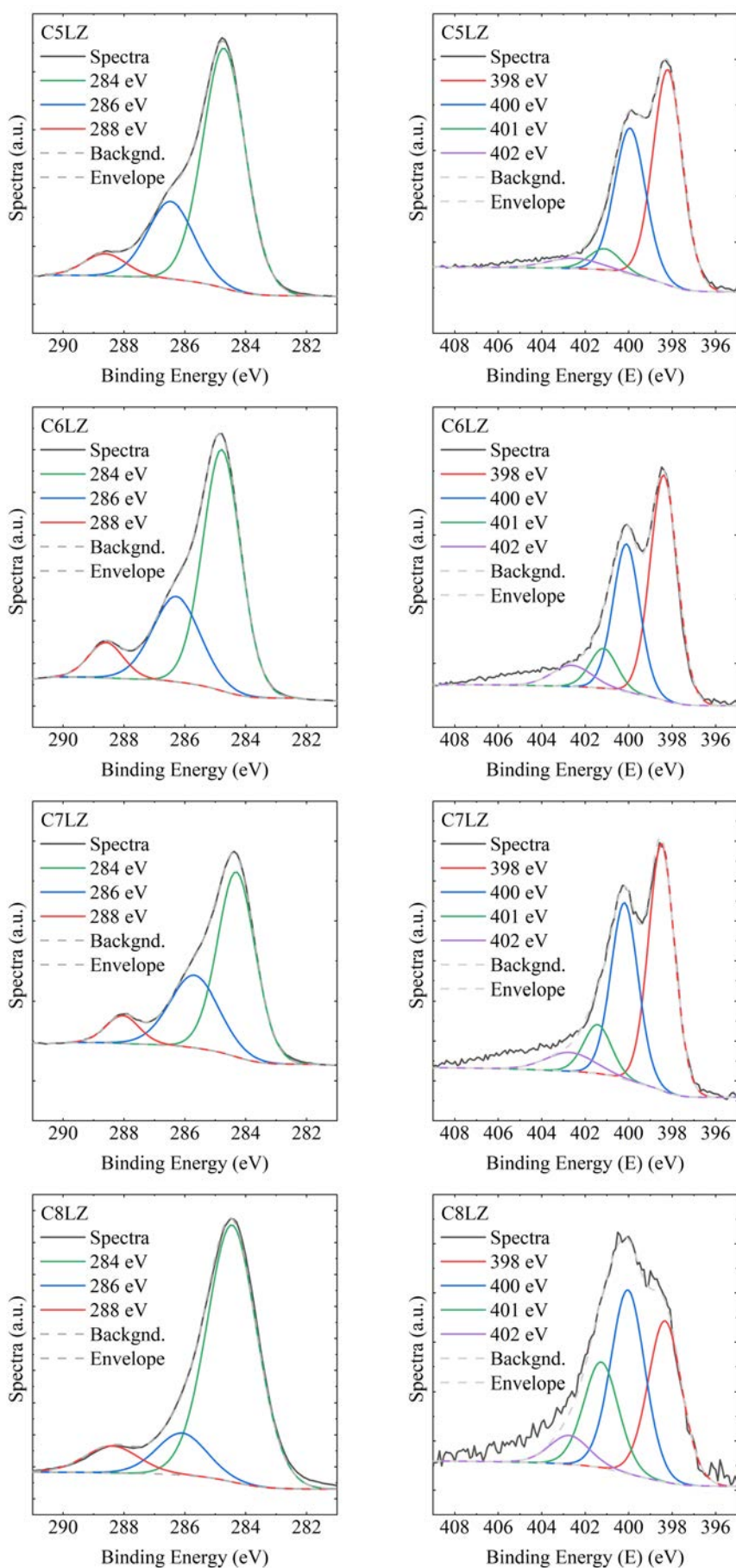


Figure 4.8: C1s (left column) and N1s (right column) XPS regions and relative deconvolution for C5LZ, C6LZ, C7LZ, and C8LZ.

of moles per 100 g for each carbon or nitrogen functionality based on SEM-EDX of the materials (see **Chapter 2**). The results are reported as function of the materials in **Figure 4.9** which shows a noticeable difference between C8LZ and the other materials. While C5LZ, C6LZ, and C7LZ presents higher amount of carbon in higher oxidation state (up to 1.4 mol/100 g), C8LZ is characterized by the higher contribution of carbon atoms at 284 eV. On the other hand, the large nitrogen loss observed for C8LZ in **Chapter 2.4** can be here correlated to the lower stability of low oxidation state nitrogen atoms (i.e. 398 eV and 400 eV). These are unstable and are lost upon heating at 800 °C. Remarkably, high oxidation state nitrogen atoms increase in content between C5LZ and C6LZ, but their amount is quite stable among all the other materials.

The trends described match partially the change in catalytic performances observed in the previous sections. C8LZ shows the highest contribution from 284 eV signal and it has the best performances for redox reactions. This confirms that conductivity and large conjugated domains (284 eV signal) are fundamental to promote redox reactions. Moreover, the loss in basic activity observed in **Figure 4.7** from C6LZ to C8LZ correlates with the loss of 398 eV and 400 eV nitrogen species. These are electron rich (low oxidation state) nitrogen atoms and they are the main basic sites of the materials. This match the change in chemical compositions observed in **Chapter 2.4**.

On the other hand, the acidic sites are less trivial to be assigned. Electron poor carbon atoms (i.e. 286 eV and 288 eV) were previously described as possible acidic sites, but they gave the lowest contribution for C8LZ (best performing acid catalysts). This might be related to the loss in electron rich nitrogen atom that effects dramatically the carbon functionalities. In particular, 286 eV carbon atoms might be bound 398 eV or 400 eV nitrogen atoms and they are lost upon higher synthetic temperature (i.e. 800 °C) while 288 eV carbon atoms might

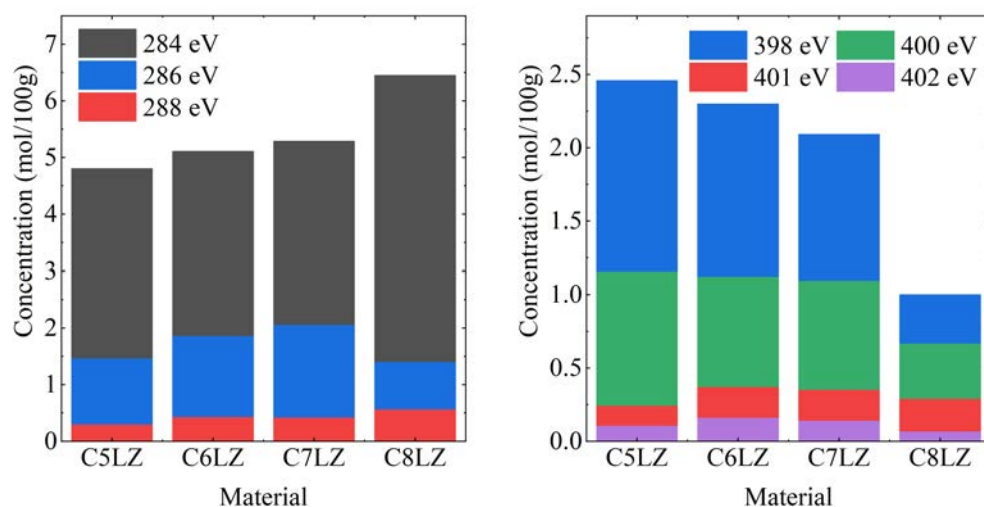


Figure 4.9: Staked bar plot representing moles per 100 g of C1s and N1s species calculated from XPS deconvolution and SEM-EDX composition.

be bound to 401 eV and 402 eV nitrogen atoms and preserved during the heating process. Accordingly to the acid catalysis results, 288 eV are probably involved in the acid catalysis because of their increasing contribution from C5LZ to C8LZ.

In order to have a better characterization of the acidic sites, temperature programmed desorption of ammonia was used. **Figure 4.10** reports the results of this analysis as TCD signal in function of temperature of the materials. The TCD signal measures the ammonia desorbed from the surface upon heating the materials. The desorption temperature gives useful information on the strength of the acidic sites. From C5LZ to C7LZ, the desorption band became gradually sharper, more intense and the desorption maximum shifted to lower temperatures. On the other hand, C8LZ had a desorption band with low intensity from 100 °C to 250 °C. The intensity of the signals is related to the amount of gas desorbed, which is connected to the amount of acid sites. Hence, the similarity between C1s XPS deconvolution and intensity of the TPD signal suggests the connection between acid sites and low oxidation state carbon atoms at 286 eV and 288 eV.

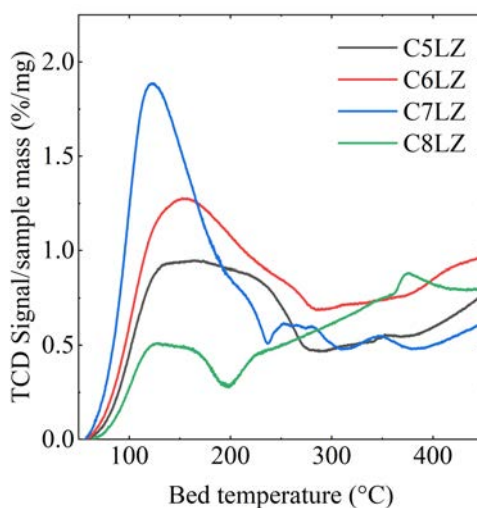


Figure 4.10: Ammonia temperature programmed desorption (TPD) plotted as TCD signal versus bed temperature.

Bibliography

- [1] Stenhouse, J. *Chem. Gaz.* **13** (1854).
- [2] Antonietti, M., Lopez-Salas, N. & Primo, A. Adjusting the structure and electronic properties of carbons for metal-free carbocatalysis of organic transformations. *Advanced Materials* **31**, 1805719 (2019).
- [3] Su, D. S., Perathoner, S. & Centi, G. Nanocarbons for the development of advanced catalysts. *Chemical Reviews* **113**, 5782–5816 (2013).
- [4] Su, D. S., Wen, G., Wu, S., Peng, F. & Schlögl, R. Carbocatalysis in liquid-phase reactions. *Angewandte Chemie International Edition* **56**, 936–964 (2017).
- [5] Navalon, S., Dhakshinamoorthy, A., Alvaro, M. & Garcia, H. Carbocatalysis by graphene-based materials. *Chemical Reviews* **114**, 6179–6212 (2014).
- [6] Tang, P., Hu, G., Li, M. & Ma, D. Graphene-based metal-free catalysts for catalytic reactions in the liquid phase. *ACS Catalysis* **6**, 6948–6958 (2016).
- [7] Rosso, C., Filippini, G. & Prato, M. Carbon dots as nano-organocatalysts for synthetic applications. *ACS Catalysis* **10**, 8090–8105 (2020).
- [8] Albero, J. & Garcia, H. Doped graphenes in catalysis. *Journal of Molecular Catalysis A: Chemical* **408**, 296–309 (2015).
- [9] Duan, X., O'Donnell, K., Sun, H., Wang, Y. & Wang, S. Sulfur and nitrogen co-doped graphene for metal-free catalytic oxidation reactions. *Small* **11**, 3036–3044 (2015).
- [10] Sun, X., Li, B., Liu, T., Song, J. & Su, D. S. Designing graphene as a new frustrated lewis pair catalyst for hydrogen activation by co-doping. *Physical Chemistry Chemical Physics* **18**, 11120–11124 (2016).
- [11] Lepre, E. Catalytic properties of high nitrogen content carbonaceous materials. *Submitted* .
- [12] Zhang, L., Zhou, M., Wang, A. & Zhang, T. Selective hydrogenation over supported metal catalysts: From nanoparticles to single atoms. *Chemical Reviews* **120**, 683–733 (2020).

- [13] Yang, F., Chi, C., Wang, C., Wang, Y. & Li, Y. High graphite n content in nitrogen-doped graphene as an efficient metal-free catalyst for reduction of nitroarenes in water. *Green Chemistry* **18**, 4254–4262 (2016).
- [14] Schirmann, J.-P. & Bourdauducq, P. *Hydrazine* (John Wiley Sons, Ltd, 2001).
- [15] Larsen, J. W., Freund, M., Kim, K. Y., Sidovar, M. & Stuart, J. L. Mechanism of the carbon catalyzed reduction of nitrobenzene by hydrazine. *Carbon* **38**, 655–661 (2000).
- [16] Yang, F., Chi, C., Wang, C., Wang, Y. & Li, Y. High graphite n content in nitrogen-doped graphene as an efficient metal-free catalyst for reduction of nitroarenes in water. *Green Chemistry* **18**, 4254–4262 (2016).
- [17] Li, L., Li, L., Cui, C., Fan, H. & Wang, R. Heteroatom-doped carbon spheres from hierarchical hollow covalent organic framework precursors for metal-free catalysis. *ChemSusChem* **10**, 4921–4926 (2017).
- [18] Gao, L. *et al.* Intrinsic peroxidase-like activity of ferromagnetic nanoparticles. *Nature Nanotechnology* **2**, 577–583 (2007).
- [19] Wu, J. *et al.* Nanomaterials with enzyme-like characteristics (nanozymes): next-generation artificial enzymes (ii). *Chemical Society Reviews* **48**, 1004–1076 (2019).
- [20] Huang, Y., Ren, J. & Qu, X. Nanozymes: Classification, catalytic mechanisms, activity regulation, and applications. *Chemical Reviews* **119**, 4357–4412 (2019).
- [21] Hu, Y. *et al.* Nitrogen-doped carbon nanomaterials as highly active and specific peroxidase mimics. *Chemistry of Materials* **30**, 6431–6439 (2018).
- [22] Gao, Y. *et al.* Nitrogen-doped sp²-hybridized carbon as a superior catalyst for selective oxidation. *Angewandte Chemie International Edition* **52**, 2109–2113 (2013).
- [23] Zhao, R., Zhao, X. & Gao, X. Molecular-level insights into intrinsic peroxidase-like activity of nanocarbon oxides. *Chemistry – A European Journal* **21**, 960–964 (2015).
- [24] Lin, S. *et al.* Nucleobase-mediated synthesis of nitrogen-doped carbon nanozymes as efficient peroxidase mimics. *Dalton Transactions* **48**, 1993–1999 (2019).
- [25] Song, Y., Qu, K., Zhao, C., Ren, J. & Qu, X. Graphene oxide: Intrinsic peroxidase catalytic activity and its application to glucose detection. *Advanced Materials* **22**, 2206–2210 (2010).
- [26] Fan, K. *et al.* In vivo guiding nitrogen-doped carbon nanozyme for tumor catalytic therapy. *Nature Communications* **9**, 1440 (2018).
- [27] Xu, W. *et al.* Lithium metal anodes for rechargeable batteries. *Energy & Environmental*

- Science* **7**, 513–537 (2014).
- [28] Webster, D. C. Cyclic carbonate functional polymers and their applications. *Progress in Organic Coatings* **47**, 77–86 (2003).
- [29] Sakakura, T., Choi, J.-C. & Yasuda, H. Transformation of carbon dioxide. *Chemical Reviews* **107**, 2365–2387 (2007).
- [30] Sakakura, T. & Kohno, K. The synthesis of organic carbonates from carbon dioxide. *Chemical Communications* 1312–1330 (2009).
- [31] Dai, W.-L., Luo, S.-L., Yin, S.-F. & Au, C.-T. The direct transformation of carbon dioxide to organic carbonates over heterogeneous catalysts. *Applied Catalysis A: General* **366**, 2–12 (2009).
- [32] Shaikh, R. R., Pornpraprom, S. & D’Elia, V. Catalytic strategies for the cycloaddition of pure, diluted, and waste CO₂ to epoxides under ambient conditions. *ACS Catalysis* **8**, 419–450 (2018).
- [33] Gianotti, E., Diaz, U., Veltz, A. & Corma, A. Designing bifunctional acid–base mesoporous hybrid catalysts for cascade reactions. *Catalysis Science & Technology* **3**, 2677–2688 (2013).
- [34] Chu, P. K. & Li, L. Characterization of amorphous and nanocrystalline carbon films. *Materials Chemistry and Physics* **96**, 253–277 (2006).
- [35] Susi, T., Pichler, T. & Ayala, P. X-ray photoelectron spectroscopy of graphitic carbon nanomaterials doped with heteroatoms. *Beilstein Journal of Nanotechnology* **6**, 177–192 (2015).
- [36] Pels, J., Kapteijn, F., Moulijn, J., Zhu, Q. & Thomas, K. Evolution of nitrogen functionalities in carbonaceous materials during pyrolysis. *Carbon* **33**, 1641–1653 (1995).

Chapter 5

Unconventional selectivity of Ni-decorated carbonaceous materials

5.1 Nickel for single-atom materials

Nickel has played a central role in heterogeneous catalysis since the twentieth century. For example, modern chemisorption theories originated from Paul Sabatier's hypothesis of Ni perhydride formation on the surface of metallic nickel during hydrogenation reactions.[1] Since this vanguard work - worth the Nobel prize in 1912 -, nickel-based catalysts made great progress for hydrogen transfer reaction as reviewed by Alonso et al. one century after.[2] More recently, this metal attracted the attention of the community as a homogeneous catalyst for cross-coupling reactions and as a single-atom catalyst for carbon dioxide reduction reaction.[3, 4] This chapter will focus on this second application.

As described in **Chapter 1**, single-atoms materials are promising candidates to overcome different heterogeneous catalysis drawbacks (e.g. low atom efficiency, not clear active sites, etc.). Among the different metals, nickel stood out in recent years for the high Faradaic efficiency in the electrochemical reduction of carbon dioxide to carbon monoxide (**Figure 5.1**). This selectivity has been observed for nickel atoms supported on nitrogen-doped nanocarbons which stabilizes the metal through a nitrogen-rich coordination environment up to 20 wt% in loading.[5, 6] Nevertheless, mainly nitrogen coordination environments have been investigated for CO₂RR while other coordination environments are overlooked. By comparing with oxygen reduction reaction (ORR) results, it was shown that oxygen coordinated Ni single atoms can show different selectivity compared to nitrogen ones.[7, 8] Hence, it is important to investigate different coordination environments for CO₂RR to promote the reduction of carbon dioxide to a more valuable products than CO.

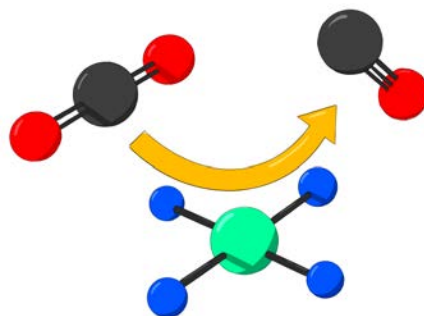


Figure 5.1: Graphical representation of a nitrogen coordinated nickel single atom involved in the CO₂RR.

The materials introduced in **Chapter 2** are optimal candidates to support single-atom dispersion due to their high specific surface area and high heteroatom content. Furthermore, their high resistance in oxidative environments - described in **Chapter 3** - allows the investigation of novel synthetic paths not applicable to conventional materials. Hence, the materials proposed in this thesis can be used as supports to develop Ni single atoms aiming to different coordination environments.

5.2 Nickel decorated materials

In order to synthesize Ni single-atoms materials, a simple impregnation-decomposition method was used starting from C8NZ and Ni acetylacetonate ($\text{Ni}(\text{acac})_2$) (**Figure 5.2**). In particular, the metal complex was chosen due to its oxygen coordination of Ni to tune the final coordination environment on the material. On the other hand, C8NZ was chosen as model support of the materials synthesized in **Chapter 2**.

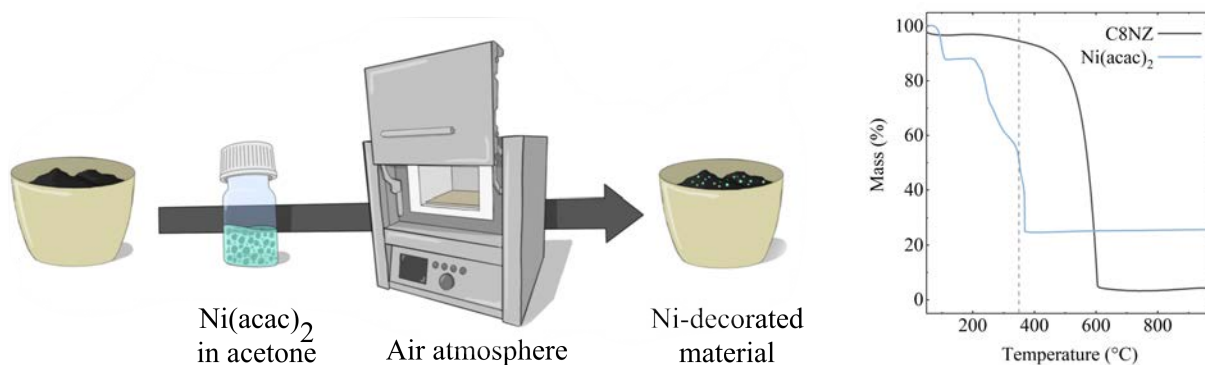


Figure 5.2: (left) Graphic representation of the synthesis of Ni-decorated materials and (right) thermogravimetric analysis in air (10 K min^{-1}) of the support material and the nickel precursor.

The synthesis involves a first impregnation step in acetone during which $\text{Ni}(\text{acac})_2$ is deposited on the material surface. Upon drying the solvent, a solid mixture is obtained and it is submitted to a heat treatment at 350° in air. At this temperature, the support remains stable while the nickel complex decomposes as seen by TGA in **Figure 5.2**. By changing the initial mass of $\text{Ni}(\text{acac})_2$ it is possible to obtain different nickel loadings. The materials will be named hereafter as " $x\text{Ni@C8NZ}$ ", where x is the Ni ideal loading expected based on the initial $\text{Ni}(\text{acac})_2$ mass used (**Table 5.1**).

Table 5.1: Summary of the material synthesized, codes and yields.

Support	Ideal Ni loading wt%	T synthesis °C	Yield %	Code
C8NZ	2	350	79	2Ni@C8NZ
	6		82	6Ni@C8NZ
	10		80	10Ni@C8NZ
	14		31	14Ni@C8NZ

At first, the elemental composition of the samples was analyzed by SEM-EDX analysis and ICP-EOS. The results are reported in **Figure 5.3** and **table 5.2**. The ideal nickel loading is confirmed in almost all the materials out of 14Ni@C8NZ, which has double the amount of nickel expected (i.e. 30 wt% vs 14 wt%). Moreover, the support composition changes significantly - carbon and nitrogen weight percentages decrease and oxygen content increases - when the nickel content reaches higher loading than 10 wt%. Both observations might be related to a material

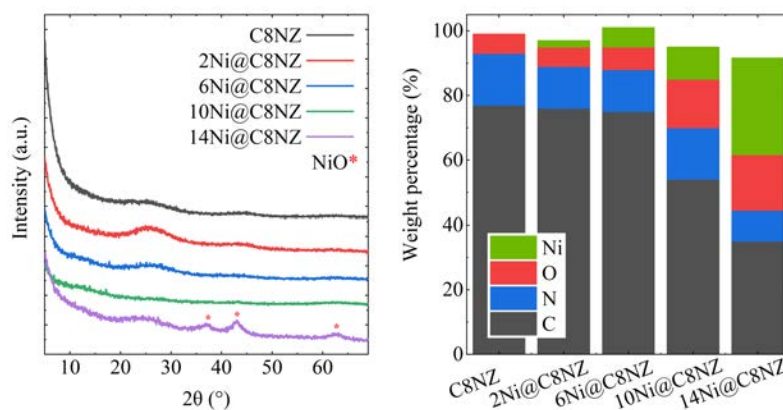


Figure 5.3: (from left to right) X-ray diffraction patterns and elemental composition from SEM-EDX of the pristine support and the Ni-decorated materials.

Table 5.2: Composition summary of the pristine support and the Ni decorated materials.

Material	SEM-EDX					ICP-EOS	C/N atomic
	wt%					wt%	
	C	N	O	Zn	Ni	Ni	
C8NZ	74	18	6	0.5	-	-	4.5
2Ni@C8NZ	79	13	6	0.6	2	2	7.0
6Ni@C8NZ	75	13	7	0.5	7	4	6.9
10Ni@C8NZ	54	16	15	0.9	12	11	3.9
14Ni@C8NZ	35	9.4	17	2.9	30	33	4.5

decomposition promoted by nickel which is in agreement with the changes in the final materials yields (**Table 5.1**). On the other hand, 2Ni@C8NZ and 6Ni@C8NZ compositions indicate that low nickel loading affects the material composition less than high nickel loading. Indeed, carbon and oxygen content remain approximately constant while nitrogen content partially decrease from 18.6 wt% to 13 wt% leading to higher C/N ratio (see **Table 5.2**).

The Ni-decorated materials were analyzed by XRD and only 14Ni@C8NZ presents clear diffraction peaks at 37°, 43°, and 63° characteristic of a NiO phase (**Figure 5.3**). This suggests that the low yield reported for 14Ni@C8NZ in **Table 5.1** might be related to the NiO phase, which promotes the decomposition of the support. On the contrary, 2Ni@C8NZ, 6Ni@C8NZ, and 10Ni@C8NZ XRD patterns do not have any peaks related to Ni, NiO, or NiOH suggesting the presence of Ni single atoms or particles smaller than 2 nm. Moreover, the graphitic stacking remains broad and weak for these materials suggesting that, even though it might promote the decomposition of the structure, nickel does not promote graphitization in these materials.

Gas adsorption was used to analyze the specific surface area and pore volume of the different samples. Nitrogen isotherms at 77 K and carbon dioxide isotherms at 273K were measured and the results are reported in **Figure 5.4** and **Table 5.3**. The gas adsorption analysis follows a similar trend to elemental composition. While low nickel loading does not affect significantly the surface area calculated using BET theory (i.e., 1834 m² g⁻¹, 1771 m² g⁻¹, and 1843 m²

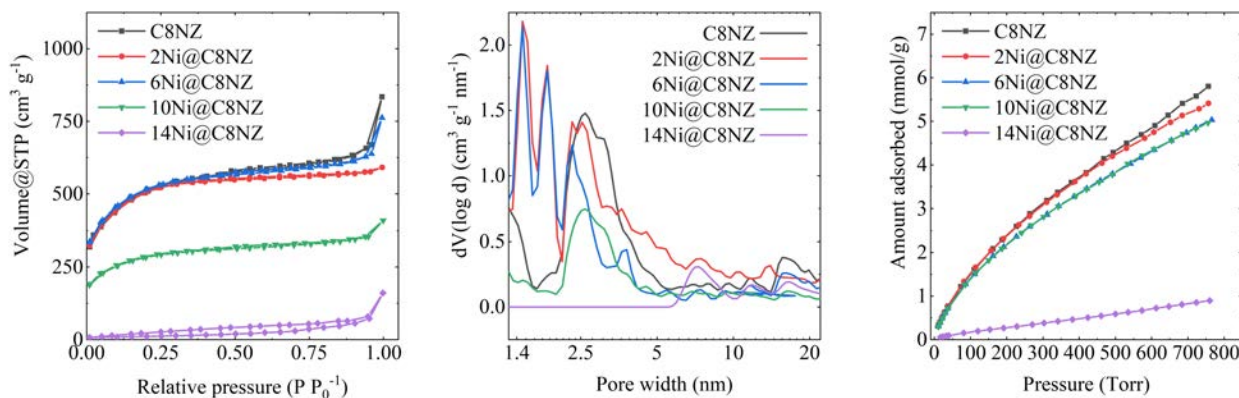


Figure 5.4: (From left to right) N₂ isotherms at 77K, DFT calculated pore size distribution, and CO₂ adsorption isotherm at 273K of the pristine support and the Ni decorated materials.

Table 5.3: Gas adsorption data obtained from BET and DFT calculations applied on N₂ and CO₂ isotherms at 77K and 273K.

Material	Specific surface area m ² g ⁻¹	Total pore volume (<40 nm) cm ³ g ⁻¹	Total pore volume (<10 nm) cm ³ g ⁻¹
C8NZ	1834	2.1	0.23
2Ni@C8NZ	1771	1.16	0.22
6Ni@C8NZ	1843	0.99	0.20
10Ni@C8NZ	1017	0.55	0.20
14Ni@C8NZ	40	0.11	0.03

g⁻¹ for C8NZ, 2Ni@C8NZ, and 6Ni@C8NZ, respectively), high nickel loading are characterized by lower specific surface area values (i.e. 1017 m²g⁻¹ and 40 m² g⁻¹ for 10Ni@C8NZ and 14Ni@C8NZ respectively). 10Ni@C8NZ isotherm maintains the C8NZ shape - type I, typical of microporous materials as discussed in **Chapter 2** - with lower volume adsorbed compared to the pristine support. 14Ni@C8NZ loses completely the initial shape due to a very low value of specific surface area measurable with nitrogen adsorption. Pore size distribution was calculated from N₂ adsorption branches with slit/cylindrical pore NLDFT model, highlighting the presence of 2.5 nm pores characteristic for C8NZ. CO₂ adsorption isotherms at 273 K shows that all the material has similar carbon dioxide adsorption out of 14Ni@C8NZ. This can be further appreciated by the total pore volume calculated from CO₂ isotherms and reported in **Table 5.3**. C8NZ, 2Ni@C8NZ, 6Ni@C8NZ, and 10Ni@C8NZ adsorbed approximately 0.20 cm³ g⁻¹ of CO₂ at 750 Torr. On the other hand, 14Ni@C8NZ adsorbed 0.03 cm³ g⁻¹ of CO₂ at the same pressure, confirming the collapse of its porous structure.

X-ray photoemission spectroscopy (XPS) was used to characterize the different oxidation states for carbon, nitrogen, and nickel atoms (**Figure 5.5**). High-resolution C1s XPS of xNi@C8NZ did not evidence significant changes among the samples. The signal was deconvoluted with Gaussian function centered at 248.6 eV, 285.9 eV, 287.8 eV, and 290.4 eV representing C=C, C-N, C=O, and -C=O bonds, respectively. Noteworthy, C-Ni bonds corresponding to Ni_{1-x}C_x

were not found at 283.4 as reported in the literature.[9]

Similar to C1s XPS, no significant differences were found in the deconvolution of N1s XPS. This was performed by different Gaussian functions corresponding to pyridinic-N (397.9 eV), pyrrolic-N (399.6 eV), and quaternary-N (401.3 eV), oxide-N (403.4eV), and the pi-pi* satellite peak (405.6 eV). Even though the metal-N component could overlap with the pyrrolic-N component, no dramatic change was observed for the pyrrolic-N signal upon Ni content increase. This might suggest that there is not a strong interaction between Ni and N.

Contrary to C1s and N1s spectra, the high-resolution XPS Ni2p_{2/3} spectra display more differences among the samples in the analysis. At first, all the spectra are characterized by the main peak and a corresponding satellite which can be both deconvoluted into two components. These components vary in contribution and positions with the nickel content. Nevertheless, the typical component from metallic nickel centered at 852.6 eV has not been detected confirming the absence of a Ni(0) phase.[10] 2Ni@C8NZ main peak has been deconvoluted by two components at 854.8 eV and 856.1 eV corresponding to tetra carbonyl complexes-like coordination and Ni acetylacetonate complexes, respectively.[11, 12] A shift to the higher binding energy of the individual components has been observed with the increase of the nickel content in 6Ni@C8NZ and 10Ni@C8NZ (i.e. 855.3 eV and 857.1 eV). These higher binding energies might be attributed to Ni in a higher valence state (e.g. Ni(III)) or the formation of Ni(II) nanoclusters.[13, 14] Additionally, the contribution of the second component decreases with the nickel loading as observed in **Figure 5.5**. Finally, 14Ni@C8NZ gave a significantly different Ni2p_{2/3} XPS spectrum compared to the other materials. The deconvolution was performed with two components at 855.8 and 853.9 eV attributed to Ni(OH) and NiO, respectively. This agrees with XRD analysis confirming the presence of a significant amount of NiO nanoparticles in this sample.

Electron microscopy imaging was used to characterize the material's morphology (**Figure 5.6**). SEM images show that the colloidal structure of C8NZ was preserved after nickel decoration and only partial shrinking is appreciable in xNi@C8NZ samples. On the other hand, TEM imaging confirms the absence of nanoparticles in 2Ni@C8NZ, 6Ni@C8NZ, and 10Ni@C8NZ. Accordingly, the 14Ni@C8NZ TEM picture shows nanoparticles of 5.1 nm diameter as expected from XRD patterns.

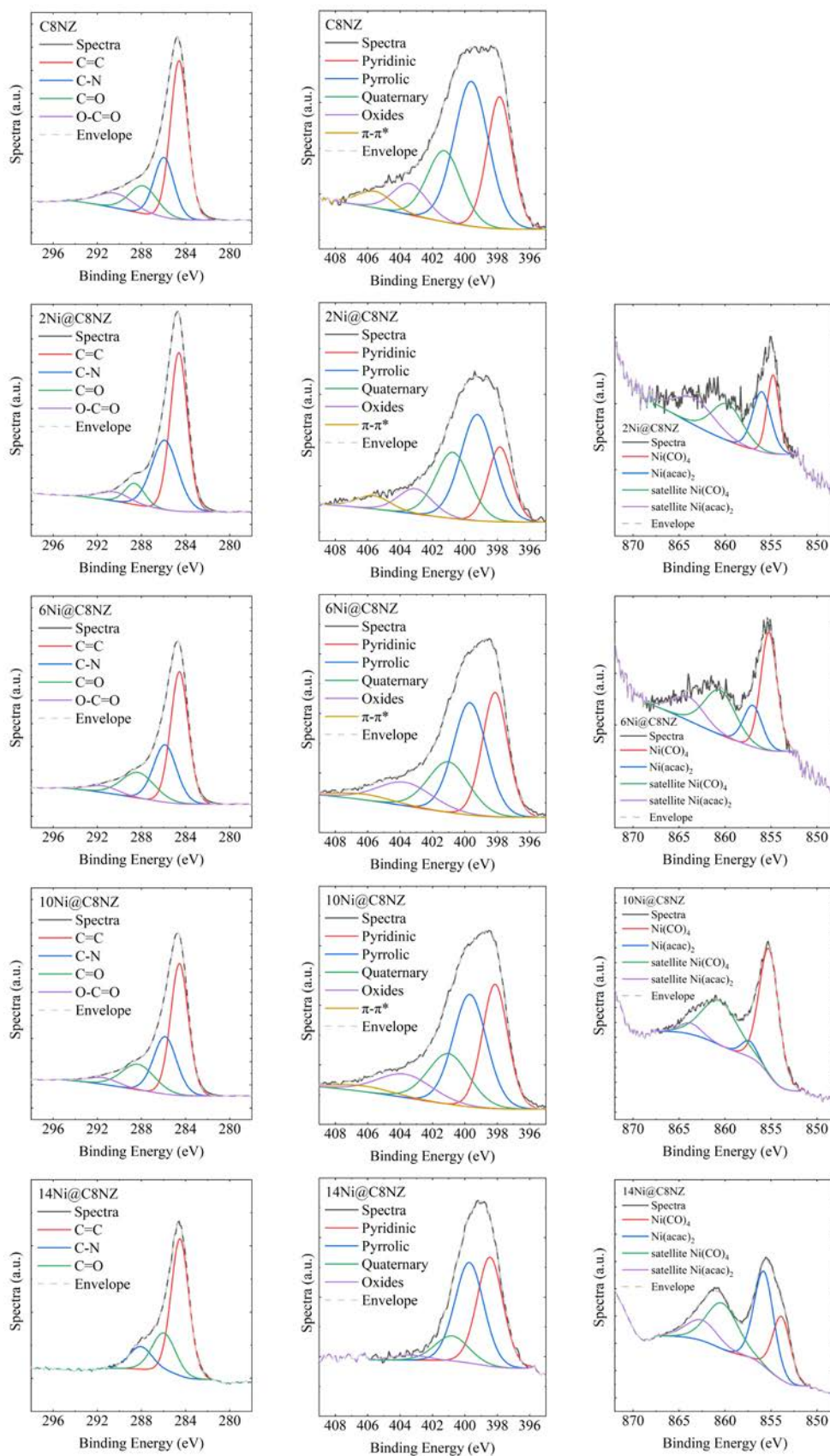


Figure 5.5: C1s (left column), N1s (center column), and Ni2p (right column) XPS spectra of the pristine support and the Ni decorated materials.

Finally, bright field and dark field STEM images of 2Ni@C8NZ, 6Ni@C8NZ, and 10Ni@C8NZ were used to investigate the material morphology and the nickel dispersion at higher magnification (**Figure 5.7**). First, bright field images - more sensitive to diffraction contrast [15] - show the presence of not well stacked and disordered layers in agreement with XRD patterns. Second, dark field images - more sensitive to atomic number contrast [15] - display the presence of numerous white spots with average diameter of 0.25 nm and increasing site density (i.e. 1.40 nm⁻², 2.09 nm⁻², and 2.55 nm⁻² for 2Ni@C8LZ, 6Ni@C8LZ, and 10Ni@C8LZ, respectively). The higher site brightness compared to the support implies that the sites are characterized by higher atomic number and corresponds to nickel sites as single atoms or small nanoclusters.

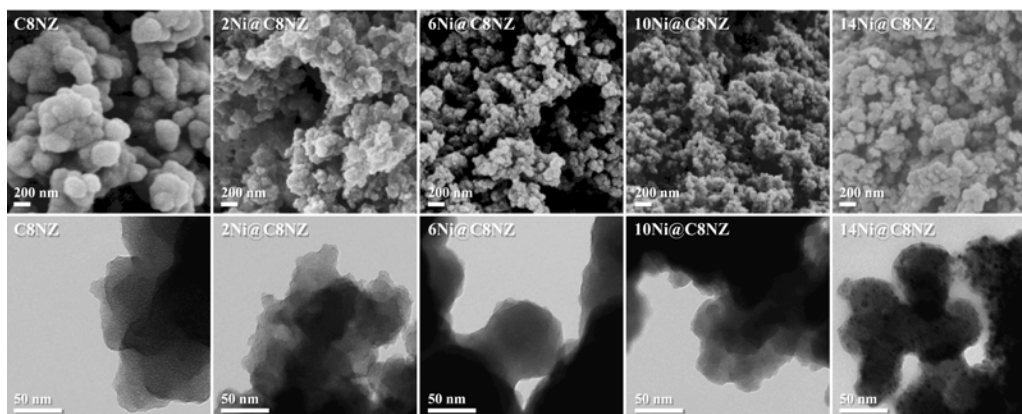


Figure 5.6: Scanning electron microscopy (first row) and Scanning transmission electron microscopy (second row) of the pristine support and the Ni decorated materials.

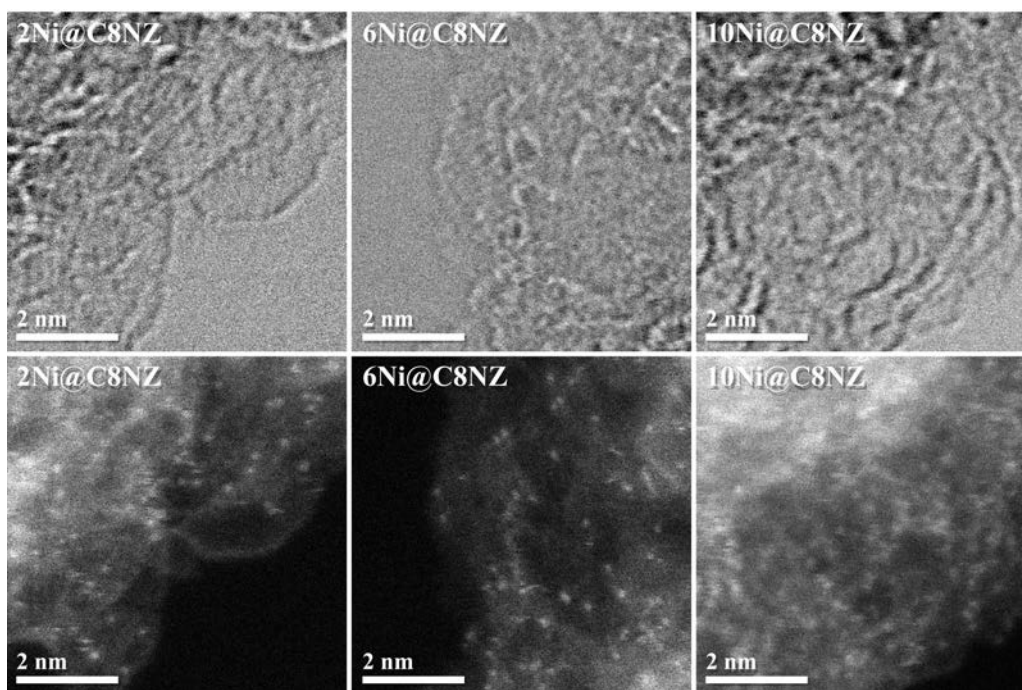


Figure 5.7: Bright field (first row) and high angle annular dark field (second row) scanning transmission electron microscopy images of (from left to right) 2Ni@C8NZ, 6Ni@C8NZ, and 10Ni@C8NZ.

5.3 Local structure of nickel atoms

A simple impregnation-decomposition method was used in the previous section to synthesize a set of Ni-decorated materials. XRD, TEM, and dark-field HAAR-STEM suggested the absence of aggregation into nanoparticles. Nevertheless, it is not possible to discriminate the presence of either isolated single-atoms or small clusters of atoms. Hence, the local structure of the Ni centers of 2Ni@C8NZ, 6Ni@C8NZ, 10Ni@C8NZ, and 14Ni@C8NZ were studied by Ni K-edge X-ray absorption near edge structure (XANES) and extended X-ray absorption fine structure (EXAFS).[16]

Figure 5.8 shows Ni K-edge XANES spectra for 2Ni@C8NZ, 6Ni@C8NZ, 10Ni@C8NZ, and 14Ni@C8NZ along with the reference spectra of bulk metal Ni, NiO, and Ni acetylacetonate ($\text{Ni}(\text{acac})_2$). The absorption edge energies of metallic nickel (i.e. 8333.0 eV) and NiO (i.e. 8340.5 eV) references are lower than that of the samples and $\text{Ni}(\text{acac})_2$ (i.e. 8350. eV). Similar Ni K-edge absorption energies and shapes were observed from nickel acetylacetonate and xNi@C8NZ . This is the first indication that nickel centers share a similar average coordination environment in the materials and the precursor.

Nevertheless, the sample thickness, the presence of mixed-valence Ni compounds, or a phase transition - from fcc to hcp with growing cluster size - might affect the intensity and the position of the Ni K-edge.[17, 18] Hence, XANES spectra of 2Ni@C8NZ, 6Ni@C8NZ, 10Ni@C8NZ, and 14Ni@C8NZ were analyzed by linear combination fitting (LCF) of $\text{Ni}(\text{acac})_2$, NiO, and $\text{Ni}^{(0)}$. The results are reported in **Figure 5.8** and point to a progressive change of $\text{Ni}(\text{acac})_2$ and NiO components in the Ni-decorated samples with the growing content of initial $\text{Ni}(\text{acac})_2$. The number of isolated oxygen coordinated Ni is 99.9% in 2Ni@C8NZ without a significant percentage of neither NiO nor $\text{Ni}^{(0)}$ detected. This percentage decreases to 95% and 90% for 6Ni@C8NZ and 10Ni@C8NZ. 14Ni@C8NZ can be reproduced by 76.8% of isolated oxygen

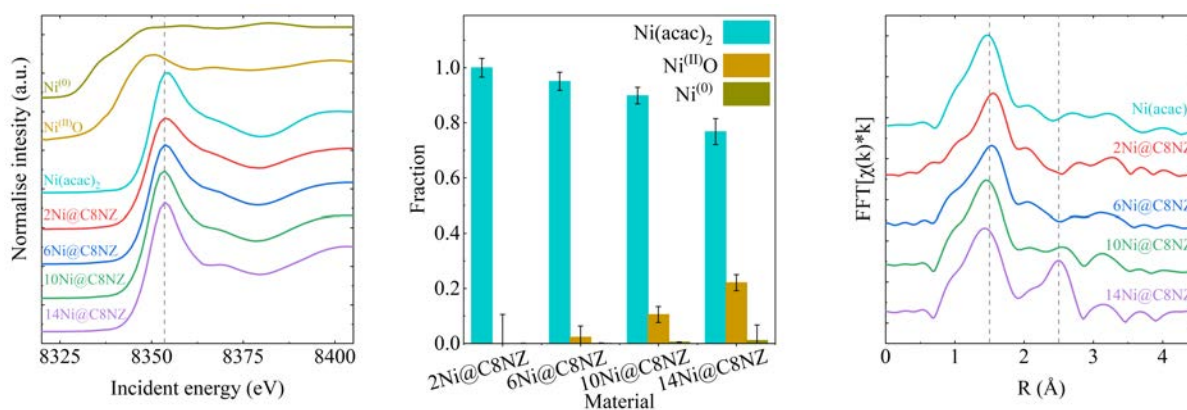


Figure 5.8: (From left to right) Normalized XANES spectra of Ni, NiO, $\text{Ni}(\text{acac})_2$, and Ni-decoration materials, linear combination fitting of Ni-decorated materials with Ni, NiO, and $\text{Ni}(\text{acac})_2$, Fourier Transformed EXAFS spectra of Ni decorated materials and $\text{Ni}(\text{acac})_2$ (no phase correction applied).

coordinated Ni(acac)₂, 22.1% NiO, and a minor fraction of 1.1% of bulk Ni⁽⁰⁾. While Ni⁽⁰⁾ has neither significant LCF contribution nor physical meaning in this context, NiO percentage indicates the presence of small nanoclusters which were not detectable by the standard characterization in 6Ni@C8NZ and 10Ni@C8NZ.

The local coordination environment of nickel atoms was further evaluated by Ni K-edge EXAFS. The k-weighted Fourier transform of the EXAFS of Ni(acac)₂, 2Ni@C8NZ, 6Ni@C8NZ, 10Ni@C8NZ, and 14Ni@C8NZ are reported in **Figure 5.8**. Without phase correction applied, this analysis depicts a prominent first shell scatter at 1.5 Å in all the samples and a second clear peak at 2.5 Å only for 14Ni@C8NZ. These results are consistent with LCF showing that 2Ni@C8NZ and 6Ni@C8NZ have dispersed isolated Ni centers and 14Ni@C8NZ has a significantly higher percentage of nanoparticles. 10Ni@C8NZ does not show a clear peak at 2.5 Å as 14Ni@C8NZ, nevertheless, its pair distribution function indicates a difference with the low Ni loading sample suggesting the presence of initial clustering.

After phase correction and fitting with the theoretical structure, the atomic distances and average coordination numbers were calculated. In particular, the second coordination shell peak at 3.0 Å is similar to the Ni-Ni distance of bulk NiO (2.94 Å), and it confirms the presence of oxide clusters in 10Ni@C8NZ and 14Ni@C8NZ. On the contrary, the nearest neighbor shell at 2.0 Å suffers from the limitation of EXAFS to distinguish light atom backscatters such as carbon, nitrogen, or oxygen.

Optimized theoretical structures of the 6Ni@C8NZ and 10Ni@C8NZ were obtained using a DFT-based dynamical simulated annealing (cell parameter in **Table 5.1**) and they are shown in **Figure 5.9**. The calculations were made considering nickel atoms in oxidation state +II in accordance with XPS and XANES findings. Coordination numbers obtained from the radial distribution functions of the simulated materials are coherent with XAS findings and provide further information. Nickel coordination environment at distances under 2.4 Å is mainly composed of oxygen for both samples with two oxygen atoms in the vicinity, one carbon and one nitrogen each (see **Table 5.1**).

In particular, the oxygen atoms are carrying a partial negative charge in 6Ni@C8NZ and 10Ni@C8NZ (i.e. -0.28 and -0.26, **table 5.2**), which helps to stabilize nickel atoms. Moreover, even though the material simulation has an atomic C/N ratio equal to 3:1, the nickel coordination environment is characterized by equal amounts of nitrogen and carbon atoms. This indicates that nitrogen might have a role in the stabilization of nickel atoms as well. Nevertheless, the absence of a clear increase in the contribution of the N-metal band in the N1s XPS suggested the absence of direct coordination bonds to nickel atoms (see the previous section). Hence, nitrogen might have a more important role in the Ni(acac)₂ dispersion preventing its clustering during heat treatment.[19]

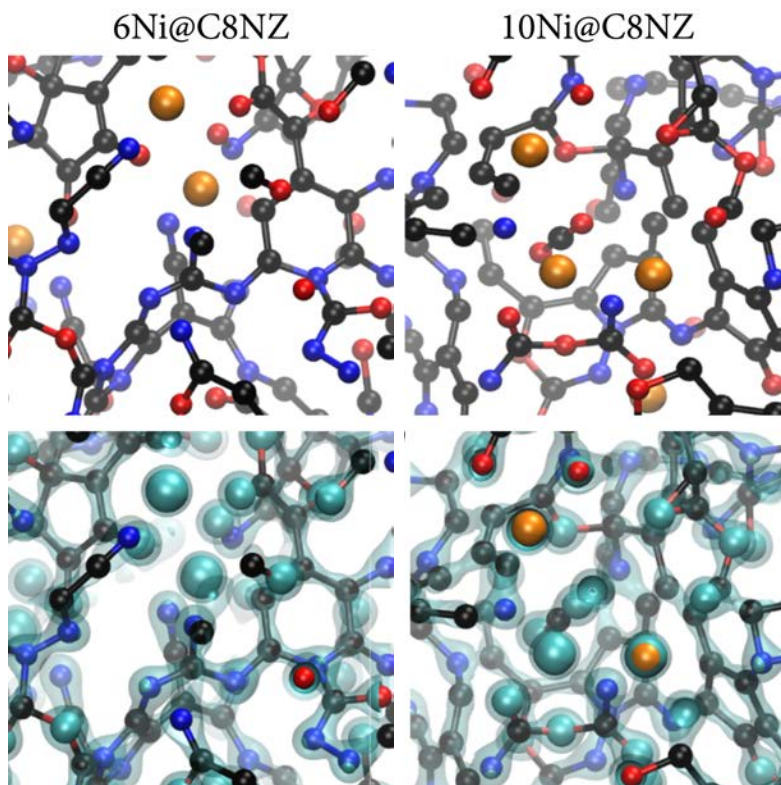


Figure 5.9: Snapshot of the modeled lowest energy structures (first row) and electron density isosurfaces of the same area (second row) of samples 6Ni@C8NZ (left column) and 10Ni@C8NZ (right column). Color code: carbon (black), nitrogen (blue), oxygen (red), nickel (orange).

Table 5.1: Nickel coordination numbers obtained by radial distribution function integration of simulated 6Ni@C8NZ and 10Ni@C8NZ.

Material	Number of atoms in supercell	Coordination number				
		Overall	C	N	O	Ni
6Ni@C8NZ	$C_{124}N_{42}O_{42}Ni_3$	4.56	1.17	1.19	2.15	0.04
10Ni@C8NZ	$C_{124}N_{42}O_{42}Ni_6$	4.99	1.18	1.45	2.29	0.07

Table 5.2: Average net atomic charges calculated using the DDEC6 method from simulated 6Ni@C8NZ and 10Ni@C8NZ.

Material	Average net atomic charges			
	C	N	O	Ni
6Ni@C8NZ	+0.20	-0.21	-0.28	+0.68
10Ni@C8NZ	+0.21	-0.18	-0.26	+0.66

5.4 Electrocatalytic activity for CO₂ reduction reaction

The catalytic conversion of carbon dioxide to more valuable products is a promising strategy to decrease greenhouse gas emissions. Among the different alternatives, the CO₂ electrochemical reduction has different advantages: it works at room temperature and it is easy to scale up. Nevertheless, the use of a catalyst is crucial to promote sustainable performances and transition metal-based catalysts supported on carbonaceous materials have attracted much attention in this regard.[20]

As introduced in **Chapter 1**, downsizing the metal dispersion is considered a promising alternative to increase the catalytic performances per metal mass unit. In particular, nickel-based single-atom catalysts are well known to promote highly selective electrochemical reduction from carbon dioxide to carbon monoxide.[21–23] However, the challenge to load a high percentage of nickel drove the focus on a mainly nitrogen-rich coordination environment and it avoided studying alternative coordination spheres of the single-atoms. As exposed throughout this chapter, xNi@C8NZ materials are characterized by mainly single atoms which have an average oxygen-rich coordination environment. Hence, their performance as a catalyst for CO₂RR was tested and the results will be described in this section.

At first, linear sweep voltammetry (LSV) in argon saturated 1M NaOH solutions showed a clear difference in the electrochemical properties of Ni-free and Ni-decorated materials (**Figure 5.10**). While 10Ni@C8NZ does not show significant current density in the potential window, C8NZ current density varies from +10 A g⁻¹ to -10 A g⁻¹ for the same potential range. Nevertheless, 10Ni@C8NZ has a lower onset potential (-1.1 V vs RHE) and a higher current density (1.107 A g⁻¹ at -1.1 V vs RHE) when the electrolyte is saturated with CO₂ compared to argon. On the contrary, C8NZ showed a lower onset potential and a higher current density in argon saturated electrolyte compared to CO₂ saturated electrolyte. Hence, nickel decoration activates the support towards the reduction of carbon dioxide.

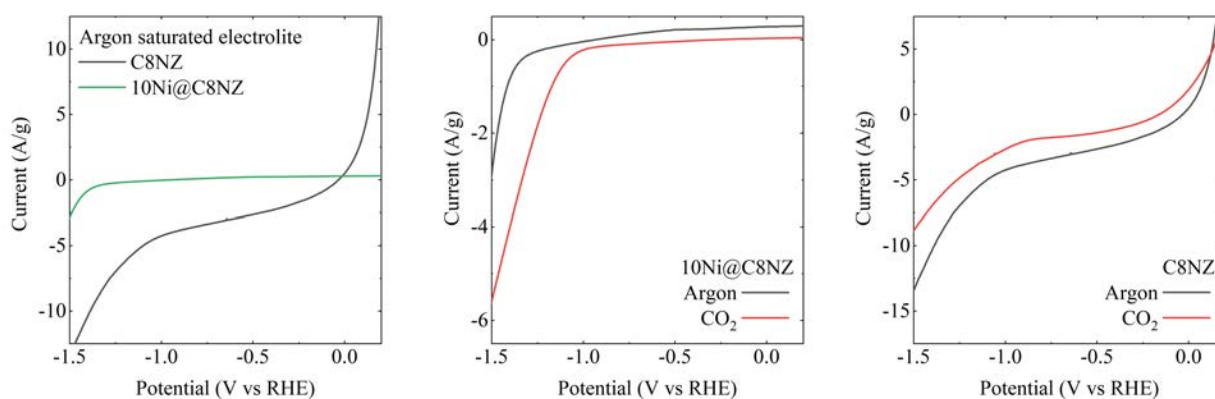


Figure 5.10: LSVs using NaOH 1M saturated with different gasses.

The electrochemical activity of xNi@C8NZ samples was further characterized by LSV as a function of nickel loading (**Figure 5.11**). However, only 6Ni@C8NZ, 10Ni@C8NZ, and 14Ni@C8NZ were considered because 2Ni@C8NZ showed similar properties to C8NZ.[19] LSV profiles indicate that 10Ni@C8NZ is the best catalyst due to its higher current density compared to 6Ni@C8NZ and 14Ni@C8NZ. In particular, 10Ni@C8NZ better performances can be ascribed to the higher nickel loading without significant aggregation.

Figure 5.11 reports the Faradaic efficiency (FE) towards different products obtained from the 10Ni@C8NZ catalysis after 4h at different potentials. Online GC was used to determine the FEs of the different gas products and off-line HPLC was used to determine the FEs of the liquid products. CO and CH₄ are the main product from CO₂ reduction at potential ranging from -0.8 V to -1.0 V vs RHE. HCOOH becomes the main CO₂ reduction product at 1.1 V vs RHE and the only direct product from CO₂ at 1.2 V and 1.3 V vs RHE. At larger potential, HER dominates the system and H₂ is practically the only detectable reaction product.

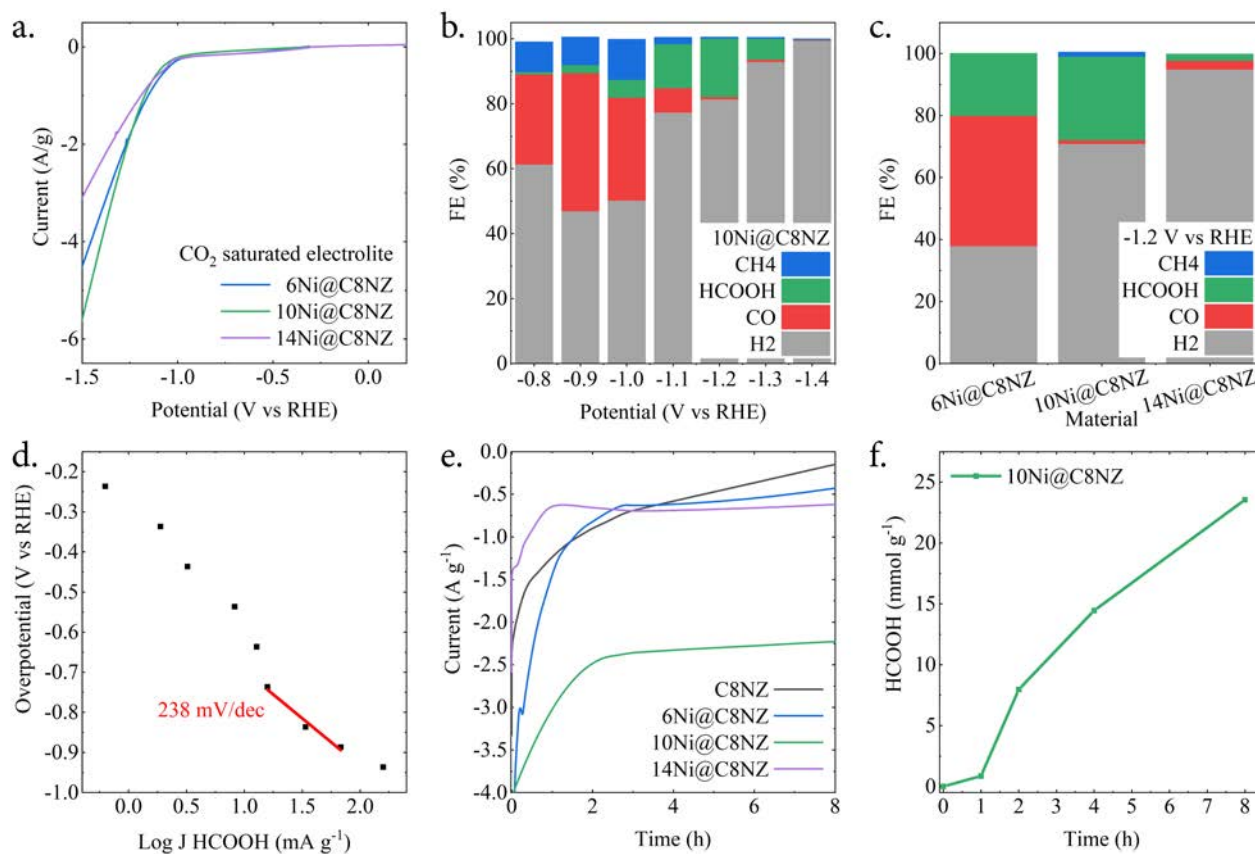


Figure 5.11: a. LSVs in CO₂-saturated NaOH 1M obtained using different electrode materials, b. FEs vs. applied potential of 10Ni@C8NZ in CO₂-saturated NaOH 1M, c. FEs of 6Ni@C8NZ, 10Ni@C8NZ, and 14Ni@C8NZ at -1.2 V vs RHE in CO₂-saturated NaOH 1M, d. Tafel slope calculated using 10Ni@C8NZ as cathode, e. chronoamperometry in CO₂-saturated NaOH 1M at -1.2 V vs RHE, f. formic acid concentration evolution using 10Ni@C8NZ as catalyst.

Moreover, nickel loading affects the product distribution and not only the current densities. **Figure 5.11** shows the FEs after 4 h at -1.2 V for 6Ni@C8NZ, 10Ni@C8NZ, and 14Ni@C8NZ. At lower Ni loading (i.e. 6Ni@C8NZ) higher FE towards carbon monoxide percentage was recorded, while at higher nickel loading (i.e. 14Ni@C8NZ) H₂ production is the main catalytic process observed. These results confirm the potential of single-atom catalysts as an alternative to nanoparticles-based catalysts and it highlights the crucial role of metal loading. These two factors lead to an unprecedented report of carbon-supported Ni single-atoms or clusters for HCOOH evolution from CO₂ electrochemical reduction.

The Tafel slope is often used as an indicator of the catalysis kinetics. However, the 10Ni@C8NZ catalysis is characterized by a high value (i.e. 238 mv dec⁻¹, see **Figure 5.11**) which does not hold useful information. Indeed, the absence of mesopores in the pore structure of the material - mainly characterized by micropores, see **Figure 5.4** - might imply mass transfer limitations and explain the high Tafel slope value.[24] Further studies on the mechanism of the catalyst are needed, but they are out of the scope of this thesis.

Finally, chronoamperometry (CA) measures were used to test the stability of the catalysis (**Figure 5.11**). In particular, the tests were carried out in a CO₂-saturated 1M NaOH solution at -1.2 V vs RHE with Ni-free and Ni-decorated materials. All the materials show a stable current up to 8 h, but only 10Ni@C8NZ presents a significantly higher current density compared to the other samples (2.5 A g⁻¹ vs 0.5 A g⁻¹). Coherently with the CA analysis, the production of HCOOH with 10Ni@C8NZ follows a linear trend with time indicating the stability of the catalyst in the working conditions up to 8 h (see **Figure 5.11**).

In conclusion, a high-nickel-loading carbonaceous material was synthesized with a cheap and easy impregnation-decomposition method. According to XAS and DFT calculation, the material presents nickel as single-atoms and small nanoclusters. Moreover, nickel atoms are characterized by an oxygen-rich coordination environment and high oxidation state. These parameters differs from the common reports in the literature and they were associated with the unprecedented production of HCOOH from CO₂RR with this type of material.

Bibliography

- [1] Che, M. Nobel prize in chemistry 1912 to sabatier: Organic chemistry or catalysis? *Catalysis Today* **218-219**, 162–171 (2013).
- [2] Alonso, F., Riente, P. & Yus, M. Nickel nanoparticles in hydrogen transfer reactions. *Accounts of Chemical Research* **44**, 379–391 (2011).
- [3] Tasker, S. Z., Standley, E. A. & Jamison, T. F. Recent advances in homogeneous nickel catalysis. *Nature* **509**, 299–309 (2014).
- [4] Yang, H. B. *et al.* Atomically dispersed ni(i) as the active site for electrochemical co2 reduction. *Nature Energy* **3**, 140–147 (2018).
- [5] Cheng, Y. *et al.* Atomically dispersed transition metals on carbon nanotubes with ultrahigh loading for selective electrochemical carbon dioxide reduction. *Advanced Materials* **30**, 1706287 (2018).
- [6] Zhao, S. *et al.* One-pot pyrolysis method to fabricate carbon nanotube supported ni single-atom catalysts with ultrahigh loading. *ACS Applied Energy Materials* **1**, 5286–5297 (2018).
- [7] Wang, Y. *et al.* High-efficiency oxygen reduction to hydrogen peroxide catalyzed by nickel single-atom catalysts with tetradentate n2o2 coordination in a three-phase flow cell. *Angewandte Chemie International Edition* **59**, 13057–13062 (2020).
- [8] Song, X. *et al.* Graphene-supported single nickel atom catalyst for highly selective and efficient hydrogen peroxide production. *ACS Applied Materials & Interfaces* **12**, 17519–17527 (2020).
- [9] Furlan, A., Lu, J., Hultman, L., Jansson, U. & Magnuson, M. Crystallization characteristics and chemical bonding properties of nickel carbide thin film nanocomposites. *Journal of Physics: Condensed Matter* **26**, 415501 (2014).
- [10] Biesinger, M. C. *et al.* Resolving surface chemical states in xps analysis of first row transition metals, oxides and hydroxides: Cr, mn, fe, co and ni. *Applied Surface Science* **257**, 2717–2730 (2011).

- [11] Barber, M. *et al.* High energy photoelectron spectroscopy of transition metal complexes. part 1.—bonding in substituted and unsubstituted first row carbonyls. *Faraday Discussions of the Chemical Society* **54**, 219–226 (1972).
- [12] Weiss, T., Warneke, J., Zielasek, V., Swiderek, P. & Bäumer, M. Xps study of thermal and electron-induced decomposition of ni and co acetylacetonate thin films for metal deposition. *Journal of Vacuum Science & Technology A* **34**, 041515 (2016).
- [13] Xie, L. *et al.* A ni(oh)₂-pto₂ hybrid nanosheet array with ultralow pt loading toward efficient and durable alkaline hydrogen evolution. *Journal of Materials Chemistry A* **6**, 1967–1970 (2018).
- [14] Aguilera-del Toro, R. H., Aguilera-Granja, F., Balbás, L. C. & Vega, A. Structure, fragmentation patterns, and magnetic properties of small nickel oxide clusters. *Physical Chemistry Chemical Physics* **19**, 3366–3383 (2017).
- [15] Kübel, C. *et al.* Recent advances in electron tomography: Tem and haadf-stem tomography for materials science and semiconductor applications. *Microscopy and Microanalysis* **11**, 378–400 (2005).
- [16] Bauer, M. & Bertagnolli, H. *X-Ray Absorption Spectroscopy – the Method and Its Applications*, chap. 7, 231–269 (John Wiley Sons, 2012).
- [17] Arrigo, R. *et al.* Influence of synthesis conditions on the structure of nickel nanoparticles and their reactivity in selective asymmetric hydrogenation. *ChemCatChem* **12**, 1491–1503 (2020).
- [18] Tarachand *et al.* Size-induced structural phase transition at 6.0 nm from mixed fcc–hcp to purely fcc structure in monodispersed nickel nanoparticles. *The Journal of Physical Chemistry C* **120**, 28354–28362 (2016).
- [19] Lepre, E. *et al.* Ni-based electrocatalysts for unconventional CO₂ reduction reaction to formic acid. *Nano Energy* **97**, 107191 (2022).
- [20] Cheng, Y., Yang, S., Jiang, S. P. & Wang, S. Supported single atoms as new class of catalysts for electrochemical reduction of carbon dioxide. *Small Methods* **3**, 1800440 (2019).
- [21] Yang, H. *et al.* Atomically dispersed ni(i) as the active site for electrochemical co₂ reduction. *Nature Energy* **3**, 140–147 (2018).
- [22] Möller, T. *et al.* Efficient co₂ to co electrolysis on solid ni–n–c catalysts at industrial current densities. *Energy & Environmental Science* **12**, 640–647 (2019).
- [23] Hu, X.-M. *et al.* Selective co₂ reduction to co in water using earth-abundant metal and nitrogen-doped carbon electrocatalysts. *ACS Catalysis* **8**, 6255–6264 (2018).

- [24] Sun, L., Reddu, V., Fisher, A. C. & Wang, X. Electrocatalytic reduction of carbon dioxide: opportunities with heterogeneous molecular catalysts. *Energy & Environmental Science* **13**, 374–403 (2020).

Chapter 6

Conclusion

The presented thesis aimed to describe the synthesis, characterization, and applications of carbonaceous materials obtained from nucleobase and nucleobase-like molecules via the salt melt templating method. This strategy produces highly nitrogen-doped carbonaceous materials, which have potential applications as cathodes for energy storage devices and heterogeneous catalysts in thermal and electrocatalysis.

Chapter 2 described the effect of precursor, salt mixture, and temperature on the final material properties. The precursor choice mainly impacts the pore structure and the material's morphology. The kinetics of the precursor condensation is central because this process competes with the precursor solvation. The salt mixture choice impacts the materials' composition, pore structure, and morphology. The presence of zinc is central to favoring the production of highly microporous materials because it affects the material's decomposition, resulting in lower nitrogen content and larger micropore volume than a zinc-free salt mixture. The impact of the temperature was observed mainly on composition and pore structure. In presence of ZnCl_2 , high temperatures (i.e., 800 °C) favors the loss of nitrogen atoms and generates larger micropore volume.

Overall, the salt melt templating method with nucleobases or nucleobase-like molecules is a competitive way to synthesize highly-doped porous carbons. In particular, doping is highly influenced by the use of aromatic heterocycles. On the other hand, the porosity is affected by a sol-gel mechanism - which occurs at temperatures lower than 500 °C - and the material decomposition is similar to the chemical activation with ZnCl_2 .

Chapter 3 highlighted the material resistance against oxidative modification and their performance as cathodes for Li-ion capacitors. Caffeine-derived materials were shown to have a stable elemental composition before and after harsh ball milling conditions (i.e., air atmosphere, 650 rpm, 50 min). In contrast, a commercial porous carbon was shown to uptake oxygen and iron atoms after the same procedure. Ball milling was used to produce a composite material by mix-

ing the caffeine-derived materials with a conductive phase, leading to improved performances as cathodes in Li-ion capacitors. Among the composites material, caffeine-derived cathodes presented a larger capacity than commercial carbon-derived cathodes. In particular, higher nitrogen content appeared crucial in the improved performance.

Chapter 4 showed the relationship between nitrogen speciation and catalytic activity for reduction, oxidation, and acid/base reactions. Cytosine-derived materials obtained at different temperatures (i.e., 500, 600, 700, 800 °C) in the presence of zinc chloride and lithium chloride were used as catalysts for the reduction of nitrobenzene, oxidation of 3,3',5,5'-Tetramethylbenzidine, CO₂ cycloaddition reaction to epoxides, and a two-step one-pot reaction from (dimethoxymethyl) benzene to benzomalonitrile. The material obtained at 800 °C resulted in the one with the highest activity for the reduction and oxidation reactions. Its higher activity was associated with the larger conjugated domains, which helped the electron transfer. The material obtained at 600 °C was shown to be the most active for the CO₂ cycloaddition reaction, suggesting the presence of a balanced amount of basic and acid sites. These were characterized by the one-pot two-step reaction, which indicated the loss of basic sites and the increase of acidic sites with the increasing synthetic temperature.

These results were correlated to the nitrogen and carbon speciation observed by X-ray photoelectron spectroscopy. In particular, the loss in electron-rich (pyridinic- and pyrrolic-like) nitrogen atoms was observed with the increasing temperatures. This was associated with the change in the materials' acid/base properties (i.e., loss of basic active sites). Moreover, the enrichment in electron-rich carbon atoms, associated with higher synthetic temperature, was identified as a leading factor in the superior activity for oxidation and reduction reactions of the material obtained at 800 °C. Finally, temperature programmed desorption suggested that the active acidic sites are the electron-poor carbon atoms observed by X-ray photoelectron spectroscopy.

Chapter 5 described the potential of such materials as supports for single-atom distributions and their unconventional selectivity in CO₂RR. A simple top-down method was used to load nickel up to 10 wt% without observing agglomeration into large nanoparticles. The highly doped material used as support helped the surface dispersion of the nickel precursor, and its resistance against oxidative modification allowed to operate the precursor decomposition in air atmosphere. According to X-ray absorption and DFT calculation, the final material presented nickel mainly as single-atoms with a small percentage of nanoclusters. Moreover, an average oxygen-rich coordination environment characterizes the material surface's nickel dispersion. The Ni-decorated materials were used as catalysts for the carbon dioxide reduction reaction. Compared to literature, the materials resulted in an unconventional selectivity towards mainly formic acid. This unconventional selectivity was associated with the nickel high oxidation state and the oxygen-rich coordination environment.

In conclusion, this thesis provided a comprehensive picture of nitrogen-doped carbonaceous materials and their application. The properties of these materials were described according to the up-to-date characterization techniques, which highlighted the potential and limitations of nitrogen doping in carbon-based materials. The study of these materials proved their broad applicability and novel strategies to improve their performance. These results correspond to the initial motivation and will help the conscious use of nitrogen-doped carbonaceous materials for energy and catalysis toward a more sustainable society.

Chapter 7

Appendix

7.1 Methods applied

Thermogravimetric analysis (TGA)

Thermogravimetric analysis is based on measuring the sample mass while its temperature increases. By recording the mass fluctuation, it is possible to understand if the sample undergoes thermal decomposition, showing a mass decrease, or reacts with the atmosphere, resulting in a mass increase. Both processes depend highly on the working atmosphere and the heating ratio, which can be controlled depending on the investigation.

The experiments in this thesis were performed on a NETZSCH TG 209 F1 Libra device. In a standard procedure, the sample was heated up from 50 °C to 1000 °C, using 1 °C min⁻¹ as the heating ratio, synthetic air or nitrogen as atmosphere, and a Pt crucible to hold the sample. Antje Voelkel performed the measurements.

Powder X-ray diffraction (X-ray)

X-ray diffraction is a widely used technique to characterize crystalline materials. This method is based on two phenomena: 1. *scattering* of the radiation and 2. *interference* between different scattered radiations. In particular, scattering is a phenomenon that occurs when the incident radiation has a comparable wavelength (λ) to the object, resulting in the diffusion of the radiation in all directions. Hence, using X-rays (10 pm < λ < 10 nm), it is possible to observe the scattering from objects of atomic dimensions. When multiple objects scatter radiation, the different scattered radiations can interact, resulting in constructive (increasing the overall intensity) or destructive (decreasing the overall intensity) interference. When ordered structures are investigated, their X-ray scattering is dominated by interference, resulting in a characteristic pattern. Bragg's law (**Equation 7.1**) describes these phenomena as a function of the wavelength (λ), the atomic distance (d), and the incident angle (θ):

$$n\lambda = 2d\sin(\theta) \quad (7.1)$$

where n is an integer number. In particular, a diffraction experiment measures the radiation intensity from powder samples at defined angles. When the angle satisfies **equation 7.1**, a peak can be measured from the detector, and the atomic distance can be derived. Nonetheless, no peak can be observed in the absence of an ordered lattice, while amorphous materials such as amorphous carbon can still present broad diffraction bands.

This thesis used a Bruker D8 advance diffractometer to record the diffraction pattern. A Cu-K α lamp was used to generate X-ray radiation ($\lambda = 1.54 \text{ \AA}$). The pattern was recorded from 5° to 70° at 0.5° min⁻¹

Ultraviolet–visible spectroscopy (UV-Vis)

Ultraviolet-visible spectroscopy is a widely used analytical technique for the quantitative determination of analytes and electronic state characterization. In a standard measurement, the sample is irradiated with UV and visible radiation, and the intensity of the incident radiation (I_0) is compared to the intensity of the transmitted radiation (I). In particular, the ratio between I and I_0 is defined as transmittance (T , see **Equation 7.2**).

$$T = \frac{I}{I_0} \quad (7.2)$$

The transmittance is a function of concentration (c), path length (L), and the substance irradiated (extinction coefficient, ϵ) as described by the Beer-Lambert law (**Equation 7.3**).

$$A = \log_{10}(T^{-1}) = \log_{10}\left(\frac{I_0}{I}\right) = \epsilon c L \quad (7.3)$$

where A is defined as absorbance and is commonly plotted on the y-axis for UV-Vis spectroscopy. More in detail, the ultraviolet and visible light have comparable energy to the energy gap between electronic states, and when the two energy match (**Equation 7.4**) the part of the incident radiation is absorbed by the sample, increasing the absorbance.

$$\Delta E = h\nu \quad (7.4)$$

This thesis used a T70 single beam spectrophotometer from PG Instruments Ltd. The spectral bandwidth was fixed at 2 nm, and the spectra were recorded with a step size equal to 1 nm and frequency similar to 1 s^{-1} .

Inductively coupled plasma atomic emission spectroscopy (ICP-AES)

Inductively coupled plasma atomic emission spectroscopy is an atomic spectroscopic technique used for qualitative and quantitative analysis of chemical elements. It is an emission spectroscopy technique and uses inductively coupled plasma to excite atoms or ions that emit electromagnetic radiation upon relaxation. The emission intensity is characteristic for each element analyzed and can be directly correlated to its concentration via a calibration curve.

ICP-AES Optima 8000 Perkin Elmer was used to perform the measurements reported in this thesis. Calibration was performed with Multi-Element-Standards, and the samples were treated in aqua regia for 12 h at room temperature and 1 h at 50 °C before measuring. Jessica Brandt performed the measurements.

Fourier-transform infrared spectroscopy (FT-IR)

Fourier-transform infrared spectroscopy is a common technique to characterize the chemical functionalities in molecules and materials. Similar to UV-Vis, it is based on radiation absorption by the sample. Different from UV-Vis, it uses infrared radiation ($40 < \tilde{\nu} < 4000 \text{ cm}^{-1}$, where $\tilde{\nu} = 1/\lambda$), which matches the energy of vibrational transitions. The absorption wavenumber ($\tilde{\nu}$) is a function of bond strength (k) and atom mass (m) as described in **Equation 7.5**:

$$\tilde{\nu} = \frac{1}{2\pi c} \sqrt{\frac{k}{\mu}} \quad (7.5)$$

where c is the speed of light and μ is the reduced mass ($\mu = m_1 m_2 / (m_1 + m_2)$). Nonetheless, the signal of IR absorption can be detected only if a change in dipole is associated with the vibrational mode. Moreover, the FTIR setup is based on a Michelson interferometer which enables the generation of an interferogram from a beam of many frequencies. The actual spectrum is derived from the data processing of the interferogram via Fourier Transformation.

A Thermo Scientific Nicolet iD5 spectrometer was used to collect the spectra of this thesis.

Nuclear magnetic resonance (NMR) spectroscopy

Nuclear magnetic resonance is a physical phenomenon and describes the perturbation from a weak oscillating magnetic field of nuclei in a strong constant magnetic field (B_0). It is widely used in spectroscopy to characterize molecular organic compounds in solution. The interaction between a magnetic field and the nuclei magnetic moment results in an energy splitting which is a function of gyromagnetic ratio (γ), magnetic quantum number (m), and the effective magnetic field (B):

$$E = -\gamma m \hbar B \quad (7.6)$$

where \hbar is the reduced Planck constant. In particular, the effective magnetic ratio is influenced by the applied magnetic field (B_0) and the induced magnetic field (B_i):

$$B = B_0 + B_i \quad (7.7)$$

B_i is influenced by the chemical environment of the nuclei in analysis, and the comparison with a reference signal allows to appreciate small differences, resulting in one of the most accurate chemical determinations available.

NMR spectroscopy is a powerful method to analyze the concentration of molecules in solution. Indeed, the intensity of the signal is proportional to the moles in the solution and the number of protons involved in the signal. Hence, the addition of an internal standard (*i.s.*) of known

concentration can be used to determine the concentration of molecules in solution according to **Equation 7.8**

$$\frac{M_x}{M_{i.s.}} = \frac{I_x}{I_{i.s.}} \frac{N_{i.s.}}{N_x} \quad (7.8)$$

Where M is the molarity, I is the intensity of the signal, and N is the number of nuclei associated with the signal.

In this thesis, $^1\text{H-NMR}$ were recorded on Ascend 400 MHz.

X-ray photoelectron spectroscopy (XPS)

X-ray photoelectron spectroscopy is a surface-sensitive quantitative spectroscopic technique. It is based on the emissions of the electrons when electromagnetic radiation hits a material (*photoelectric effect*). Each element emits photoelectrons with specific energy, and their number is related to the element content. For these reasons, the technique enables qualitative and quantitative analysis of the elemental composition. Nonetheless, the mean free path of the photoelectrons limits the bulk analysis by XPS, and the maximal depth is estimated to be around 5 to 10 nm. Hence, XPS is considered surface-sensitive and can be applied to conductive materials to avoid charging. Moreover, the electron energy depends on their chemical and electronic environment, and XPS can reveal information on the binding state of each element. The binding energy (E_{binding}) can be calculated accordingly to the **Equation 7.9**:

$$E_{\text{binding}} = E_{\text{photon}} - (E_{\text{kinetic}} + \phi) \quad (7.9)$$

where E_{photons} is the energy of the X-ray photons, E_{kinetic} is the kinetic energy of the electrons, and ϕ is a work function term specific for each materials. Usually, ϕ is measured using a standard material and acts as a correction for experimental fluctuation characteristic of the setup. A typical XPS spectrum reports the signal intensity as a function of the binding energy, and peak-fitting is usually conducted with specialized software. The peak identification is based on an experimentally determined and theoretically calculated binding energy state.

A Thermo Scientific Escalab 250 Xi was used to perform the measures in this thesis. The instrument used a micro-focused monochromated Al $K\alpha$ source (1486.68 eV) and a 400 μm spot size. LiCl was added to each sample to calibrate the binding energies, and calibration was performed towards Li^+ . Thermo Scientific Advantage software was used to perform the peak-fitting. The measurements were performed by Dr. Johannes Schmidt (TU Berlin).

X-ray absorption absorption (XAS)

X-ray absorption spectroscopy considers the electromagnetic radiation absorption associated with atomic core level transitions. X-ray absorption near edge structure (XANES), or near edge X-ray absorption fine structure (NEXAFS), is a subset of X-ray absorption spectroscopy, which considers the energy region up to 50-100 eV above the selected core level ionization energy. XANES is a powerful technique due to its elemental specificity, and it can be used to extract information about element valence and its ligand geometry. Nonetheless, XANES requires an intense and tunable source of X-rays, and for this reason, they are performed at synchrotron.

Extended X-ray absorption fine structure (EXAFS) is a subset of X-ray absorption. It considers the extended region after the absorption edge up to 1000 eV, characterized by an oscillating absorption coefficient. This phenomenon is caused by the backscattered photoelectrons from the surrounding environment of the excited atoms, which can be modeled with plane-wave single-scattering considering the correction for curved-wave and multiple-scattering effects. Through this analysis, it is possible to understand the excited atoms' coordination number and atomic distances.

The Ni K edge X-ray absorption fine structure was recorded in transmission mode at Bessy II at mySpot beamline. A Si(111) multiple crystal monochromator was used for the energy selection, and an ionization chamber with air was used for signal detection. The first inflection point of the Ni(0) XANES spectrum (8333 eV) was used for the energy calibration. The beam spot size was 0.5 mm and the total flux was $1.5 \cdot 10^{11}$ ph s⁻¹. Athena and Artemis software were used to analyze extended X-ray absorption fine structure (EXAFS). Ernesto Scoppola and Ivo Zizak provided crucial support in recording the XAFS spectra, Michal Nowakowski performed the XANES and EXAFS elaboration, and Julian Heske and Thomas D. Kühne performed the DFT calculations.

Scanning electron microscopy (SEM)

Scanning electron microscopy is an imaging technique based on a focused beam of electrons. The interaction between electrons and the material's surface produces various signals containing surface topography and composition information. Depending on the mode, SEM can detect low-energy secondary electrons (*SE*) emitted from the material surface and high-energy backscattered electrons (*BE*). While SE holds surface morphology information, BE is influenced by the sample composition. Indeed, the scattering process depends on the element's atomic mass, and heavier atoms appear brighter when BE are measured. To facilitate the measure, the sample must be conductive, and the surface is usually spattered with gold or platinum.

In this thesis, A LEO 1550-Gemini microscope operating from 3.00 kV to 20.00kV was used to record SEM images. Before the measurement, all samples were sputtered with a film (approximately 10 nm, 80% gold, and 20% platinum) to increase their conductivity. Bolortuya Badamdorj and Heike Runge recorded the SEM images.

Energy-dispersive X-ray spectroscopy (EDX)

Energy-dispersive X-ray spectroscopy is an analytical technique commonly used for elemental analysis. It is based on an electron beam with enough energy to extract electrons from the core levels of the sample irradiated. Upon this process, the atom enters an excited state and can relax by the hole filling from outer electron shells. X-ray radiation is emitted during the atom relaxations. The energy of the emitted radiation corresponds to the energy gap between the two electronic states and is characteristic of each element. Hence, the sample's elemental composition can be extracted from the number of photons emitted. Usually, this measure is coupled with a scanning electron microscope or a scanning transmission electron microscope. Bolortuya Badamdorj and Heike Runge recorded the SEM-EDX Spectra.

This thesis used a Link ISIS-300 system from Oxford instrument Group equipped with Si(Li) to record the EDX spectra.

Scanning transmission electron microscopy (STEM)

Similar to SEM, scanning transmission electron microscopy is based on a focused electron beam. Nonetheless, The detector analyzes the transmitted electrons from the sample, often prepared as a thin film. The contrast in STEM imaging is a function of sample thickness (i.e., darker the spot, thicker the sample) and the composition (i.e., darker the area, heavier the atoms). Compared to SEM, STEM imaging can provide more magnified imaging of the samples, and aberration-corrected images from STEM can provide atomic-scale resolution. More in detail, *bright field* mode detects the unscattered electrons and is sensible to the lattice of the materials (diffraction contrast). In contrast, *high angle annular dark field (HAADF-STEM)* mode detects the scattered electrons, which are dependent on the atomic weight of the atoms (Z-contrast).

This thesis used a double Cs corrected JEOL JEM-ARM200F (S)TEM operated at 80 kV to conduct the STEM imaging. The instrument was equipped with a cold-field emission gun and a Gatan Quantum GIF spectroscopy system. A probe coverage semi-angle of 41.7 mrad was used to collect the HAADF-STEM images. Heike Runge recorded the STEM images while Tobias Heil performed the high resolution STEM imaging.

Nitrogen adsorption/desorption isotherms

Gas adsorption measurements are widely used for the characterization of porous materials. By recording the amount of gas adsorbed on the material as a function of the pressure at constant temperature, it is possible to obtain various information about the specific surface area, the pore volume, and the pore structure. In particular, nitrogen adsorption measurements are commonly recorded at 77K, comparing the sample cell pressure to the pressure of an empty cell (relative pressure). Nitrogen interactions with materials surfaces are weak Van der Waals interactions resulting in the physisorption of the gas. This can be analyzed by the Brunauer, Emmett, and Teller (BET) theory (**Equation 7.10**) which allows to determine the specific surface area of the material from the adsorbed gas amount (n_a) at the defined relative pressure (P/P_0):

$$\frac{P/P_0}{n_a(1 - P/P_0)} = \frac{1}{n_m C} + \frac{C - 1}{n_m C} P/P_0 \quad (7.10)$$

where n_m is the monolayer capacity and C is considers the net molar adsorption energy. Hence, the material surface area (S_{BET}) can be calculated as:

$$S_{BET} = n_m a_m N_A \quad (7.11)$$

where N_A is the Avogadro constant and a_m is the area occupied by an adsorbate molecule. BET analysis is normally performed between $0.05 < P/P_0 < 0.4$, the adsorbed N_2 amount has to increase with increasing P/P_0 , and the linear region has to have a positive intercept, resulting in a positive C value.

Besides surface area, the pore volume and the pore size distribution can be derived from the nitrogen isotherms. Historically, these values were calculated from the Kelvin equation to estimate the shift of the gas-liquid phase transition of a confined liquid:

$$\ln(P/P_0) = -\frac{2\gamma V_m}{RT(r_p - t_c)} \quad (7.12)$$

where γ is the surface tension of the bulk fluid, V_m is the molar liquid volume, r_p is the pore radius (considering cylindrical pores), and t_c is the thickness of the adsorbed multilayer film formed prior to pore condensation. This method was included in more sophisticated models such as the Barrett-Joyner-Halenda (BJH). Nonetheless, the Kelvin equation's validity is questionable and narrows its application. Today, molecular simulation or DFT are commonly used and provide a reliable determination of mesopores volume and pore size distribution.

This thesis used a Quadrasorp apparatus from Quantachrome Instruments to perform the nitrogen physisorption experiments. These were performed at 77 K, and the sample was degassed at 150 °C for 20 h in a high vacuum before the experiments. Multi-point BET model in the relative pressure below 0.2 was used to determine the surface area using the Rouquerol criteria.

Carbon dioxide adsorption isotherm

Differently from N₂ adsorption experiment, CO₂ adsorption experiments are typically conducted at 273 K. The higher working temperature allows carbon dioxide to access smaller pores thanks to its higher kinetical energy, and CO₂ sorption is usually considered for the characterization of micropores. Nonetheless, CO₂ can interact with primary sites due to its electron-poor carbon atom, resulting in chemical interaction when basic sites (e.g., pyridinic nitrogen) are present in the sample. Hence, most physisorption models cannot be applied to the materials in analysis, and only the total pore volume can be calculated.

Similar to N₂ sorption measurements, CO₂ sorption experiments were conducted to a Quadrasorp instrument. The measures were performed at 273 K, and the samples were degassed at 150 °C for 20 h before the experiment.

Temperature programmed desorption

Temperature programmed desorption (TPD) is a useful technique to characterize binding sites on the material surface. In particular, it considers the desorption of molecules from the material surface upon increasing temperature. These molecules are usually adsorbed on the material surface by pulse chemisorption. TPD profiles are reported as the intensity of the signal versus the temperature of the samples and highlight the amount and the strength of the binding sites to the adsorbed molecules.

This thesis used an AMI-300lite from Altamira Instruments to record the TPD profiles. These were recorded by pulsing at 50 °C ammonia until the sample was not saturated. After saturation, the bed temperature increased to 500 °C at 10 °C min⁻¹.

7.2 List of used chemicals

Table 7.1: List of substances used in this thesis with relative CAS registry number, supplier, and purity grade. All the substances were used without further purification.

Substance	CAS	Supplier	Purity grade
Cytosine	71-30-7	Merck	> 98%
Adenine	73-24-5	Sigma-Aldrich	> 99%
Caffeine	58-08-2	Sigma-Aldrich	> 99%
Zinc chloride	7646-85-7	Alfa Aesar	> 98%
Lithium chloride	7447-41-8	Sigma-Aldrich	> 98%
Sodium chloride	7647-14-5	Fischer Chemicals	> 99%
Potassium chloride	7447-40-7	Sigma-Aldrich	> 98%
Hydrochloric acid (37%)	7647-01-0	Roth	> 98%
Cyanamide	420-04-2	Sigma-Aldrich	> 99%
1-Methyl-2-pyrrolidinone	872-50-4	Alfa Aesar	> 99%
Polyvinylidene difluoride	24937-79-9	MPI corporation	> 99%
Nitrobenzene	98-95-3	Sigma-Aldrich	> 99%
Hydrazine monohydrate	7803-57-8	Sigma-Aldrich	> 99%
3,3',5,5'-Tetramethylbenzidine	54827-17-7	Roth	> 99%
Hydrogen peroxide solution (30% w/w)	7722-84-1	Sigma-Aldrich	> 99%
Epichlorohydrin	106-89-8	Sigma-Aldrich	> 99%
Benzaldehyde dimethyl acetal	1125-88-8	Sigma-Aldrich	> 99%
Malononitrile	109-77-3	Acros Organics	> 99%
Ethanol	64-17-5	Fisher Scientific	> 98%
Acetonitrile	75-05-8	Acros Organics	> 99%
Nickel(II) acetylacetonate	3264-82-2	Alfa Aesar	> 99%
Sulfuric acid	7664-93-9	Roth	> 99%
Sodium hydroxide	1310-73-2	Roth	> 99%

7.3 Material synthesis

Salt melt templated synthesis

Using an agate mortar, 2 g of precursor (i.e., cytosine, adenine, or caffeine) were mixed with 40 g of a salt mixture (i.e., $\text{LiCl}_2/\text{ZnCl}_2$, $\text{NaCl}_2/\text{ZnCl}_2$, LiCl/KCl in 1/1 wt% mixtures). The solid mixture was transferred to a ceramic crucible and closed with a ceramic lid. The crucible containing the solid mixture was heated at $1\text{ }^\circ\text{C min}^{-1}$ in an oven saturated with nitrogen up to a defined temperature (i.e., 500, 600, 700, 800 $^\circ\text{C}$). This temperature was kept for 2h. Once this time passed, the heating was turned off, and the oven cooled down spontaneously, keeping the saturated nitrogen atmosphere. As soon as the oven reached room temperature, the crucible was removed from the oven, and the solid mixture was washed in HCl (1M) overnight two times at room temperature and one time at 50 $^\circ\text{C}$. After the last washing, the sample was first dried at 70 $^\circ\text{C}$ for 4 h and second at 150 $^\circ\text{C}$ in a vacuum oven overnight. The final material appears a fluffy black powder.

This method was used to synthesize C8LZ, A8LZ, CF8LZ, C8LK, C8NZ, C5LZ, C6LZ, C7LZ, CF7NZ, and CF7NZ.

Ball milling of caffeine derived materials

In a standard procedure, 54 g of material were placed in a 12.5 mL stainless steel jar with five stainless steel balls of 1 cm diameter. Using a planetary ball mill (Retsch PM100), the solid was ground for 50 min at 650 rpm.

Nitrogen doping of commercial carbon (Kuraray)

1 g of commercial Kuraray carbon material was soaked in 2 mL water solution of cyanamide (1 g/mL) and stirred for 6 h at room temperature. Successively, the water was evaporated at 60 $^\circ\text{C}$ for 12 h leaving a solid mixture. This was submitted to a heat treatment in a nitrogen-saturated atmosphere at 800 $^\circ\text{C}$ for 4 h using a $1\text{ }^\circ\text{C min}^{-1}$ heating ratio. A fluffy black powder was obtained upon spontaneous cool down of the oven.

This method was used to prepare N-Kur.

Metal loading

100 mg of a carbon material were mixed with different amounts (i.e., 10, 30, 50, and 70 mg) of nickel(II) acetylacetonate. 5 ml of acetone were added to the solid mixture, and the system

was stirred for 2 h at room temperature. After stirring, the acetone was evaporated at 70 °C for 4 h. The resulting solid mixture was transferred to a ceramic crucible and closed with a ceramic lid. The crucible was submitted to a heat treatment at 350 °C using 1 °C min⁻¹ as heating ratio without prior gas saturation of the atmosphere, leading to the treatment in air. The temperature was kept for 2 h, and the oven was let to cool down spontaneously afterward. A fluffy black powder was obtained as a result.

This method was used to synthesize 2Ni@C8NZ, 6Ni@C8NZ, 10Ni@C8NZ, 14Ni@C8NZ.

7.4 Catalytic experiments

Nitrobenzene reduction

A microwave vessel was loaded with nitrobenzene (36.9 mg, 0.30 mmol), 5 mg of the catalyst, ethanol (3 mL), and hydrazine monohydrate (58.2 µL, 1.2 mmol). After adding a stir bar, the vessel was sealed with a septum and parafilm. The system was stirred at room temperature. After the corresponding time, the vessel was opened, and 1,3,5-trimethoxybenzene (internal standard, 50.5 mg, 0.30 mmol) was added. After sonicating for 5 minutes, an aliquot of the mixture was diluted in CDCl₃ and analyzed by ¹H-NMR. Cristian Cavedon performed the nitrobenzene reduction experiments.

TMB oxidation

A plastic vial (2 mL) was loaded with AcOH/AcONa buffer (900 µL, 0.5 M), 3,3',5,5'-tetramethyl-[1,1'-biphenyl]-4,4'-diamine solution in DMSO (40 µL, 12.5 mM), and H₂O₂ solution in H₂O (40 µL, 1 M). To start the reaction, a dispersion of the catalyst in water (20 µL, 0.25 mg mL⁻¹) was added to the vial, and the system was rapidly mixed. Immediately after the catalyst addition, the absorbance at 652 nm was measured as a function of time.

The Michaelis-Menten kinetics was used to analyze the properties of the catalyst. Hence, different H₂O₂ solution (i.e. 0.25, 0.50, 0.75, 1.0, 1.25, 1.5 M) were prepared and added (40 µL) to the system described in the previous paragraph. Solvent, substrate, and catalyst concentrations were kept constant. The initial reaction rate (v_0) was measured from the absorbance as a function of the time, and its inverse was plotted against the inverse of H₂O₂ concentration. Hence, K_M and v_{max} can be calculated from their linear relationship:

$$\frac{1}{v_0} = \frac{K_M}{v_{max}} \cdot \frac{1}{[H_2O_2]} + \frac{1}{v_{max}}$$

CO₂ cycloaddition

An autoclave system (Berghof BR-100, 100 mL) equipped with a stir bar was loaded with the catalyst (50 mg), epichlorohydrin (5 mL, 64 mmol), and 1,3,5-trimethoxybenzene (internal standard, 140 mg, 0.8 mmol). The system was sealed and fluxed three times with CO₂. The autoclave was pressurized with CO₂ (5 Bar) and heated up to 150 °C. After 3 h, the heating was turned off, and the system spontaneously cooled down. Once at room temperature, the autoclave was opened to release the gas pressure. The reaction media was filtered and appeared as a viscous orange liquid when the reaction was successful. The filtration was diluted in CDCl₃ and ¹H-NMR was used to determine the conversion and selectivity.

(dimethoxymethyl)benzene to benzomalononitrile

A round bottom flask was loaded with benzaldehyde dimethyl acetal (152 mg, 1 mmol), malononitrile (66 mg, 1 mmol), water (50 µL, 2.8 mmol), 1,3,5-trimethoxybenzene (internal standard, 70 mg, 0.4 mmol), catalyst (50 mg), and acetonitrile (2 mL). The reaction mixture was stirred and kept at 80 °C using an oil bath. After the corresponding time, an aliquot of the mixture was collected, filtered, and diluted in acetone-d₆. ¹H-NMR was used to determine the species concentration, yields, and selectivity. Sylvain Rat performed the conversion from DMB to BMN.

7.5 Electrochemical methods

Li-ion capacitor

To prepare the electrodes, the active material (42 mg) and the conductive super P carbon (12 mg) were initially ground using ball milling (50 min, 650 rpm, 12.5 mL Jar, 5 balls of 1 cm). Subsequently, a PVDF solution (1 mL, 6 mg mL⁻¹) was added to the solid mixture and ground for 10 min under the same conditions. 40 µL of the prepared ink were dropped on 11 mm carbon paper discs (Spectracarb 2050A-0550) and dried for 1 h at 80 °C to remove the volatile impurities. The electrode was dried at 120 °C for 17 h under a vacuum. The electrodes loading was 2.0-2.5 mg cm⁻².

A Swagelok-type cell was used to perform all the electrochemical measurements (**Figure 7.1**). Lithium foil was used as the counter electrode, a Celgard 2325 (diameter 13 mm, thickness 25 µm) was used as the membrane, and a solution of LiPF₆ (1M) in ethylene carbonate and diethyl carbonate (1:1 v/v, 100 µL, used as obtained from Sigma-Aldrich) was used as electrolyte. A circular carbon current collector covered with the active material was used as the working electrode. All cells were assembled in the glove box with low oxygen and water levels.

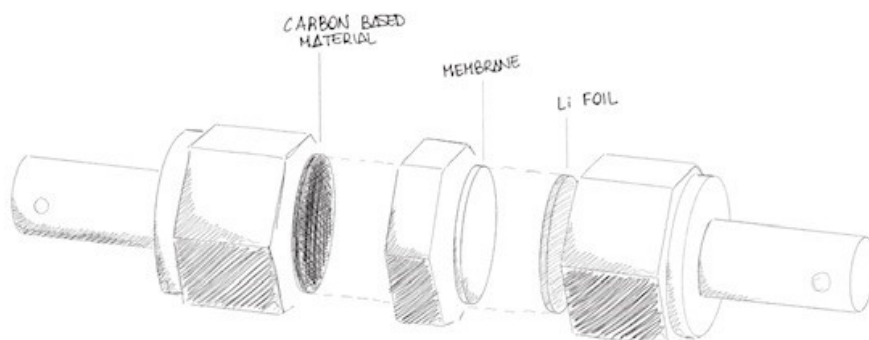


Figure 7.1: Graphical representation of the Swagelok cell used for the Li-ion capacitor tests.

Cyclic voltammetry was conducted by cycling at 5 mV s^{-1} during 30 cycles and at 2, 1, 0.5, 0.2, and 0.1 mV s^{-1} for one subsequent cycle each. In the displayed cycling, the last cycle was displayed. Charging-discharging measurements were conducted at constant current densities (i.e., 0.2 A g^{-1} for 100 cycles and 0.8 A g^{-1} for 100 cycles) or at varying current densities (i.e., 20 cycles at 0.05 A g^{-1} , 10 cycles at 0.10 A g^{-1} , 10 cycles at 0.20 A g^{-1} , 10 cycles at 0.40 A g^{-1} , 10 cycles at 0.80 A g^{-1} , and 10 cycles at 0.05 A g^{-1}) in triplicate.

The assessment of surface- of diffusion- controlled contributions was performed by changing the scan rate from 0.1 mV s^{-1} to 5 mV s^{-1} . At a certain potential, the current response (I) can be separated in two contribution as a function of the scan rate (ν): *surface controlled* (k_1) and *diffusion controlled* (k_2):

$$I = k_1\nu + k_2\sqrt{\nu} \quad (7.13)$$

Upon linearization, **equation 7.13** can be rewritten as:

$$\frac{I}{\sqrt{\nu}} = k_1\sqrt{\nu} + k_2 \quad (7.14)$$

Hence, from measuring the current at different scan rate, it is possible to calculate the ratio of surface controlled processes (Faradaic charge storage of redox-active species on the surface) or diffusion controlled processes (electric double layer formation).

Ivan K. Ilic performed the measurement for the Li-ion cathode performances.

Electrochemical CO₂ reduction reaction

To prepare the electrodes, the catalyst (10 mg) was dispersed in ethanol (200 μL) and Nafion 117 solution (50 μL , 5%). Upon sonication, a homogeneous ink was obtained. The ink (30 μL) was drop-casted on each side of a gas diffusion layer (1.5 cm x 1.0 cm, Spectracarb 2050-0550 from FuelCellStore). The solvent evaporated at room temperature, but the electrodes were dried in a vacuum oven overnight to remove possible solvent traces.

All the electrochemical characterizations were performed using a Gamry Interface 1000. The CO₂RR tests were run with a custom-made three-electrode H-cell configuration (**Figure 7.2**). A Nafion 117 membrane separated Cathodic and anolyte. An Ag/AgCl KCl sat. electrode was used as a reference, a platinum foil was used as a counter electrode, and NaOH in an aqueous solution (1 M) was used as the electrolyte.

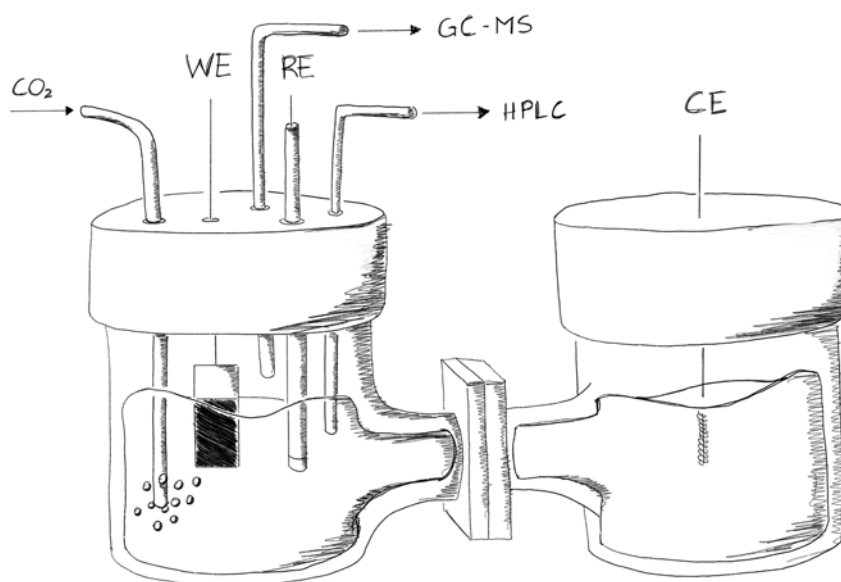


Figure 7.2: Graphical representation of the H-cell used during the CO₂RR experiments.

Catalytic performance was tested using chronoamperometry measurements at different potentials. Gas chromatography (Shimadzu GC-2014) was used to evaluate the gas products, using a MolSieve 5 A column to separate H₂ and a PorePlot Q column to analyze CO and CH₄. The liquid products were analyzed using high-performance liquid chromatography (Dionex UltiMate 3000 UHPLC system) with a RevexTM ROA-Organic Acid H⁺ LC column (300 x 7.8 mm) from Phenomenex was used. Prior the measure, the samples were acidified with H²SO₄ up to Ph 2-3 and a H₂SO₄ solution (0.005 N) was used as mobile phase at 0.5 mL min⁻¹ flow rate at 25 °C. Josep Albero performed the catalytic electroreduction of CO₂ experiments.

7.6 List of publications

Google Scholar Enrico Lepre ORCID 0000-0003-4252-3056

1. **Enrico Lepre**, Julian Heske, Michal Nowakowski, Ernesto Scoppola, Ivo Zizak, Tobias Heil, Thomas D. Kühne, Markus Antonietti, Nieves López-Salas, and Josep Albero. Ni-based electrocatalysts for unconventional CO₂ reduction reaction to formic acid. *Nano Energy*, 2022, 107191;
2. Alberto Rodríguez-Gómez \diamond , **Enrico Lepre** \diamond , Luz Sánchez-Silva, Nieves López-Salas, and Ana Raquel de la Osa. PtRu nanoparticles supported on noble carbons for ethanol electrooxidation. *Journal of Energy Chemistry*, 2022, 66, 168–180;
3. Ivan K. Ilic \diamond , **Enrico Lepre** \diamond , and Nieves López-Salas. Caffeine-derived noble carbons as ball milling-resistant cathode materials for lithium-ion capacitors. *ACS Applied Materials & Interfaces*, 2021, 13(25), 29612–29618;
4. Huize Wang, Simon Delacroix, Oliver Osswald, Mackenzie Anderson, Tobias Heil, **Enrico Lepre**, Nieves López-Salas, Richard B. Kaner, Bernd Smarsly, and Volker Strauss. Laser-carbonization: Peering into the formation of micro-thermally produced(n-doped)carbons. *Carbon*, 2021, 176, 500–510.

\diamond Shared co-authorship

7.7 Declaration

Die vorliegende Dissertation entstand in dem Zeitraum zwischen November 2019 und November 2021 am Max-Planck-Institut für Kolloid- und Grenzflächenforschung unter Betreuung von Prof. Dr. Dr. h.c. Markus Antonietti.

Hiermit erkläre ich, dass die vorliegende Arbeit selbstständig angefertigt wurde und keine anderen als die angegebenen Hilfsmittel und Quelle verwendet wurden.

Die Arbeit wurde bisher weder im Inland noch im Ausland in gleicher oder ähnlicher Form einer anderen Prüfungsbehörde vorgelegt. Es habe bisher keine früheren erfolglosen Promotionsverfahren stattgefunden.

The present work was carried during the period between November 2019 and November 2021 at the Max Planck Institute of Colloids and Interfaces under the supervision of Prof. Dr. Dr. h.c. Markus Antonietti.

I declare that I have written this work on my own and used no other than the named aids and references.

This thesis was not submitted to another examination board in this or other countries. There were no unsuccessful examination

Enrico Lepre
